UNIVERSITY OF BIRMINGHAM

Spinal Implants—The Problems of Debris

by

David Geoffrey Eckold

A thesis submitted to

The University of Birmingham

for the degree of

Doctor of Philosophy

School of Mechanical Engineering

University of Birmingham

September, 2015

Abstract

Wear debris are known to incite a variety of biological responses when released from a joint replacement device. One such response is known as osteolysis—pathological destruction of bone. Osteolysis is the major cause of failure in joint replacements. The loss of bone around a joint replacement may cause an aseptic loosening of the implant and reduce options for revision surgery. The intervertebral disc may be replaced with a joint replacement device. Often, this is done with a ball on socket joint using a metal-on-polymer material combination. ultra-high molecular weight polyethylene (UHMWPE), inherited from hip and knee implants, is a common choice in lumbar disc replacements.

The wear debris from a Charité implant, tested *in vitro*, was characterised using computer vision techniques and machine learning. It was found that wear debris from this UHMWPE and metal implant produce debris that are particularly prone to illicit an immune reaction that could lead to osteolysis.

To counter the release of wear debris into periprosthetic tissue where it can do harm, laser sintered Polyetherketoneketone (PEKK) was wear tested in an attempt to capture wear debris in the surface voids formed by the manufacturing process. Despite literature suggesting this could work, wear tests showed sintered PEKK is unsuitable as a bearing material.

Acknowledgements

I would like to thank my supervisors: Dr. Karl D. Dearn and Prof. Duncan E. T. Shepherd. Without whom, I probably wouldn't have started writing this thesis yet...

Other academic and technical staff and students I would like to thank are Dr. Daniel M. Espino, Mr. Carl Hingley, Dr. Richard Hood, Dr. Thomas Hoskins Mr. Simon Rowan, Dr. Joshua Shenker, Mr. Adam Sheward, Mr. Daniel Smith and Mr. Peter Thornton.

My thanks also go to the Biomedical Engineering Research Group—especially Naomi and Spencer, who offered help, ideas and distraction in equal measure. The others were some help as well.

I would also like to thank Felicity, who found 'The Cat'.

Lastly, I would like to thank my parents and siblings; they were, after all, a prerequisite for my existence (less so my siblings).

Contents

List of Figures

List of Tables

List of Codes

Acronyms

R_a . . . . . average roughness

R_{ku} . . . . . roughness kurtosis

R_{sk} . . . . . roughness skewness

AF . . . . . anulus fibrosus

AR . . . . . aspect ratio

AUC . . . . . area under curve

CoCrMo . . . . . Cobalt Chrome Molybdenum alloy

CT . . . . . computed tomography

CWT . . . . . continuous wavelet transform

DDD . . . . . degenerative disc disease

DLS . . . . . dynamic light scattering

ECD . . . . . equivalent circle diameter

EDS . . . . . energy-dispersive X-ray spectroscopy

EDTA . . . . . Ethylenediaminetetraacetic acid

FEG-SEM . . . . . field emission gun scanning electron microscope

FIB-SEM . . . . . focused ion beam scanning electron microscope

HCl . . . . . hydrochloric acid

HFRR . . . . . high-frequency reciprocating rig

ICP . . . . . iterative closest point

MoP . . . . . metal-on-polymer

NN . . . . . Nearest-Neighbour

NP . . . . . nucleus pulposus

PEEK . . . . . Polyetheretherketone

PEKK . . . . . Polyetherketoneketone

PIFS . . . . . Partition-Iterated Function Systems

PTFE . . . . . polytetrafluoroethylene

ROC . . . . . receiver operating characteristic

SD . . . . . standard deviation

SD-F/W . . . . . Spinal Disc Fatigue/Wear system

SEM . . . . . scanning electron microscope

SIFT . . . . . Scale-Invariant Feature Transforms

SLS . . . . . selective laser sintering

SVM . . . . . Support Vector Machine

TDR . . . . . total disc replacement

TJA . . . . . total joint arthroplasty

TJR . . . . . total joint replacement

TLD . . . . . ‘through-lens detector’

TNFα . . . . . tumour necrosis factor alpha

UHMWPE . . . . . ultra-high molecular weight polyethylene

UHR . . . . . ‘ultra-high resolution’

Chapter 1

Introduction

Wear debris are known to be one of the leading causes of the long term failure of total joint replacements (TJRs) (Purdue et al., 2006). For example, the wear debris from ultra-high molecular weight polyethylene (UHMWPE) on metal joint replacements, particularly when in the size range of 0.1–$1\ \mu\mathrm{m}$, have been shown to cause aseptic loosening of implanted devices (Green, Fisher, Bridget Matthews, et al., 2000). Consequently, there have been numerous studies which focused on the quantification, characterisation and compatibility of wear debris generated from hip and knee implants, both from *in vitro* and *in vivo* wear debris (Kobayashi et al., 1997; Nine et al., 2014; Topolovec, Milošev, et al., 2013).

A relative newcomer in the field of TJRs is spinal disc replacement. This involves the total replacement of the spinal disc, the fibrocartilaginous joint between two vertebræ in the spine. The requirement for this surgery is usually due to degenerative disc disease (DDD), a general term for the degeneration of the intervertebral disc resulting in chronic pain of the spine. The symptoms of DDD can include fluid loss from the disc leading to a loss of volume, reducing the intervertebral distance. This can have the effect of nerve impingement between the facet joints. It is also possible for the nucleus pulposus (the central, gelatinous part of a intervertebral disc) to herniate through the outer anulus fibrosus, this is commonly known as a slipped disc.

Prior to motion preserving joint replacements in the spine, DDD was often treated using a spinal fusion—the joining of two vertebræ using a bone graft to form a single bony column. While this method is highly successful in reducing pain in DDD sufferers, recently it has been questioned whether the reduction of flexibility of the spine

could cause further disc problems adjacent to the fusion in later years (Hilibrand and Robbins, 2004; Park et al., 2004).

In addition to the effects on bone, wear debris in the spinal area has been shown to induce short-term fibrosis and histiocytic reactions within the spinal column in *in vivo* animal studies (Cunningham et al., 2013). These immune reactions may interfere with the healing process after surgery. Therefore, it is especially important to reduce the release of debris into the area surrounding a spinal implant at all stages of the implant life.

In this thesis, a two pronged approach is used in an attempt to 'solve' the wear debris problem in spinal implants: i. the wear debris generated by a commonly used spinal implant device was characterised; and ii. an attempt to minimise the release of wear debris into periprosthetic tissue is explored. This is shown graphically in the thesis outline (figure 1.1).

In chapter 2, the relevant background research is presented, starting with a brief introduction to total joint arthroplasty (TJA) and the effects of wear debris discovered from hip and knee replacement surgeries. This is followed by an introduction to spinal arthroplasty, why it is done and current devices. The second part of this chapter focuses on tribology and wear—the cause of wear debris.

Chapter 3 outlines in general the materials and methods used in this thesis. This includes the *in vitro* testing methods of spinal implants used in this study and by the other studies that have generated wear debris analysed here. The methods for scanning electron and optical microscopy can also be found in this chapter.

Chapter 4 is the development and testing of a computer vision

and machine learning method for the analysis of wear debris. It covers the use of image segmentation and key feature extraction to quantify images for statistical analysis and categorisation.

Chapter 5 is the analysis of UHMWPE wear debris from a 5 million cycle fatigue test of the Charité implant performed by Moghadas, Mahomed, Shepherd, et al. (2015). The size, shape and morphology of wear debris are examined using methods from chapter 4.

Chapter 6 is the exploration of using a novel material and manufacturing process that may lead to a reduced release of wear debris into periprosthetic tissue. The material in question is selective laser sintering (SLS) Polyetherketoneketone (PEKK). The manufacturing accuracy is examined as are the tribological properties through Stribeck analysis and long term wear tests.

Chapter 7 contains the general conclusions to this thesis and alludes to further research necessary.

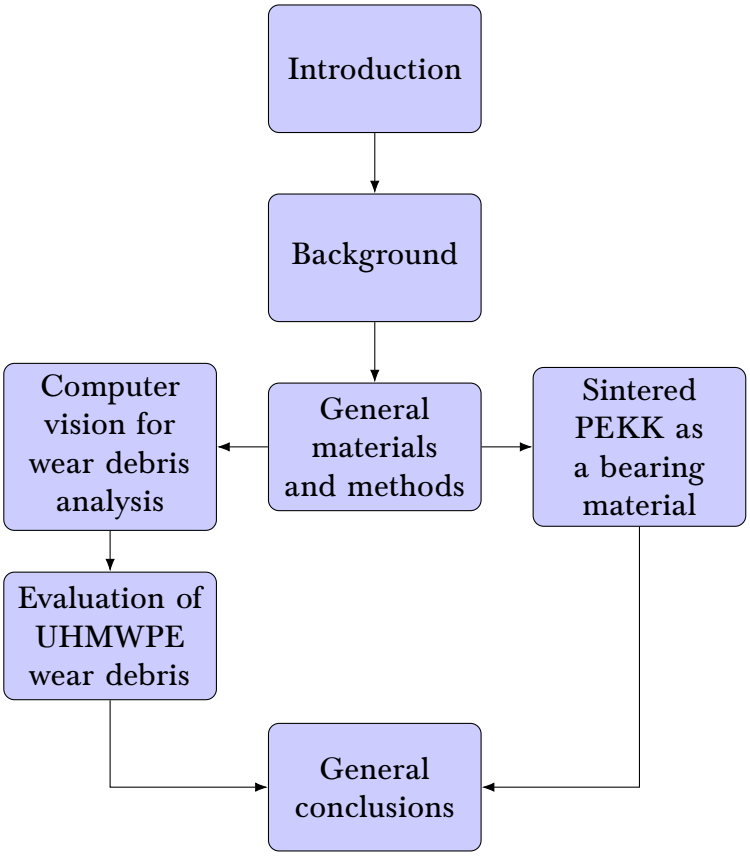

FIGURE 1.1 – Thesis outline.

Chapter 2

Background

Chapter Overview

In this chapter an overview of previous research relevant to this thesis is covered. In §2.1 an introduction into the history of total joint arthroplasty is given. The reason that wear debris is of vital concern in arthroplasty is reviewed in §2.1.1. A discussion of spinal implants—why they exist and the problems they face is in §2.1.2. Tribology, the mechanical engineering component of this thesis is reviewed in §2.2.

FIGURE 2.1 – A metal-on-metal hip implant.

2.1 Total Joint Arthroplasty

Total joint arthroplasty (TJA) is the surgical reconstruction of a damaged joint—or replacement with an artificial device. The aim of TJA is to preserve as much of the possible motions and stability of the original joint as possible, while eliminating pain. The practice of replacing joints was first recorded to have occurred in 1891, when Prof. Themistocles Glück presented the use of an ivory femoral head replacement (Knight et al., 2011). During the early 20th century, surgeons experimented with resection and replacement with tissues, such as porcine bladders (Baer, 1918), to inserting nylon sheets between the resurfaced bone ends of the joint (Kuhns and Potter, 1950) in knee arthroplasty. However, follow-ups on these surgeries showed high rates of failure, to quote Shiers (1954) 'These results are not good—they are bad.' It wasn't until the mid 20th century that total joint replacements began to mature into devices with good long term survivorships (August et al., 1986; Brown et al., 2002). The first 'modern' total joint replacement (TJR) was the Charnley *low-friction* high-density polyethylene hip (Charnley, 1972); comprised of a metal ball and stem, with a polymer cup, held in place with bone cement.

Since the introduction of the Charnley hip and subsequent refinements and improvements to the design of implants, TJR surgery has been hugely successful. Using a range of material combinations (such as metal-on-metal or ceramic-on-ceramic) and geometries (for instance, larger ball radii for increased stability) to suit the patients requirements. An example large head, metal-on-metal implant is shown in figure 2.1. However there has been one major obstacle that has existed throughout the history of TJRs; it was the cause of

the 95 % failure rate of Charnley's first attempt at hip replacements (using a 'Teflon' cup) (Charnley, 1963; Joshi et al., 1998). The issue was *osteolysis* the pathological destruction of bone (Harris, 1994, 1995, 2001). It is now known that osteolysis is initialised by the biological reactions to *wear debris* (Purdue et al., 2006).

2.1.1 The Biology of Wear Debris

Wear debris has become a 'hotly' researched topic in biomedical engineering, due to its role in osteolysis and the limits it places on implant life (Nine et al., 2014). In the early 1990's large quantities of wear debris were noticed in the periprosthetic tissue where bone resorption had occurred (Amstutz et al., 1992; Harris, 1994; Hirakawa et al., 1996; Schmalzried et al., 1992).

The mechanism by which ultra-high molecular weight polyethylene (UHMWPE) wear debris induces osteolysis has been studied. It has been found that the primary biological reaction to wear debris involves macrophages[1] (Schmalzried et al., 1992). Elevated levels of macrophages are found in the periprosthetic tissue during revision surgery—these cells have been found to have been actively phagocytosing wear debris (ibid.). The phagocytosis of wear debris has also been reproduced *in vitro* with cultured macrophages (Purdue et al., 2006; Xing et al., 2002), and *in vivo* animal models (Cunningham et al., 2013; Goodman et al., 1990; Millett et al., 2002; Schwarz et al., 2000; Wimhurst et al., 2001).

It has been found that the the inflammatory response from wear debris is variable, depending on numerous factors including: i. size,[2]

[1] A type of white blood cell.

[2] Green, Fisher, Stone, et al., 1998; Green, Fisher, Bridget Matthews, et al., 2000.

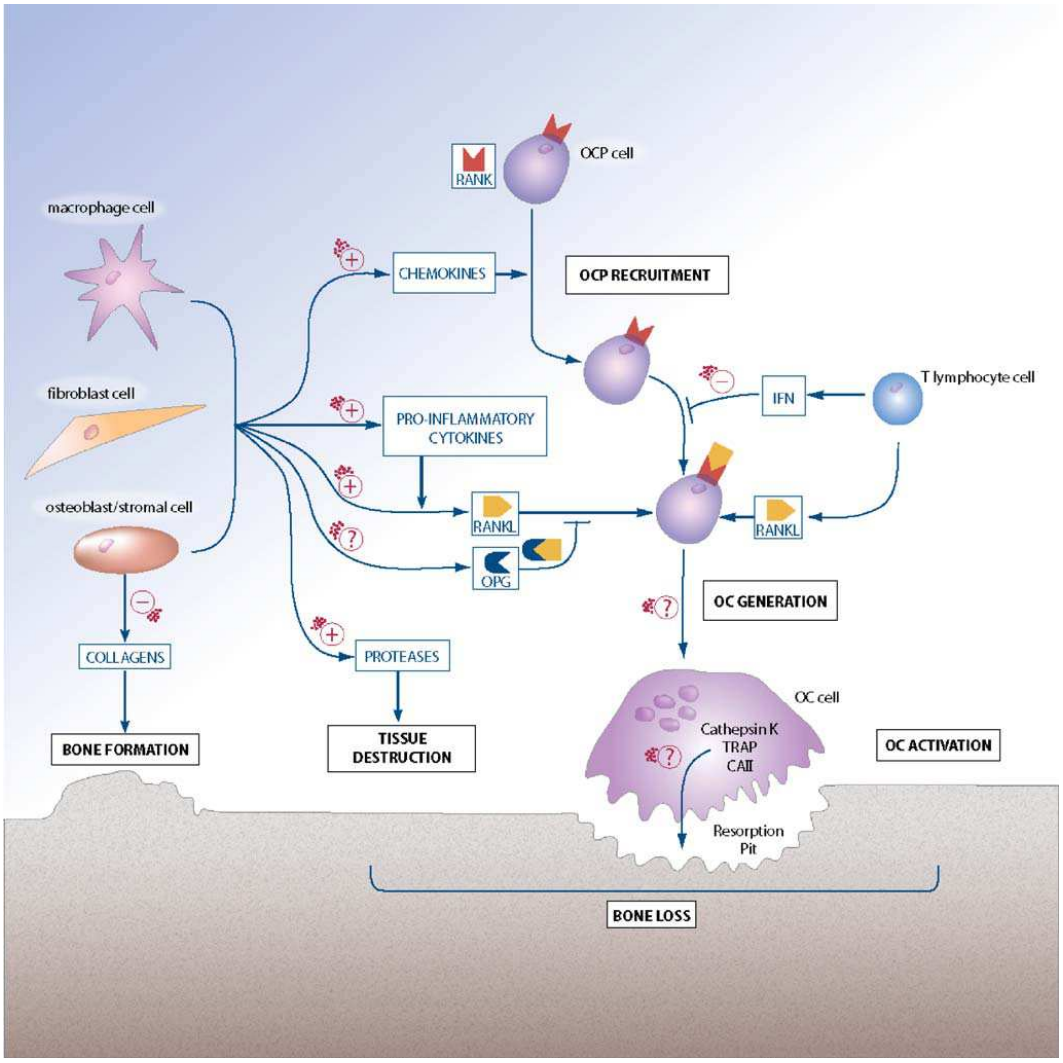

FIGURE 2.2 – Illustration of the interaction of wear debris with cellular and molecular regulation of osteoclastogenesis. *Reprinted with permission of Springer* from P. E. Purdue et al. (2006). "The central role of wear debris in periprosthetic osteolysis". In: ***HSS Journal*** 2.2, pp. 102–113.

ii. shape,[3] iii. material composition,[4] and iv. dose.[5] The response from macrophages induces other inflammatory mediators such as tumour necrosis factor alpha (TNFα) and IL-1β (Purdue et al., 2006). These cytokines[6] are precursors to osteoclasts, the cells capable of bone resorption (ibid.). An illustration of this complex process is shown in figure 2.2.

Originally, it was thought spinal implants would be immune to

[3] Yang et al., 2002.
[4] Haynes et al., 1998; Sethi et al., 2003; Shanbhag et al., 1994.
[5] Shanbhag et al., 1994.
[6] A signalling protein.

complications caused by wear debris (sometimes called 'particle disease') (Punt, Cleutjens, et al., 2009). However, revision surgery of Charité total disc replacements (TDRs) has shown cases of inflammation and osteolysis (ibid.).

2.1.2 The Spine

Anatomy of the Spine

The spine is anatomically split into sections, known as curves: i. the cervical lordosis,[7] ii. the thoracic kyphosis,[8] iii. the lumbar lordosis, and iv. the sacrum and coccyx (Cramer and Darby, 2013). The first three are labelled on figure 2.3. Disc arthroplasty surgery is performed between the vertebræ of the cervical and lumbar spine.

The cervical curve, the neck, supports the head and has the highest range of motion. The first inter-vertebral disc is found between C2–3,[9] and is therefore the most superior location that can suffer from a degenerate disc (ibid.). The thoracic region is the longest section of the spine, however its attachment to the ribs cause it to have the least mobility (ibid.). The lowest section, the lumbar is highly flexible and supports the mass of the upper body. Due to the need for both high stability and high mobility, this section is the most susceptible to degenerative diseases (Putz and Müller-Gerbl, 1996).

The vertebræ are separated by a disc which allows six degrees of freedom; i.e. it is capable of lateral motion and rotations in all axis and circumduction (Cramer and Darby, 2013). Flexion/extension

[7] Lordoses are curves that are concave posteriorly.

[8] Kyphoses are convex posteriorly.

[9] I.e. between cervical vertebræ 2 and 3, C1 is the most superior vertebra (closet to the head).

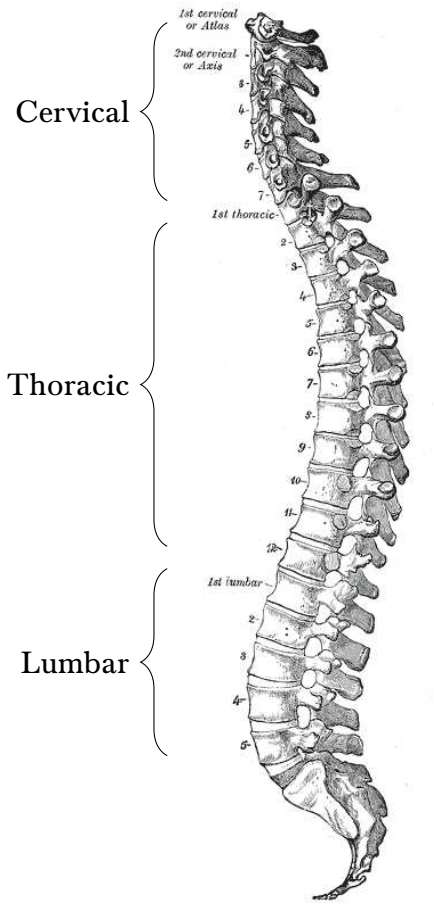

FIGURE 2.3 – Illustration of the spine[a]. *Image is in the public domain.*

[a]Gray, 1918, plate 111.

and lateral bend between two vertebræ is shown in figure 2.5. While the range of motion between two adjacent discs is small, the additive effect of many vertebræ and discs results in considerable flexibility. The discs are connected to the vertebræ by cartilaginous endplates. There are 24 inter-vertebral discs in the spine, from C2–3 to L5–S1, there is also a disc between the sacrum and coccyx. The structure of the fibrocartilaginous intervertebral joint is shown in figure 2.4.

The disc has two main parts (shown in figure 2.4(b)), i. the anulus fibrosus (AF) disci intervertebralis, and ii. the nucleus pulposus (NP).

The anulus fibrosus (of the thoracic and lumbar spine) surrounds the NP with several layers (lamellæ) of fibrocartilage. The lamellæ are 60 % by dry weight collagen fibres and 10 % elastin fibres (Bog-

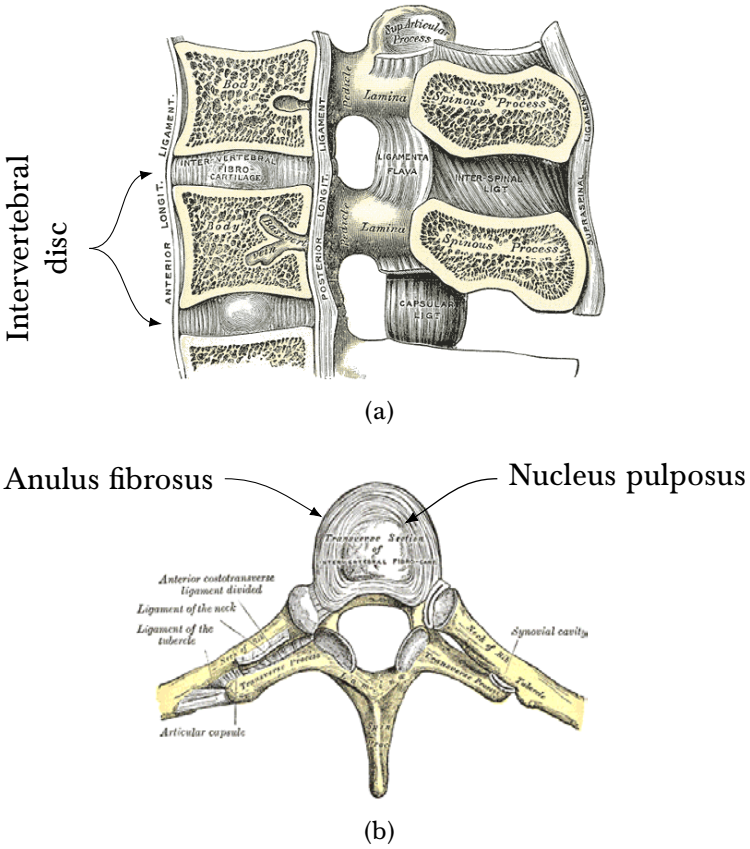

FIGURE 2.4 – Illustration of the inter-vertebral disc (a) as a cross section longitudinally of the spine[a] and (b) from above[b]. *Images are in the public domain.*

[a] Gray, 1918, plate 301.
[b] Gray, 1918, plate 313.

duk, 2005; Smith and Fazzalari, 2009). These fibres alternate in alignment between adjacent lamellæ, either at approximately 65° or 130° from vertical (Cramer and Darby, 2013). This arrangement of alternating alignments that wrap around the nucleus make the anulus robust to the stresses applied during torsion and bending (Hickey and Hukins, 1980). The AF is under tensile stress circumferentially as it resists the radial pressure from the NP, which is almost always under compression. As such, the AF is the major load bearing component of the intervertebral disc.

In the cervical spine, the anulus is a crescent shape and only a single layer, the nucleus is also thicker proportionally to the vertebræ to allow for a large range of motion (Cramer and Darby, 2013). The cervical disc dehydrates quicker than the other parts of the spine,

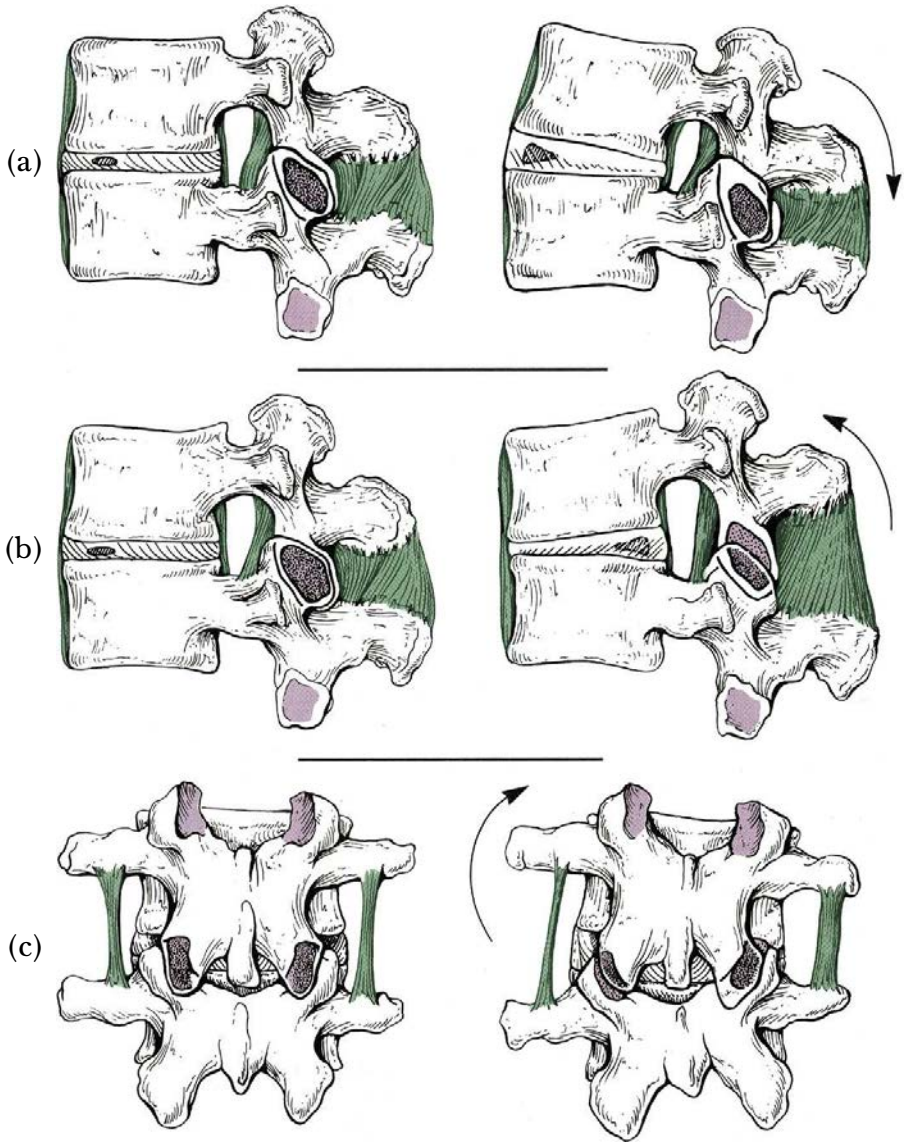

FIGURE 2.5 – Illustration of a pair of vertebræ in (a) extension, (b) flexion and (c) lateral bend. *Reprinted with permission of Elsevier.* From G. D. Cramer and S. A. Darby (2013). ***Clinical Anatomy of the Spine, Spinal Cord, and ANS***. Elsevier Health Sciences

resulting in thinning and increased pressure on the Zygapophysial Joints (Cramer and Darby, 2013).

The nucleus pulposus is the central region of the intervertebral disc. The NP is viscoelastic, and therefore has properties dependant on the rate of change of load. While it is commonly thought that the NP acts as a shock absorber—this is not the case. The NP translates the compressive load to a radial pressure contained by

the AF, the combined components of the disc allow it to behave as a thick walled pressure vessel (Hukins and Meakin, 2000). The NP is able to move within the AF in the transverse plane during bending, i.e. during flexion, the nucleus is displaced posteriorly and during extension it is displaced anteriorly (ibid.). The NP is between 70 % and 90 % water; however, since it is avascular, it must be hydrated by absorbing water from surrounding tissue. The NP reaches its peak hydration between the ages 20–30, as the disc subsequently dehydrates degeneration sets in rapidly (Coventry, 1969).

Degenerative Disc Disease

Disc dehydration and degeneration occurs naturally with age. Degenerative disc disease (DDD) a term for the accelerated and painful degeneration of a intervertebral disc (Adams and Dolan, 2012). The highest incidents of DDD occur between the ages of 30 and 50 (Marchand and Ahmed, 1990), much younger than the average age of patients requiring hip replacement surgery (Crawford and Murray, 1997).

An illustration showing three modes of disc degeneration is shown in figure 2.6. This illustration shows two types of tear: i. a circumferential tear, and ii. a radial tear. Note how one of the radial tears has ruptured the outer lamellar and the nucleus has herniated into a nerve root.

2.1.3 Arthroplasty of the Spine

UHMWPE is a common choice for joint arthroplasty as a bearing counter-face, in part due to its low chemical reactivity and tribological properties. Current TDRs such as the SB Charité and PRODISC-

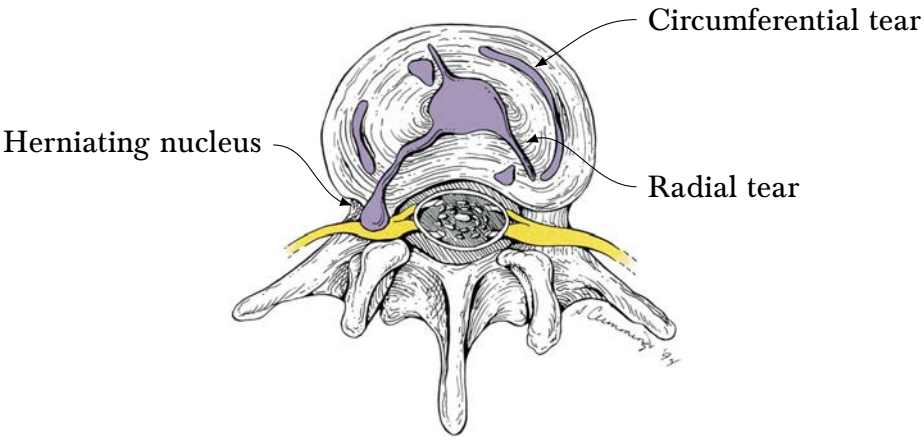

FIGURE 2.6 – Illustration of a damaged disc[a]. Note the herniating nucleus impinging on a nerve. *Reprinted with permission of Elsevier.*

[a]Cramer and Darby, 2013, p. 298.

L (DePuy Synthes Spine, Raynham, MA, USA) both make use of a Cobalt Chrome Molybdenum alloy (CoCrMo) on a UHMWPE bearing. This tribological combination is the obvious choice for TDRs given the long standing and successful use in hip and knee arthroplasty, where it was found that older, less active patients were best served by metal-on-polymer (MoP) (Milošev et al., 2012). Interest in wear debris has grown over the years as their various adverse effects have been further understood, that can reduce implant life, and induce unwanted biological reactions within the body (Harris, 1995; Ingham and Fisher, 2000)

The wear of joint replacement implants has been studied in detail (Moghadas, Mahomed, Shepherd, et al., 2015; Neukamp et al., 2014; Punt, Baxter, et al., 2011; Xin et al., 2013) and the debris from these studies are often examined using scanning electron microscopy (Nine et al., 2014), as it has excellent imaging properties at the magnification ranges required to produce highly detailed micrographs of debris. While it is easy to characterise debris on simple metrics such as equivalent circle diameter (ECD), aspect ratio (AR) and roundness, the task of categorising the contents of any image in qualitative terms i.e. morphology, remains a significant

challenge.

2.2 Tribology

Tribology is the study of friction, lubrication and wear of objects in relative motion. The name comes from the Greek *tribō* meaning 'to rub'. The first 'tribology' paper was O. Reynolds (1886). "On the Theory of Lubrication and Its Application to Mr. Beauchamp Tower's Experiments, Including an Experimental Determination of the Viscosity of Olive Oil." In: ***Proceedings of the Royal Society of London*** 40.242-245, pp. 191–203 (Stachowiak and Batchelor, 2013). However, due to the microscopic nature of many tribological properties, e.g. surface roughness, true investigation and understanding of the underlying properties of friction and wear have only been possible in the past few decades.

The tribology of two contacting surfaces is highly dependant on the surfaces microscopic structure and properties, texture, and the lubricant between them. The microstructure and properties are typically inherited from the bulk material—therefore one of the primary methods to optimise a tribological system it to select a suitable material. Another important aspect for tribology of a material is the surface texture. The surface topography can be described as a fractal, however it is usually simplified to the fluctuations in height at two distinct scales: i. waviness is the fluctuations on the macro scale, and ii. roughness on the micro scale. An example of a material displaying both waviness and roughness is shown in figure 2.7.

FIGURE 2.7 – A random surface showing both roughness and waviness.

2.2.1 Friction

Friction, the derivative of energy lost by distance, is one of the primary concerns in tribology as it is both a source of inefficiency and a driving factor of wear. The energy is dissipated in the form of heat and sound (vibrations), and by plastic deformation/fracturing (wear). See figure 2.8. While minimising friction will lead to minimising energy available to degrade the surfaces, causing wear, other factors may cause low friction to not mean low wear.

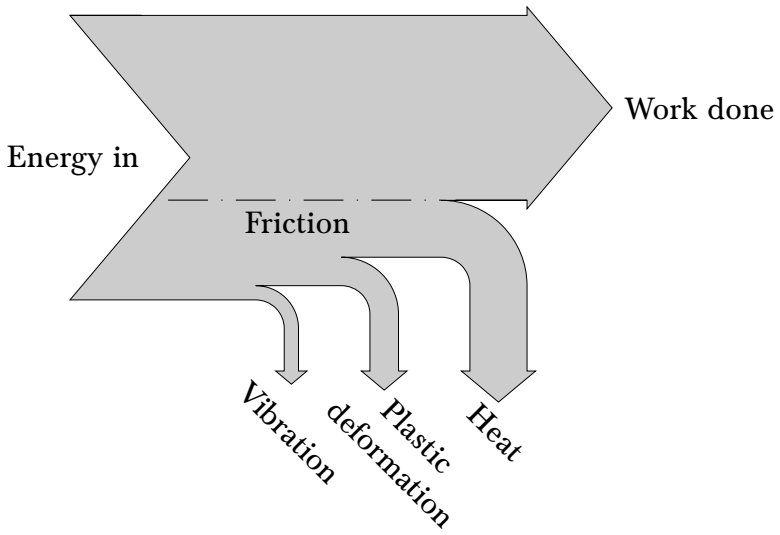

FIGURE 2.8 – Sankey diagram of the attrition caused by friction.

Historically, friction was empirically shown to follow the following laws:

i. Friction is invariant of the apparent area of contact.

ii. Friction is proportional to the normal load.

iii. Friction is invariant of the sliding velocity between the surfaces.

The first two laws are known as Amontons' laws and the third is Coulomb's law of friction. However, the cause of friction is complex and multi-factorial, therefore there are many exceptions. One of the

assumptions required for these laws is that the apparent contact (e.g. Hertzian contact area) greatly exceeds the actual contact area (where atoms are interacting between surfaces). An illustration of a large apparent contact with little area of real contact is shown in figure 2.9. The third law relies upon the flash temperature (a function of sliding velocity) being low enough, that it does not cause localised thermal expansion or alter the material properties significantly (Stachowiak and Batchelor, 2013). Polymers often do not follow these laws as they are both viscoelastic (Ferry, 1980) and sensitive to temperature.

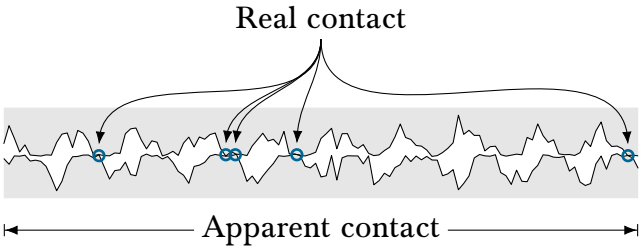

FIGURE 2.9 – Illustration of the difference between real contact area and apparent contact area.

2.2.2 Lubrication

Lubrication is the introduction of a substance between two surfaces for the purpose of reducing friction and/or wear. Typically this involves the introduction of an additional substance, although self-lubricating materials do exist. Typically the lubricating substance will be a fluid or some dispersion in a carrier fluid. Within the context of joint arthroplasty and biomedical engineering, natural synovial joints are lubricated with fluid-protein suspension. This is modelled *in vitro* with either diluted bovine serum albumin, bovine synovial fluid, and also human serum albumin (British Standards Institution, 2011b; Weightman et al., 1972).

Lubrication can be categorised into three regimes: i. boundary lubrication (figure 2.10(a)), ii. hydrodynamic lubrication (figure

2.10(c)), and iii. elastohydrodynamic lubrication. It is also possible for either of the latter two to be mixed with boundary lubrication as a hybrid regime (figure 2.10(b)). An illustration of boundary, mixed, and hydrodynamic lubrication is shown in figure 2.10. Stribeck curves can be used to ascertain which lubrication regime occurs at which sliding velocity, more detail on this is given in §6.2.2.

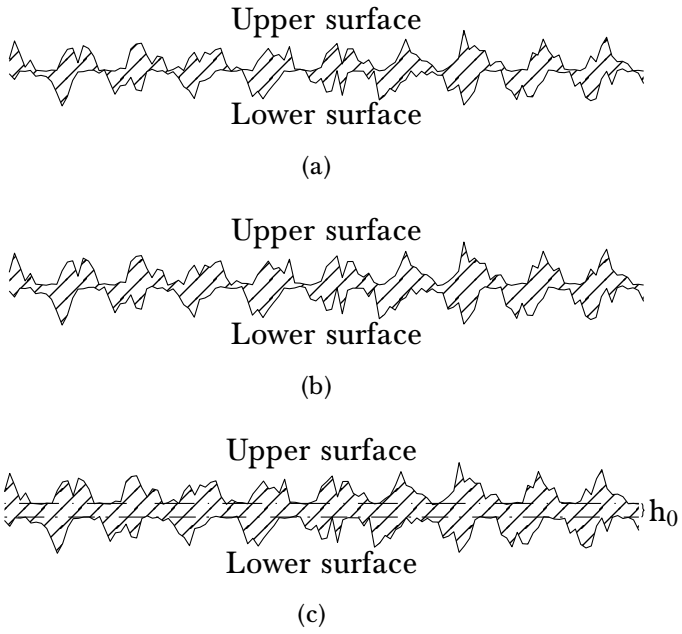

FIGURE 2.10 – Cross-section of surfaces in boundary lubrication (a), where asperities are in contact; mixed lubrication (b), where the asperities are almost touching; and hydrodynamic lubrication (c) where there is a distinct film of thickness h_0.

Boundary lubrication is where the load is supported by the asperity-on-asperity contact, much like in figure 2.9. Boundary lubrication occurs when the hydrodynamic pressure is not sufficient to support a given load, usually due to an insufficient sliding velocity (Stachowiak and Batchelor, 2013). Literature shows spinal implants operate in this mode (Moghadas et al., 2013a; Xin et al., 2013)

Hydrodynamic lubrication is where there is sufficient sliding velocity for the load to be supported by the pressure within the lubricant and there is no asperity-on-asperity contact. For hydrodynamic lubrication to occur, two conditions must be satisfied: i. the

contacting surfaces must not be parallel, and ii. the sliding velocity must be sufficient for the resulting pressure to support the load (Stachowiak and Batchelor, 2013). Hydrodynamic lubrication was discoved by Tower (1883) and was shortly after defined analytically by 'the Reynolds equation' (Reynolds, 1886).

Elastohydrodynamic lubrication is similar to hydrodynamic lubrication in that the pressure within the lubricant supports the load and there is no asperity-on-asperity contact. However, there are two additional elements to elastohydrodynamic lubrication: the elastic properties of the contacting bodies and the viscosities pressure dependence of the lubricant are fundamental to the tribological performance.

Mixed lubrication occurs as a transitional state between boundary lubrication and hydrodynamic lubrication. The load is partially supported by the lubricant pressure, but there are still some cases of asperity-on-asperity contact.

2.2.3 Wear

Wear is the process of material loss from two contacting bodies. Wear is typically categorised by the mechanism by which it was caused; there are six categories, although only five usually occur in biomedical implants. The categories are: i. abrasion, ii. adhesion, iii. fatigue, iv. fretting, v. corrosion, and vi. erosion—although this is not normally found in joint replacements (Stachowiak and Batchelor, 2013).

Abrasive wear is where one surface's asperities or a 3rd body particle cuts into the second surface—typically the abrasive is a much harder material. The result of abrasion is ploughing or micro-cutting of the softer materials surface, the wear debris produced from this mechanism often take the form of fine cutting chips (Myshkin et al., 2005).

The rate of abrasive wear has been shown experimentally to be proportional to the ultimate tensile stress and corresponding strain such that abrasion $\propto 1/\sigma_u \varepsilon_u$ (Lancaster, 1968, 1969; Myshkin et al., 2005).

Adhesive wear is when asperities in contact form a bond, known as an adhesive junction; as the surfaces slide apart the adhering material may be pulled away from it's parent surface (Stachowiak and Batchelor, 2013). The removed material may stay attached to the second surface or be released as a wear particle. In severe cases of adhesion, extremely large volumes of material may become detached—creating macroscopic sized wear debris (Hunt, 1993; Williams, 1994).

Within the majority of polymers-on-polymer and polymer-on-metal interactions, the attractive forces that create these adhesive junctions are hydrogen bonds and Van der Walls forces (Briscoe, 1982; Myshkin et al., 2005).

Fatigue wear is caused by the cyclic loading and unloading of the material. The cyclic stressing of a material causes small cracks to propagate and accumulate (Myshkin et al., 2005). The location of these cracks will typically form at a depth which will vary depending on friction coefficient; with low friction coefficients (< 0.3),

the cracks tend to occur in the subsurface region (Johnson, 1986; Myshkin et al., 2005). Above a friction coefficient of 0.3 the cracks will appear on the surface (Myshkin et al., 2005).

Fretting is the quasi-static loading and unloading of a surface—somewhat like fatigue, but when relative motion is small. Fretting typically occurs at the fixating surface between an artificial joint and the bone, rather than the bearing itself (Bryant et al., 2014; Stachowiak and Batchelor, 2013).

Corrosion is the tribologically induced chemical corrosion of a bearing surface. High flash temperatures at asperity contacts may induce oxidation or a breakdown of the lubricant or surface material (Stachowiak and Batchelor, 2013). Fretting contact is also associated with tribochemical corrosion in hip stems (Cook, Bolland, et al., 2013; Cook, Shearwood-Porter, et al., 2013).

2.2.4 Wear Debris

The characteristics of wear debris can be related to the wear mechanics of a bearing system (Anderson, 1982). These characteristics have particular importance in joint replacement implants as not only do they indicate the wear regime (Kumar, Mukherjee, et al., 2013), but they also influence immune reactions of the patient (Hallab and Jacobs, 2009; Ingham and Fisher, 2000). It is important, therefore to characterise generated wear debris to ensure implant designs and material choices minimise the formation, and release into periprosthetic tissue, the debris morphologies that correlate with the adverse biological reactions outlined above.

The size of wear debris has been associated with the ratio of surface energy and hardness, $w/\mathfrak{h}$; wear particles trapped within the bearing environment will either be combined together or break apart until they settle at this ideal size (Rabinowicz, 1961; Rabinowicz and Foster, 1964).

There are various methods to characterise wear debris. Scanning electron micrographs provide excellent qualitative information of wear particles, and with the aid of computer vision techniques, can also provide quantitative analysis. The methods and analysis gained through computer vision can range in degrees of sophistication (Gladkis et al., 2011; Raadnui, 2005; Stachowiak and Podsiadlo, 1999, 2001, 2006; Stachowiak, Stachowiak, et al., 2008), from simple area and aspect ratio measurements to machine learning and object recognition. A further benefit of this is that by classifying debris by morphology, the wear regime can often be inferred (Reda et al., 1975).

Other methods to characterise wear debris by size include the use of laser light scattering of particles undergoing Brownian motion (and thus measure the equivalent Brownian motion diameter)—either by tracking particles or autocorrelating the scattered signal (*Zetasizer μV User Manual* 2008). Another method is to measure the settling time of particles in an analytical disc centrifuge, measuring the Stokes diameter. A drawback of this method is the debris must be more dense than the fluid medium, or the particles will float and never settle, as this fluid is typically a water-glucose solution, UHMWPE may not be measured this way. It may be possible to measure UHMWPE particles in an alternative solvent, or with the low-density density adaptor—availability dependant. For higher

density particles, the disc centrifuge offers a powerful method for analysing debris, owing to the large range in particle size detectable in a single sample. Each method measures particle size in subtly different ways—resulting in each method being incomparable (Hunt, 1993).

A summary of the results of several studies of wear debris from hips and knees are shown in Table 2.1. Studies have found the majority of UHMWPE debris exists in the range of 0.1–$1\,\mu\mathrm{m}$, with low instances of particles greater than $10\,\mu\mathrm{m}$ in size. Despite continued work on the analysis of wear debris, particularly in biomedical engineering, where debris from *in vivo* and *in vitro* orthopaedic implant studies is continually characterised (Eckold et al., 2015; Hongtao et al., 2011; Kumar, Mukherjee, et al., 2013; Nine et al., 2014; Saikko et al., 2015), there have been few advancements recently on moving beyond simple size and shape attributes.

TABLE 2.1 – A comparison of UHMWPE wear debris from hip and knee implants, based on the work of Nine et al. (2014).

Type	Author	Source	Shape	Size	Instrument
Mobile bearings	Gladkis et al. (2011)	knee joint simulator	elongated, fibril like, and spherical	0.2–0.8 μm	AFM, SEM
Revision surgery of THRs	Zolotarevová, Entlicher, et al. (2010)	periprosphetic tissues	cylindrical, slice and spherical	0.1–10 μm and > 10μm	SEM, IR, EDX/EDS
Mobile bearing	Wang, Ge, et al. (2010)	hip joint simulator	round, flake, stick, and twig	frequently occurs within range of 1–30 μm, but overall size range is 0.1–320 μm	SEM, EDS
Revision surgery of THRs	Lapcikova et al. (2008)	periprosthetic tissues	elongation, 1.29 ± 0.13, 1.35 ± 0.29 and circularity, 0.97 ± 0.07, 0.93 ± 0.09	ECD, 18.5 ± 5.29 nm and 21.2 ± 8.01 nm	FEGSEM, EDS, IR
Revision surgery of THRs	Richards et al. (2008)	periprosthetic tissues	rounded, fibril, and flake	< 35%, 30 nm and 0.1–0.990 μm, rest are >1 μm	FEGSEM, EDS
Revision surgery of THRs	Koseki et al. (2005)	periprosthetic tissues	rounded, flattened, and flakes or fibrils	87.9 % < 1 μm	TEM, SEM
Hip joint	Visentin et al. (2004)	periprosthetic tissues	rounded, beads, fibrils, flakes	ECD range is from 0.48 to 0.95 μm	SEM, Micro-Raman spectrometry
Hip joint	Tipper et al. (1997)	periprosthetic tissues of THRs	fibril, platelet	most of particles, 0.1–0.5 μm and very few > 10 μm	SEM

2.3 Chapter Summary

Spinal implants are a continuation on current arthroplasty practices in hips, knees and other joints. The process involves the replacement of the intervertebral disc with an artificial joint. A common artificial disc is the Charité implant, which uses CoCrMo end-plates with a UHMWPE core. Hip and knee arthroplasty has found that UHMWPE implants, while inexpensive, have a finite life as wear debris may cause osteolysis. In older patients this is not always a concern, as even with the UHMWPEs short lifetime, the advanced age of elder patients means they are unlikely to be excessively active, resulting in a high chance of the implant outlasting them. Spinal implants, however, are typically implanted in younger patients, who are more active and are expected to live for decades after surgery.

The current state of wear debris from *in vitro* simulations of spinal implants is unknown; however, based on the performance of UHMWPE on metal hip and knee implants, and from explant studies of spines—there may be cause for concern. By confirming that spinal simulators such as the Bose ElectroForce SD-F/W (see §3.2) are accurate in recreating the conditions in the spine, and that the wear debris are similar, it will be possible to test novel geometries and surface morphologies as well as different material combinations prior to clinical trials where patients may be at risk.

One of the main objectives of this thesis is to characterise the wear debris from spinal implants, to assess the likelihood of osteolysis occurring in spinal implants and the analysis of the wear debris from a Charité implant, shown in chapter 5. The wear debris is analysed using computer vision techniques. These techniques have

not previously to the authors knowledge been used in wear debris analysis in literature and have recently been gaining sophistication and accuracy. In chapter 6, the use of a novel material and manufacturing technique is considered to attempt to reduce the release of wear debris into periprosthetic tissue.

Chapter 3

General Materials and Methods

Chapter Overview

In This chapter the general materials and methods of the thesis are laid out. In §3.2 the testing conditions for *in vitro* simulations on a spinal simulator are illustrated. How biological lubricants are digested and debris is isolated is outlined in §3.4. The digestion and filtration of wear debris from bovine serum is discussed in §3.4. The use of a high frequency reciprocating rig and associated calculations are explained in §3.3. The settings used to perform scanning electron microscopy are in §3.5, and subsequent image analysis is detailed in §4.2.3. §3.6 contains the method for using the Alicona Infinite Focus to create topology maps of samples, and the *post hoc* analysis of Alicona data.

3.1 Materials

3.1.1 UHMWPE HFRR Specimens

30 GUR1020 ultra-high molecular weight polyethylene (UHMWPE) wear testing discs (figure 3.1) were ordered from Orthroplastics (Lancashire, UK) for use in the high-frequency reciprocating rig (HFRR) detailed in §3.3. These discs were manufactured from compression moulded pins of $12\,\mathrm{mm}$ in diameter and machined into discs of thickness $4\,\mathrm{mm}$. The UHMWPE was 1020 grade, which has a density of $930\,\mathrm{kg\,m^{-3}}$.

FIGURE 3.1 – Example HFRR Specimen manufactured by Orthoplastics.

3.1.2 PEKK Specimens

6 Polyetherketoneketone (PEKK) spinal disc sockets and 30 HFRR discs were ordered from Oxford Performance Materials (South Windsor, CT, USA). The manufacturing process was selective laser sintering. The lumbar total disc replacement (TDR) specimens were manufactured following the same drawing used by Moghadas (2012, p. 180) (see appendix B) used to test UHMWPE. The PEKK sockets were used in conjunction with CoCrMo balls from the same study. The socket had a specified radius of $10.350\,\mathrm{mm}$, as Moghadas, Shep-

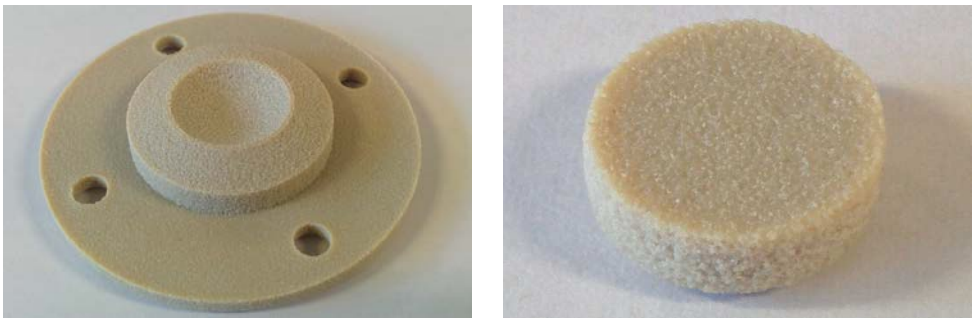

(a) (b)

FIGURE 3.2 – Sintered PEKK specimens, where (a) is a spinal implant specimen and (b) is a specimen for the HFRR.

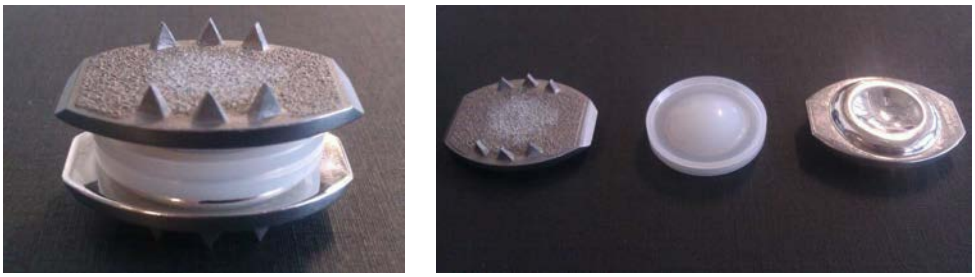

(a) (b)

FIGURE 3.3 – The Charité implant shown combined (a) and in pieces (b).

herd, et al. (2012) found smaller radius polymer socket on metal ball had superior friction characteristics. The HFRR discs were specified to be 10 mm in diameter and of 4 mm thickness—the standard size for HFRR specimens.

3.1.3 Charité Wear Debris

The wear debris analysed in chapter 5 was generated in 5 million cycle wear tests performed by Moghadas, Mahomed, Shepherd, et al. (2015). The implant in question was a Charité lumbar TDR manufactured by DePuy Spine (Raynham, MA, USA). Figure 3.3 shows an example of a Charité implant both assembled, and in parts. The two endplates are manufactured from Cobalt Chrome Molybdenum alloy (CoCrMo) and the core is UHMWPE.

3.2 Wear Testing on Bose SD-F/W

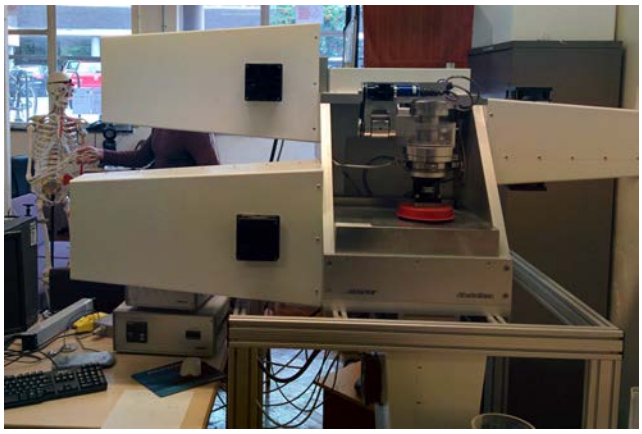

FIGURE 3.4 – A Bose ElectroForce SD-F/W test system.

The *in vitro* simulation was performed on a Bose ElectroForce Spinal Disc Fatigue/Wear system (SD-F/W) (Bose Corp., ElectroForce Systems Group, Eden Prairie, Minnesota, USA). This system is pictured in figure 3.4, the software was Wintest 4.1. The Bose SD-F/W was designed specifically for the *in vitro* testing of spinal implants. The simulator is capable of rotational motion in all three axis and linear motion in one axis (to apply a compressive load). There is also a temperature controlled lubricant bath within which the test specimens are held. Each actuator and the lubricant bath are PID controlled to ensure the simulator behaves as commanded despite differences in materials or geometries being tested.

TABLE 3.1 – Load and displacement settings for lumbar *in vitro* simulation as outlined by BS ISO 18192-1:2011

Actuator	Min	Max	Frequency
	Angle		
Flexion/Extension	−3°	6°	1 Hz
Axial Rotation	−2°	2°	1 Hz
Lateral Bend	−2°	2°	1 Hz
	Force		
Axial Load	500 N	2000 N	2 Hz

Tests were performed following ISO 18192 (British Standards

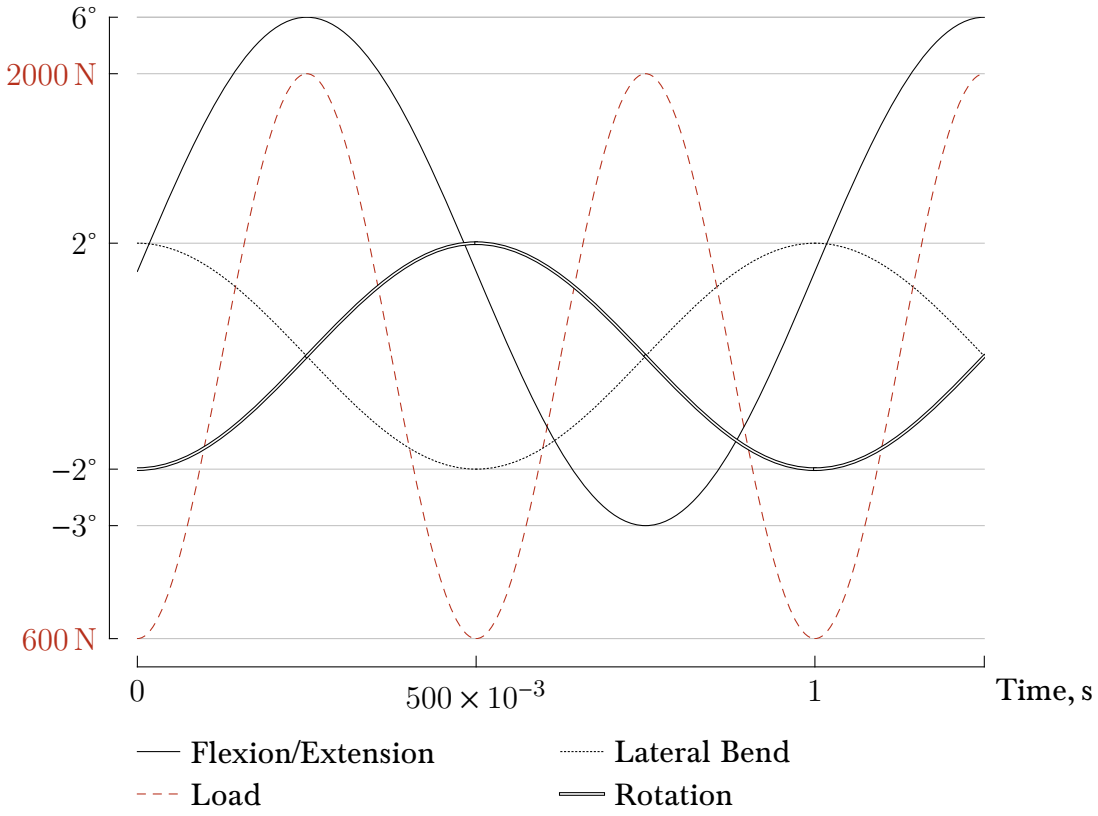

FIGURE 3.5 – Sine waves of each actuator according to BS ISO 18192-1:2011.

Institution, 2011b), this standard outlines the load and displacement waveforms that each axis of the simulator must follow. The minimum and maximum actuator settings and the frequency is shown in Table 3.1.

The phase of the sine waves are shown in figure 3.5, where load and flexion are in phase, lateral bend is $+\frac{\pi}{2}$ and rotation is $-\frac{\pi}{2}$. The direction in which these loads and displacements were applied is demonstrated in figure 3.6, where a Charité implant is used as an example. In addition to the test parameters, limits were set on the actuators to prevent damage to the machine should a device fail; rotation, flexion extension, and lateral bend are limited to ±2° beyond their settings. Load is limited to 2.400×10^3 N and −400 N. If these limits are exceeded, the simulator will automatically

initiate a controlled stop. The actuators were PID tuned; each of the displacement driven motions are tuned manually to a triangular waveform in free space. A metal dummy specimen was used to roughly tune the load actuator to a square wave, and fine tuned on the test specimen using the 'TuneIQ' function within the Bose Wintest software. Amplitude compensation of $0.5\,\%$ was used on the load actuator to ensure the load reaches its settings without the risk of over tuning the actuator which could cause unpredictable behaviour and loss of control.

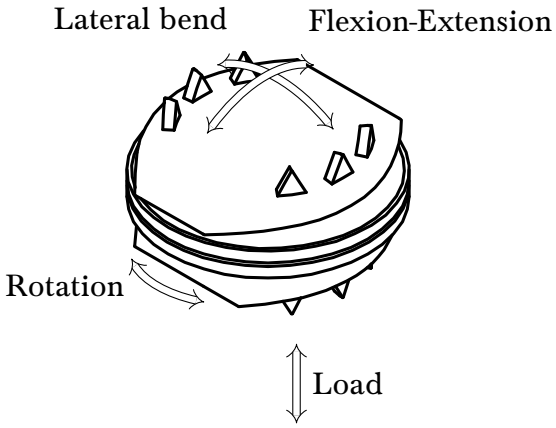

FIGURE 3.6 – Directions of motion applied to a Charité disc implant.

The standard also states a lubricant of bovine serum albumin $20\,\mathrm{g\,l^{-1}}$[1] protein content in deionised water at $37\,^{\circ}\mathrm{C}$ should be used. In addition, sodium azide ($300 \times 10^{-3}\,\mathrm{g\,l^{-1}}$) was used as a bactericide. The ISO standard states it is optional to use Ethylenediaminetetraacetic acid (EDTA) to prevent calcium deposits precipitating out of solution, which can be seen during electron microscopy. Since previous studies by Moghadas (2012) and Xin (2013) were performed without the addition of EDTA; to maintain compatibility with these studies, no EDTA was used. As the wear test progressed, lubricant evaporated; to ensure the bearing surfaces were always fully sub-

[1] Moghadas (2012) and Xin (2013) also performed tests using BS ISO 18192-1:2008 (British Standards Institution, 2008) which specified $30\,\mathrm{g\,l^{-1}}$ protein content.

merged, the lubricant was 'topped up' with deionised water at least once every 24 hours.

All implants that were tribologically tested in bovine serum had to be cleaned and dried prior to both testing and weighing using the following protocol. Implants were weighed initially and every subsequent 0.25 million cycles. After each 0.25 million cycles, the implant was removed from the machine, $50\,\mathrm{ml}$ of lubricant was extracted from the lubricant bath, after stirring to ensure some of the larger particles that sediment out quickly were sampled, and frozen for later analysis. Both the implants and the machine components that were in contact with bovine serum were soaked in Virkon (DuPont Chemical Solutions Enterprise, Wilmington, DE, USA) for 2–24 hours, then rinsed with distilled water. Once dry, the implant was soaked in 2-propanol (Sigma-Aldrich, St. Louis, MO, USA) for 5 minutes in an ultrasound bath, and then rinsed with acetone (Fisher Scientific UK Ltd, Loughborough, United Kingdom). The implant was then desiccated in a vacuum desiccator for 48 hours. Any remaining particulates were removed with an air duster and lint free towels. After the sample was cleaned between each 0.25 million cycles, the implant was weighed on an Ohaus GA 200 D analytical balance (Ohaus Europe GmbH, Nänikon, Switzerland) 5 times in different orientations and a mean was taken. The implant was then reset in the simulator and realigned by pre-loading to $\approx 50\,\mathrm{N}$ in displacement control, and then using the x, y stage to move the implant to find a minima in load. Fresh lubricant was then added to the bath and allowed to warm to $37\,^{\circ}\mathrm{C}$ before (re)starting the test. Before the wear test was started, the frictional torques in each axis were measured for the purpose of plotting stribeck curves (see

§6.2.2), the procedure and results for this are shown in chapter 6.

3.3 High Frequency Reciprocating Rig

For the purpose of finding abrasion and adhesion training debris, a HFRR ball on disc tribometer (PCS Instruments, London, United Kingdom) using a steel ball (ANSI E-52100, PCS Instruments) on UHMWPE disc was used in two scenarios (figure 3.7(a)). In both cases, tests were conducted at $37\,^{\circ}\mathrm{C}$ in deionised and filtered water was used to ensure particles found in the lubricant were wear debris and not contaminants. The scenarios were designed to deliberately induce either abrasion or adhesion in a simplified manner to allow for the identification of these wear debris morphologies (Stachowiak and Podsiadlo, 2006; Stachowiak, Stachowiak, et al., 2008). The two scenarios were:

i. A roughened ball of roughness $R_a = 0.5\,\mu\mathrm{m}$ run at $20\,\mathrm{Hz}$ over a short time period (20 minutes). The ball was roughened with P400 grit WetorDry (3M, St. Paul, Minnesota, USA).

ii. A smooth ($0.05\,\mu\mathrm{m}$ roughness) ball at $25\,\mathrm{Hz}$ for 4 hours.

The applied load in both cases was $0.981\,\mathrm{N}$. These parameters were chosen based on the Hertzian elastic contact properties of the spinal simulator used in §3.2. The frequencies were chosen after the machine constraints denied the ability to exactly replicate sliding velocities in ISO 18192. Further calculations were performed to ensure the chosen frequencies were within acceptable limits defined by glass transition temperature of UHMWPE. The Hertzian contact calculations are shown in section §3.3.1

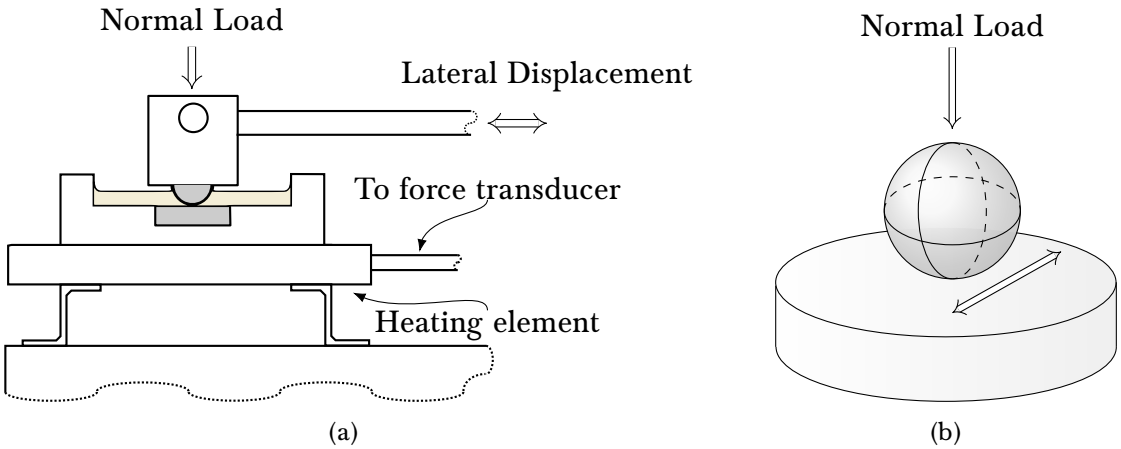

FIGURE 3.7 – Schematics of (a) the specimen holder and surrounding parts of the HFRR, and (b) the kinematics of the HFRR.

The surface roughness's of the balls were measured before testing using an Alicona Infinite Focus optical 3D micro coordinate system (Alicona Imaging GmbG, Raaba/Graz, Austria), see §3.6. Both sets of conditions were run in 1 ml of lubricant comprising of ultra-pure deionised water (Resistivity: $> 18\,\mathrm{M\Omega\,cm}$, Inorganic content: < 2 ppb). The lubricant, containing debris, was vacuum filtered and prepared for the scanning electron microscope (SEM) using the method in §3.4.

3.3.1 Hertzian Elastic Contact

To calculate the resultant contact pressure of the applied load used in §3.2, Hertzian contact mechanics were employed (Johnson, 1986). By calculating the contact pressure a Charté implant is subject to when at maximum load ($2000\,\mathrm{N}$), the equations (Equations 3.2 & 3.1) can be solved for the ball on plate geometry of the HFRR, or other tribometer arrangements. These equations are solved in MATLAB, the code is shown in appendix A (code snippet A.1 on

page 137). The contact pressure was calculated from:

$$p_0 = \frac{3W}{2\pi a^2} \tag{3.1}$$

where p_0 is the maximum contact pressure, W is the normal load and a is the radius of the contact area given by:

$$a = \sqrt[3]{\frac{3WR^*}{4E^*}} \tag{3.2}$$

The equivalent elastic modulus was calculated from:

$$\frac{1}{E^*} = \overbrace{\frac{1-\nu_1^2}{E_1}}^{\text{Socket/disc material properties}} + \underbrace{\frac{1-\nu_2^2}{E_2}}_{\text{Ball material properties}} \tag{3.3}$$

where, E_1, E_2 are the elastic moduli of the materials, E^* is the combined modulus and ν_1, ν_2 are the Poisson's ratios of the materials.

The equivalent radius was calculated from:

For a socket, the radius is negative; a flat disc has radius ∞.

$$\frac{1}{R^*} = \overbrace{\frac{1}{R_1}}^{\text{Socket/disc radius}} + \underbrace{\frac{1}{R_2}}_{\text{Ball radius}} \tag{3.4}$$

where, R_1, R_2 are the radii of the ball and socket and R^* is the combined radius.

Charité Mechanics Using the geometry of the wear test specimens used by Moghadas (2012) (10 mm or 14 mm radius ball with a 0.35 mm radial clearance) and the maximum load for lumbar disc testing, 2000 N (British Standards Institution, 2011b). The contact pressure was calculated using the Hertzian elastic contact equations 3.3–3.1:

$P_{10\,\mathrm{mm}}$ 14.98 MPa

$P_{14\,\mathrm{mm}}$ 9.63 MPa

The sliding speed at the centre of contact was calculated using the following from the ISO standard for spinal disk testing:

Flexual range: 9°

Lateral bend: 4°

Rotation: 4°

Frequency: $1\,\mathrm{Hz}$

The velocity due to the rotational component tends towards 0 at the centre of the contact area, since this is where the maximum pressure is located, it was ignored for the purpose of converting testing parameters to the HFRR.

$$S(x,y) = \overbrace{3.5\sin(\omega t)\underline{i}}^{\text{Flexion}} + \overbrace{2\cos(\omega t)\underline{j}}^{\text{Lateral bend}} \tag{3.5}$$

$$\dot{S}(x,y) = 3.5\omega\cos(\omega t)\underline{i} - 2\omega\sin(\omega t)\underline{j} \tag{3.6}$$

therefore,

$$|\dot{S}(x,y)| = \sqrt{(3.5\omega\cos(\omega t))^2 + (-2\omega\sin(\omega t))^2} \tag{3.7}$$

The maximum sliding speed ($|\dot{S}(x,y)|$) was therefore $21.991\,\mathrm{mm\,s^{-1}}$, and the average speed is $17.289\,\mathrm{mm\,s^{-1}}$.

HFRR Mechanics By holding the sliding speed at a constant $17.289\,\mathrm{mm\,s^{-1}}$ and the frequency to the machine minimum to $10\,\mathrm{Hz}$, the stroke length can be calculated as follows:

$$17.289 = a\omega$$

$$\text{Stroke} = 2a$$

$$\text{Stroke} = 550\,\mu\mathrm{m}$$

Since $550\,\mu\mathrm{m}$ is very small, the frictive mode would involve largely fretting. However, as the shear force from friction is invariant to sliding velocity, barring temperature and lubrication effects, the wear effects should be unaffected by using the HFRR at $10\,\mathrm{Hz}$ and a stroke of $2\,\mathrm{mm}$.

The minimum normal load the HFRR is capable of applying is $100\,\mathrm{g}$ ($0.98\,\mathrm{N}$). The geometry of the HFRR is a $3\,\mathrm{mm}$ radius steel ball on a flat UHMWPE disc. By treating the flat UHMWPE disc as a socket with infinite radius, the mean contact pressure is calculated to be $25.20\,\mathrm{MPa}$.

3.3.2 Temperature Calculation

Medical grade UHMWPE will soften at $80\,^{\circ}\mathrm{C}$ (Ticona, 2001). As the flash temperature would increase with sliding velocity, the maximum frequency for the HFRR was calculated using both unidirectional sliding calculations and calculations with an oscillating heat source. It is believed that the cooling effect of the lubricant will cause the true temperature to lie between these two temperatures.

Unidirectional Sliding

The Temperature rise from unidirectional sliding at location x and depth z, $T(x, z)$, is given by Carslaw and Jaeger (1959). The equation is reprinted in Johnson (1986, p. 378) and shown below in a modified state for when the heat source is circular instead of a line contact:

$$T(x,y,z) - T_0 = \frac{\dot{h}}{2\pi\alpha} \int_{t'=-\infty}^{0} \int_{s=-a}^{a} \int_{\theta=0}^{2\pi} \frac{\langle \Re \rangle}{t'} \exp\left\{ -\frac{(x - s\cos\theta - Vt')^2 + (y - s\sin\theta)^2 + z^2}{4\alpha t'} \right\} \mathrm{d}\theta \mathrm{d}s \mathrm{d}t' \quad (3.8)$$

where,

$$\langle \Re \rangle = \begin{cases} 1 & \text{flat contact} \\ \sqrt{1 - \left(\frac{s}{a}\right)^2} & \text{parabolic contact} \end{cases} \tag{3.9}$$

and,

$$\alpha = \frac{k}{\rho c_p} \tag{3.10}$$

$$\dot{h} = \mu p_0 V \tag{3.11}$$

where T is the temperature, T_0 is the initial temperature, k is the thermal conductivity, ρ is mass density, and c_p is specific heat capacity. μ is the friction coefficient, V is velocity, t is time, and t' is instantanious time. This equation is solved with the MATLAB code A.2 in appendix A page 138.

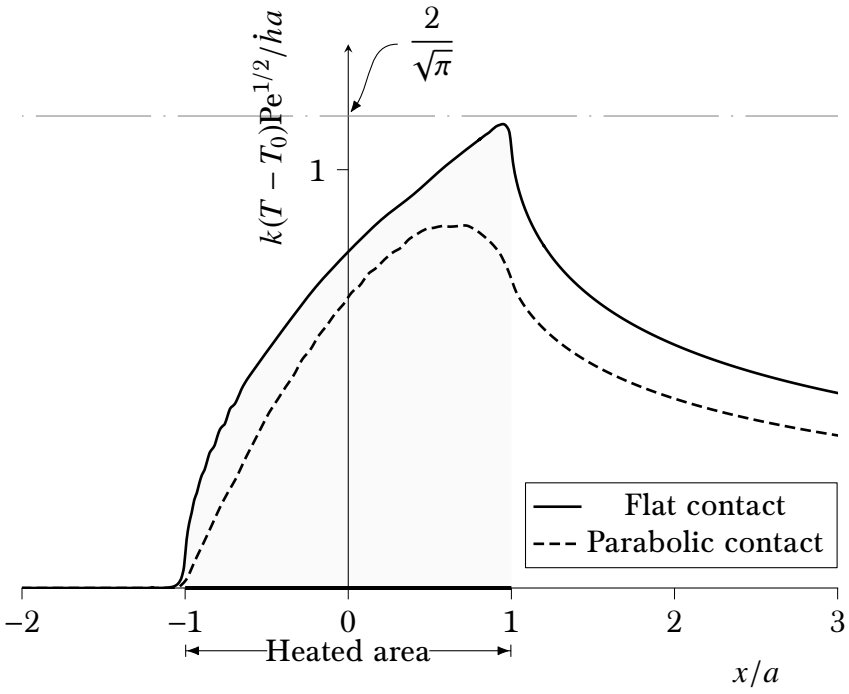

FIGURE 3.8 – Normalised x location of maximum dimensionless temperature rise due to unidirectional sliding when $y = z = 0$.

The above equation 3.8 was solved using the adaptive quadrature function in MATLAB at various positions of x, the results are shown in figure 3.8. It can be seen that in the case of a flat contact, the maximum dimensionless temperature is close to where $x = a$ and

can be approximated to be $\frac{2}{\sqrt{\pi}}$. However, in the case of a parabolic contact—such as a sphere on flat arrangement, the maximum dimensionless temperature rise was 0.866. Therefore the maximum temperature rise can be simplified to equation 3.12 (Williams, 1994, p. 128).

$$T_{max} - T_0 = \begin{cases} \frac{2}{\sqrt{\pi}} \cdot \frac{\dot{h}a}{k} \cdot \mathrm{Pe}^{-1/2} & \text{flat contact} \\ 0.8663 \cdot \frac{\dot{h}a}{k} \cdot \mathrm{Pe}^{-1/2} & \text{parabolic contact} \end{cases} \tag{3.12}$$

where Pe is the Peclet number,

$$\mathrm{Pe} = \frac{Va}{2\alpha} \tag{3.13}$$

Solving equation 3.12 between $10\,\mathrm{Hz}$ to $30\,\mathrm{Hz}$ in operating frequency and between oscillating amplitudes $100 \times 10^{-3}\,\mathrm{mm}$ to $1\,\mathrm{mm}$ produces a temperature rise shown in figure 3.9(a).

As shown by figure 3.9, the temperature rise due to unidirectional sliding at between 10–30 Hz and at oscillating amplitudes up to $1\,\mathrm{mm}$ is small ($<5.6\,^{\circ}\mathrm{C}$)—resulting in a flash temperature ($<42.6\,^{\circ}\mathrm{C}$); well below the softening temperature of UHMWPE ($80\,^{\circ}\mathrm{C}$). However this equation assumes a perfectly flat half-space and spherical elastic body, in reality, it is likely non-uniformity of surfaces will cause localised hotspots greatly exceeding the calculated value (Stachowiak and Batchelor, 2013, p. 513).

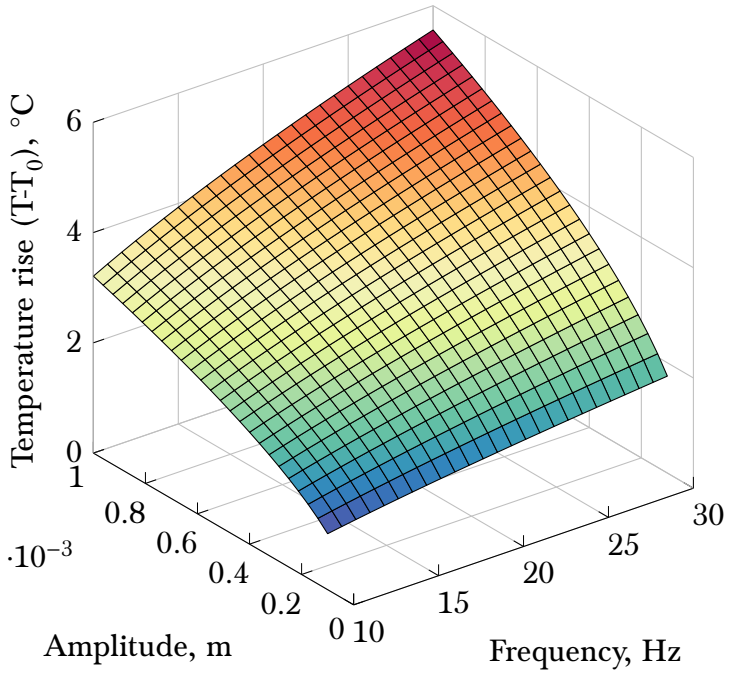

(a)

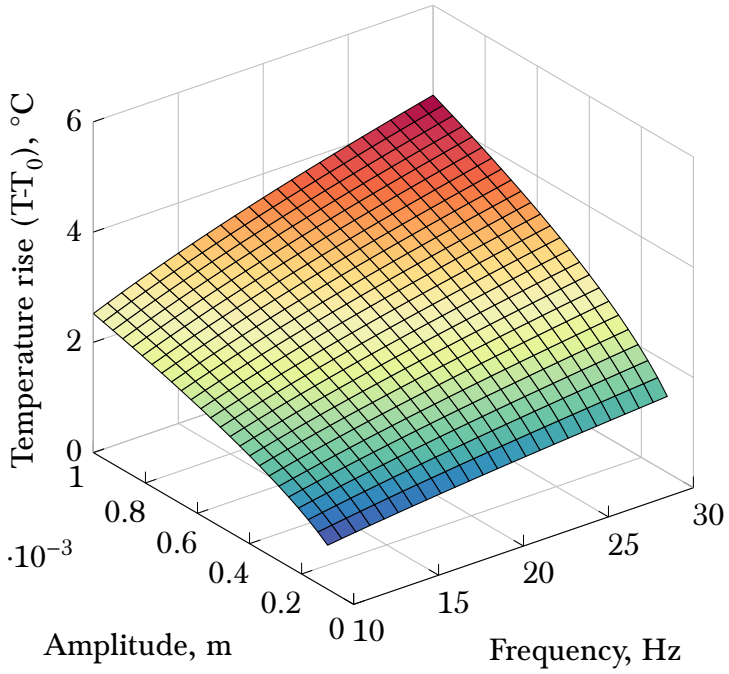

(b)

FIGURE 3.9 – Temperature rise as a function of frequency and oscillating amplitude due to (a) a flat contact, and (b) a parabolic contact.

Oscillating Heat Source

The transient temperature at (x, y, z, t) is given by:

$$T(x,y,z,t) - T_0 = \frac{\dot{h}}{2\pi\alpha} \sum_{i=t'}^{t} \int_{t'_{i-1}}^{t'_i} \frac{|\sin(\omega t')|}{t'^{3/2}} \int_{s=-a}^{a} \int_{\theta=0}^{2\pi} \langle \Re \rangle \exp\left\{ -\frac{(x - s\cos\theta - v(t'))^2 + (y - s\sin\theta)^2 + z^2}{4\alpha t'} \right\} \mathrm{d}\theta \mathrm{d}s \mathrm{d}t' \quad (3.14)$$

where,

$$v(t') = A(1 + cos(\omega t')) \quad (3.15)$$

The calculation of temperature is based on the work by Wen and Khonsari (2007), their work involved deriving an extension to the analytical equation given by Carslaw and Jaeger (1959) (Equation 3.8) for the transient temperature during fretting contact (equation 3.14). This equation is solved with the MATLAB code A.3 in appendix A page 140.

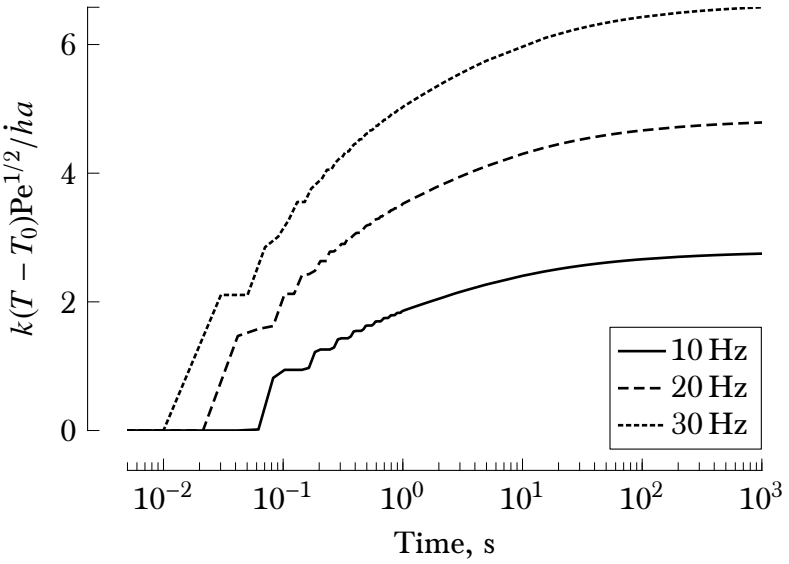

FIGURE 3.10 – log(t) plot of temperature rise at ($x = y = z = 0$).

Figure 3.10 shows the temperature rise for a parabolic contact at three frequencies, the temperature rise when the heat source oscillates over a point will experience an exponentially approaching

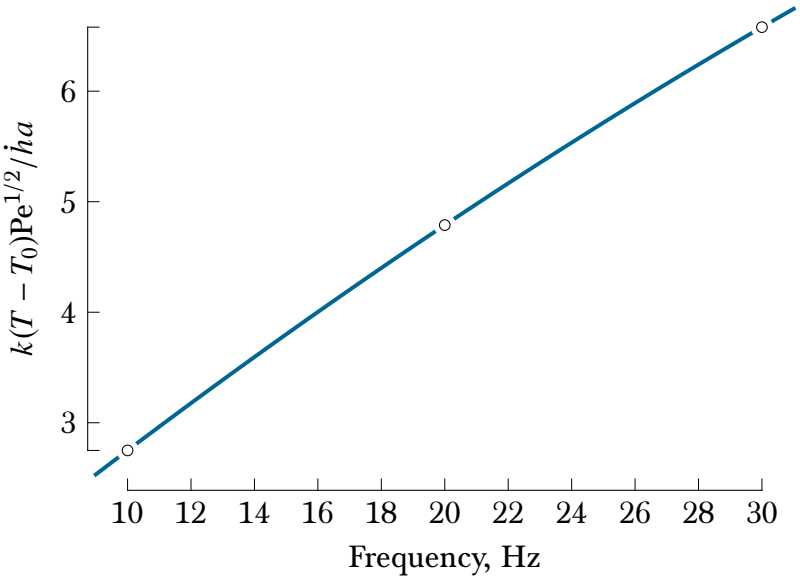

FIGURE 3.11 – Fitted data of the final temperature rise with increasing frequency.

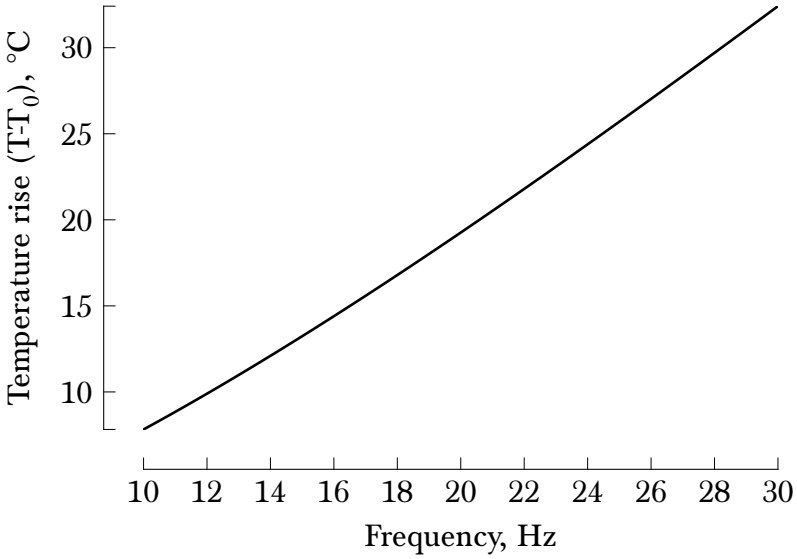

FIGURE 3.12 – Final oscillating temperature rise with frequency for a parabolic contact.

temperature increase. The final temperature rise is shown in figure 3.11, this shows a quadratic curve fit with the equation 3.16, the R^2 value for this fit is 1 (the norm of residuals is below the error for double precision floating point numbers). A curve fit was used to interpolate results due to the computational time to solve for each frequency.

$$\text{Fit} = -0.001238.f^2 + 0.241.f + 0.4633 \tag{3.16}$$

$$T - T_0 = \text{Fit} \cdot \frac{\dot{h}a}{k} \cdot \text{Pe}^{-1/2} \tag{3.17}$$

Figure 3.12 shows the final temperature rise for an oscillating parabolic contact. It can be seen that the temperature rise increases to the square for increasing values for frequency, where at $30\,\text{Hz}$, the temperature rise is $32.41\,°\text{C}$ (meaning a flash temperature of $69.41\,°\text{C}$). However these equations assume a perfectly flat half-space and spherical elastic body; in reality, it is likely non-uniformity of surfaces will cause hotspots greatly exceeding the calculated value. Therefore oscillating frequencies above $30\,\text{Hz}$ were not used.

3.4 Bovine Serum Digestion and Filtration

The isolation of polymer debris was performed using the hydrochloric acid (HCl) method presented in BS ISO 17853:2011 (British Standards Institution, 2011a, p. 9). This is necessary as plasma proteins such as albumin will irreversibly bind to UHMWPE particles (Zolotarevová, Hudeček, et al., 2010). A volume of $10\,\text{ml}$ of bovine serum containing debris was mixed with $40\,\text{ml}$ hydrochloric acid, $32\,\%$ w/w, using a vortex mixer and this was then incubated at $50\,°\text{C}$ for 1 hour in a water bath.

From the digested bovine serum $0.5\,\text{ml}$ was diluted into $100\,\text{ml}$ of analytical grade methanol, (Fisher Scientific UK Ltd, Loughborough, United Kingdom) and vacuum filtered through $0.1\,\mu\text{m}$ Nuclepore filters (Whatman International Ltd, Maidstone, United Kingdom).

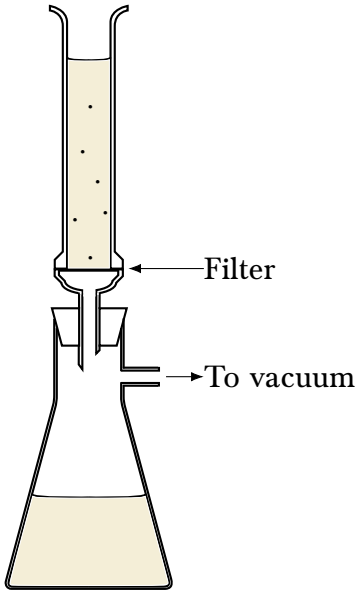

FIGURE 3.13 – Vacuum filtration schematic.

The filter was cut with a scalpel to 5 mm x 5 mm squares and fixed to an SEM stub with either a strip of copper tape or a carbon conductive tab, and allowed to dry in a desiccator for 24 hours prior to sputter coating and electron imaging.

3.5 Scanning Electron Microscopy

Scanning electron microscopy is a technique to generate very high resolution micrographs at high magnification. It involved the use of a high-tension electron beam that rasters across the objects surface. The electron beam upon striking the specimen interact with the surface causing the release of secondary electrons, X-rays cathode-luminescent and backscattering primary electrons from the beam. All images used for the methods described in §4 use secondary electron images (unless they were produced with the Hitachi TM 3030, which produces only backscatter images).

FIGURE 3.14 – Platinum sputter coating of a specimens.

Prior to electron imaging, any non-conductive specimen must be coated in a thin conductive coating and grounded, otherwise

the specimen would become charged. A charged specimen would cause warping artefacts and other aberrations on the image—the trapped electrons would repel electron beam altering its path. The filters were therefore sputter coated with either gold or platinum for 60 seconds at 30 mA using an Agar automatic sputter coater (Agar Scientific, Elektron Technology UK Ltd, Essex, United Kingdom). Silver conductive paint (RS components Ltd, Northants, United Kingdom) was dabbed on an edge to create a conductive bridge between the coated surface and the SEM stub.

Depending on the availability and state of repair of an electron microscope (SEMs are notorious for breaking down), different equipment was used. Electron microscopy was performed using one of the following microscopes:

FEI 235 Dualbeam FIB-SEM

A FEI 235 dualbeam focused ion beam scanning electron microscope (FIB-SEM) (FEI, Hillsboro, Oregon, USA). Secondary electron images were taken using the electron column with an acceleration voltage of 10–12 kV and the 'through-lens detector' (TLD) on 'ultra-high resolution' (UHR) mode. The TLD differs from a Everhart-Thornley detector in that the detector is placed above the objective lens rather than in the specimen chamber, this has the effect of changing the apparent illumination source to above the specimen, rather than from the detector.

Jeol 7000F FEG-SEM

A Jeol 7000F field emission gun scanning electron microscope (FEG-SEM) (Jeol Ltd., Tokyo, Japan), secondary electrons are

detected using an Everhart-Thornley detector using a beam voltage of $5\,\mathrm{kV}$,[2] a beam current of $10\,\mu\mathrm{A}$ and an aperture of $3\,\mu\mathrm{m}$. The Jeol 7000F (figure 3.15) is fitted with an Oxford Instruments INCA energy-dispersive X-ray spectroscopy (EDS) detector (Oxford Instruments plc, Oxfordshire, UK), this provides elemental composition data by analysing the X-ray spectra emitted by the specimen at the location of the incident electron beam. This can be used to separate contaminants from the debris when morphology is ambiguous.

FIGURE 3.15 – Jeol 7000f.

Hitachi TM3030

A Hitachi TM3030 (Hitachi Ltd., Tokyo, Japan) is a tabletop microscope which possesses only backscatter and a Bruker Quantax EDS (Bruker Corp., MA, USA) detectors. However it is capable of low pressure imaging and charge reduction capabilities, meaning it can image samples that have not been coated. This allows for quick and convenient imaging when a full sized microscope is not necessary i.e. high detailed full frame particle images are not required.

Once a particle was found and good focus was achieved (requiring the adjustment of both primary focus and astigmatism to find optimum focus), high quality images were created using a slow 26 second scan with no averaging.

[2] Different beam voltages were used as particles suffered from beam damage while being scanned. Beam voltage effects the distance an electron will penetrate a specimen, and therefore changes the image contrast and contrast effects (Joy and Joy, 1996). Since Scale-Invariant Feature Transforms (SIFT) normalises contrast gradient when generating features (Lowe, 2004), the effects of this should be minimal. All measurements in chapter 5 occured on images from the FEI with constant beam voltage, and so the difference in beam voltage had no effect (if any would have occured) on these measurements.

3.6 Alicona Infinite Focus 3D Coordinate System

The Alicona Infinite Focus is an optical microscope coupled with a sophisticated electronic stage and optics mount, enabling computerised x, y & z-control. By using accurate position data of the motorised x, y-stage and optics height, along with the working distance of lens in use; the inbuilt software can create a 3D topological map of the scanned surface that also contains true colour image data of the surface. This map was either analysed with the Alicona Infinite Focus software suite, for cases where surface roughness measurements were required, or exported to MATLAB for volume and sphericity measurements. For cases where surface roughness measurements were required, the specimen was scanned using the correct objective lens, and stage and wavelength cut-off filter settings for the expected roughness measurement according to BS ISO 4288:1998 (British Standards Institution, 1997). The lens and roughness parameters are shown in table 3.2:[3]

To transfer data from the Alicona to MATLAB, the data was

[3] *Alicona Reference Documentation* 2013.

TABLE 3.2 – Objective lens and vertical resolution settings for measurement of a given roughness. lenses marked with a * indicate a longer profile length needs to be used.

Roughness (μm) R_z	Roughness (μm) R_a	Vertical Resolution (μm)	Objective Lens
100	10	2	5x, 10x, 20x, 50x, 100x
50	5	1	5x*, 10x, 20x, 50x, 100x
10	1	0.2	10x*, 20x, 50x, 100x
5	0.5	0.1	20x*, 50x, 100x
1	0.1	0.02	50x*, 100x
0.5	0.05	0.01	100x

first exported into a plain text .csv file. This data was then imported into MATLAB using the script 'genAliconaImport.m' (Appendix A, MATLAB code A.4 p. 142). This script is capable of automating various plotting and mathematical functions.

To ensure data is comparable between scans, the 10x lens was used for all non-roughness measurements. Light settings were chosen as a compromise between various areas on the specimen—since not all areas will produce good data with the same light setting, this was especially obvious on areas of different gradient or roughness. The Alicona Infinite Focus does not have a global origin, therefore the 0 z-height had to be reset to the same position prior to each measurement. This was done by using a roughness standard, the standard used was a Rubert-Song reference specimen 501 X serial number P186 (Rubert & Co., Cheadle, UK), finding the z-position where the standard is in focus, and setting this to be the 0 plane. Additionally, data of the same specimen showing different stages of wear were realigned with each other using iterative closest point (ICP) (Wilm and Kjer, 2013). ICP will iteratively attempt to minimise the mean squared error of every point in a point cloud with the reference cloud. This method is prone to becoming trapped in local minimums, therefore it is vitally important to sanity check results. The accuracy of using the Alicona Infinite Focus with cubic interpolation of void data and realignment using ICP for the purpose of finding volume loss during wear tests was assessed by N. C. Green (School of Mechanical Engineering, University of Birmingham). The precision, found by realigning multiple scans of the same object and evaluating the difference of their volumes, is shown in table 3.3. An overview of this method is shown in figure 3.16.

TABLE 3.3 – Volumetric precision of Alicona Infinite Focus data realigned with ICP compared with the mass balance.

Mass balance precision, mm^3	Alicona volumetric precision, mm^3
25.4×10^{-3}	17.0×10^{-3}

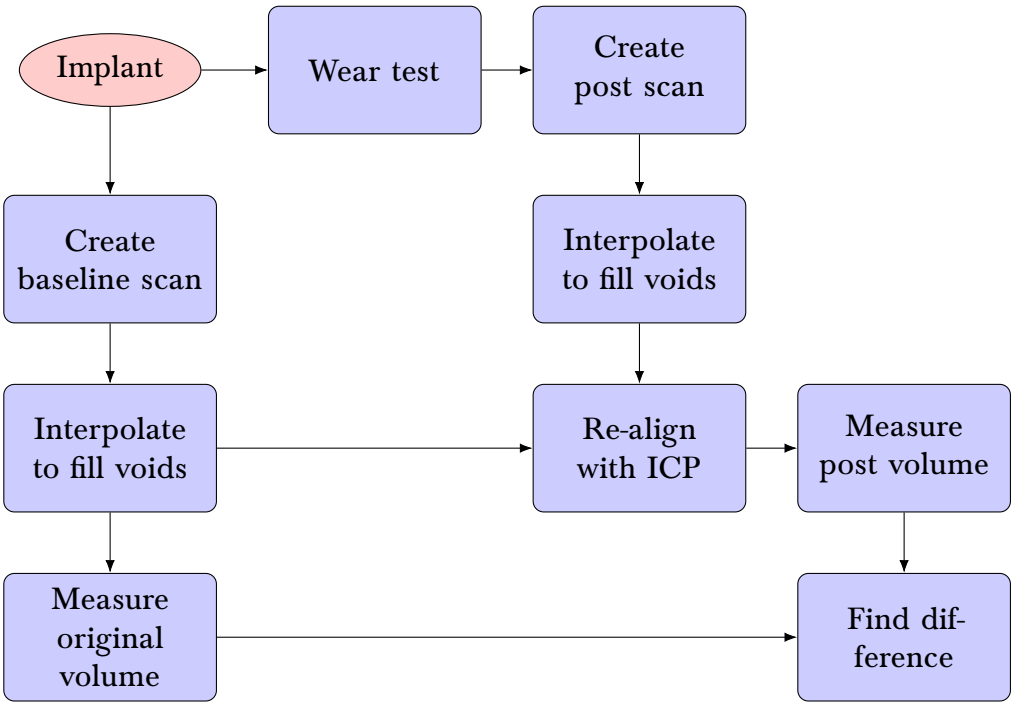

FIGURE 3.16 – A schematic overview of the process of finding volume difference data from Alicona scans after a wear test.

3.6.1 `genAliconaImport.m`

The preamble of the file, up to line 50, is the set-up for MATLAB's input parser, which was used so that the same file could be used to produce different outputs depending upon needs, e.g. if plotting was required, the interpolation method needed changing or volume measurements were necessary.

Between lines 56–80 was automatically generated by MATLAB's import data function, where it was given an example data file, and the parameters for cleaning the data were selected using a GUI, this was then converted into a general use function that was employed to import all Alicona Infinite Focus data.

Once the data had been split into three arrays, x, y & z, the step size between each incremental change in the x, y-grid (dx and dy) is needed. Lines 90–91, see code 3.1, was used to find the indices in the arrays where a change in value occurred,[4] it then finds the absolute difference between the value found at this index +1 and the value of the initial index.

CODE 3.1 – Lines 90–91 of `genAliconaImport.m` showing the implementation to find of dx and dy.

```
90 dx = abs(x(find(diff(x),1)+1)-x(1));
91 dy = abs(y(find(diff(y),1)+1)-y(1));
```

An issue found with the Alicona Infinite Focus data was that of voids in the data—where the microscope was unable to record any data. This had multiple causes, but generally, when the light settings did not provide adequate light for the sensor. Setting the light settings entailed compromising optimum light settings in one region to have suitable settings in another. Therefore it was impossible to get good settings over the entirety of the specimens.

$$\iint z(x, y)dxdy \tag{3.18}$$

To solve the double integral used to find the volume of measured parts (equation 3.18),[5] these voids needed to be filled, therefore an interpolant was used. See code 3.2. The default interpolant was a natural neighbour, to maintain continuity, however nearest neighbour and linear were available options. The extrapolant is set

[4] N.B. The `find(diff(-,1))` returns the index preceding the change in value, hence the +1

[5] This integral is the volume between the upper surface of the measured specimen, and the 0 z-plane of the Alicona Infinite Focus' coordinate system set using the reference standard

to 'none', to prevent the function inventing data beyond the region measured, which would produce unexpected results.

CODE 3.2 – Lines 104–106 of genAliconaImport.m showing the scattered interpolant function.

```
104 F = scatteredInterpolant(x, y, z,
    ↪ p.Results.interpolant, 'none');
105 [vx,vy] = ndgrid(xvg,yvg);
106 vz = F(vx,vy);
```

The double integral in equation 3.18 was solved numerically using the midpoint rule (equation 3.19) using line 111 (code 3.3). Note, the colon operator (:) concatenated the 2-dimension array, allowing just a single summation to perform the same output as a double sum.

$$\sum\sum z(x,y)\Delta x\Delta y \tag{3.19}$$

CODE 3.3 – Lines 110–111 of genAliconaImport.m that numerically solve equation 3.19

```
110 if p.Results.findVolume == 1
111     output = dx * dy * sum(vz(:));
```

3.7 Chapter Summary

To summarise, this chapter presented details of the material properties of UHMWPE, PEKK and the Charité implant along with the source of the materials. The UHMWPE discs are used in the HFRR for the generation of wear debris without contaminats from bovine serum. PEKK discs are manufactured in two designs, one for the HFRR and another for the Bose spinal simulators. Wear debris from

Charité implants is taken from the study by Moghadas, Mahomed, Shepherd, et al. (2015).

This chapter also included the general methods used in this thesis. The Spinal simulator used by Moghadas, Mahomed, Shepherd, et al. (2015) and Xin (2013) as well as for testing the PEKK implants is shown. The HFRR was used to create debris and perform other general tribometric tests.

For the analysis of wear debis, the bovine serum needed to be digested. This was done using HCl followed by filtering through nuclepore filters in a vacuum filtration system. The filter papers were then coated with a conductive medium (either gold or platinum) and examined on a SEM.

Finally, the Alicona Infinite Focus is used to measure surface morphology. The data from the Alicona is analysed in MATLAB to measure volume differences—and therefore the volume of wear scars.

Chapter 4

Wear Debris Analysis using Computer Vision

Chapter Overview

In This chapter, the characterisation of wear debris based on SEM images is presented. Computer techniques such as edge detection, image segmentation, key-point feature quantification and machine learning are employed. In §4.1 a brief introduction is given. In the method section (§4.2): §4.2.1 relates to the generation of wear debris, §4.2.2 is the SEM protocols. The process of image segmentation and edge detection is in §4.2.3, machine learning and computer are discussed in §4.2.4. The results, comprised of confusion matrices and receiver operating characteristic curves, are in §4.3. A discussion of the results can be found in §4.4, and a chapter conclusion in §4.5.

This chapter is based on a publication under review for ***Computer Methods in Biomechanics and Biomedical Engineering: Imaging & Visualization***

4.1 Introduction

Computer vision, granting a computer the ability to recognise objects from images, is a significant challenge in computer science. The task requires converting the qualitative information within an image into quantitative data that describes the contents. A good 'quantizer' will be invariant of context of the image (lighting and position) and transformations of the object (rotation or scaling). Without a good 'quantizer' it would not be possible to recognise the same object in different images—taken from different angles and in different contexts or lighting.

The characterisation of wear debris by their morphology is a subset of computer vision, however past research has concentrated on creating bespoke methods of analysing the debris. Examples include Partition-Iterated Function Systems (PIFS) developed by Stachowiak and Podsiadlo (1999) or wavelet based methods (Chen et al., 2006). These methods attempt to capitalise on various properties of wear debris (Kirk et al., 1995; Podsiadlo and Stachowiak, 2000; Zhang, Lu, et al., 1997). These methods have been shown to be extremely powerful, and have high success in terms of accuracy.

At the time of development of these classifiers, the field of computer vision was nascent and emerging methods and algorithms were performing relatively poorly (Boiman et al., 2008). However, advancement in the field has occurred quickly throughout the mid–late 2000s (Everingham et al., 2010).

There are two key areas of improvement within this field: that is the classifier, and the descriptor quantiser. The classifier is the mechanism for classifying objects based on the data fed to them;

these can be learning based, or non-parametric based. Common classifiers are Support Vector Machine (SVM) (Cortes and Vapnik, 1995; Zhang, Berg, et al., 2006), decision trees (Bosch et al., 2007) and Nearest-Neighbour (NN) (Boiman et al., 2008) based classifiers.

The descriptor quantiser is how the computer interprets the image and it is the algorithm that generates quantitative data about an image that describes what is pictured within. This can be as simple as colour histograms, or object size/aspect ratio, to more complex properties such as fractal dimensions, geometric-blur (Zhang, Berg, et al., 2006) or the descriptor quantiser used in this thesis—Scale-Invariant Feature Transforms (SIFT).

This chapter describes an implementation of, and the viability of using an open-source, but well-regarded and robust generic object recognition algorithm for the use of wear debris analysis from scanning electron microscope (SEM) micrographs. The aim is to introduce methodologies from outside disciplines with greater experience in computer vision, thereby allowing biomedical engineers and tribologists the opportunity to analyse SEM images without the need to reinvent tools found elsewhere. By removing the obstacle of creating a program that can recognise debris, greater comparison can be made between papers on the subject of wear debris analysis. The algorithm used in this chapter is known as SIFT, and was invented by Lowe, 2004; the implementation is known as VLFeat from the Oxford Vision Laboratory (Vedaldi and Fulkerson, 2010b,c).

The efficiency of assessing the debris images has been greatly increased, using a SIFT to extract key point data from individual images and a SVM. The SVM was trained to filter images of debris into appropriate morphologies, using wear particles generated from

idealised adhesion and abrasion tests. The debris morphology assessment tool is then used to examine how debris changes over the course of a 5 million cycle endurance test. The debris is compared against ultra-high molecular weight polyethylene (UHMWPE) debris generated in a reciprocating tribometer, using test parameters that would predominately run in specific wear regimes.

A flow chart giving an overview to the method presented in this chapter is shown in figure 4.1.

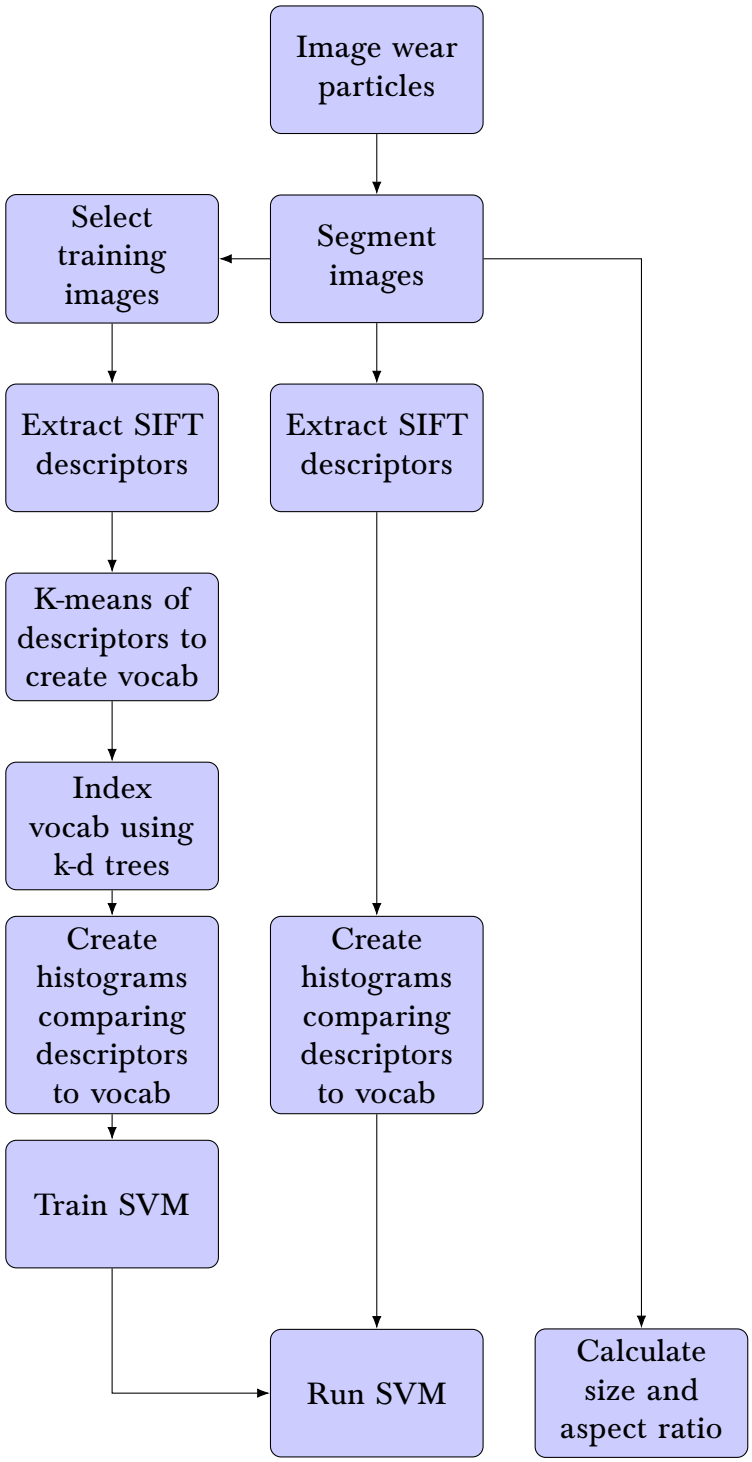

FIGURE 4.1 – A Schematic overview of the process of using computer vision to analyse wear debris.

4.2 Methods

4.2.1 Debris Generation

Wear debris was generated, isolated and imaged using SEM. The material used to generate the debris was UHMWPE and it was generated using two different methods: i. a high-frequency reciprocating rig (HFRR) (PCS Instruments, London, United Kingdom); or ii. a Bose ElectroForce Spinal Disc Fatigue/Wear system (SD-F/W) (Bose Corp., ElectroForce Systems Group, Eden Prairie, Minnesota, USA).

The UHMWPE was created in a study by Moghadas, Mahomed, Shepherd, et al. (2015) using the Bose SD-F/W to wear test a Charité total disc replacement (TDR) implant (see section 3.1.3). This study followed British Standards Institution (2011b) which is included in §3.2. This implant has two Cobalt Chrome Molybdenum alloy (CoCrMo) concave end-plates and a central convex UHMWPE core (figure 4.2). The lubricant in the Bose SD-F/W was Bovine serum albumin ($30\,\mathrm{g\,l^{-1}}$ protein content) (Sera Laboratories Int, West Sussex, United Kingdom).

The HFRR is a simple linear reciprocating motion ball on disc tribometer, using a $6\,\mathrm{mm}$ diameter steel ball (PCS Instruments, London, United Kingdom) on GUR 1120 UHMWPE discs (Orthoplastics, Lancaster, UK). The method for generating adhesive and

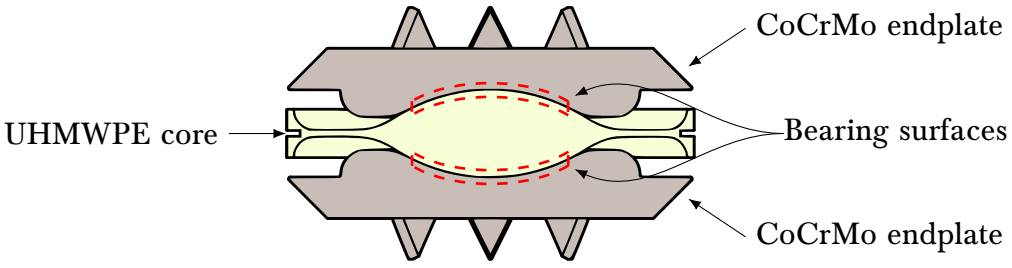

FIGURE 4.2 – Illustration of the cross-section of a Charité implant.

abrasive debris using the HFRR is described in §3.3.

The wear debris was collected from the lubricants through vacuum filtration. The bovine serum was first digested to remove attached proteins and other biological contaminants found in bovine serum using the hydrochloric acid (HCl) method outlined in BS ISO 17853:2011 (British Standards Institution, 2011a, p. 9). This method uses hydrochloric acid at $50\,^{\circ}\mathrm{C}$ to digest the biological content in bovine serum albumin; it was then diluted with methanol to reduce the viscosity enough for filtering. For the detailed method of bovine digestion and filtration, please see §3.4.

Subsequent to digestion, the debris containing fluids were filtered through $0.1\,\mu\mathrm{m}$ Nucle-pore filters (Whatman International Ltd, Maidstone, United Kingdom) in a vacuum filtration system, and then were mounted on an SEM aluminium stub and sputter coated in gold for using an Agar automatic sputter coater (Agar Scientific, Elektron Technology UK Ltd, Essex, United Kingdom) (see §3.5).

4.2.2 SEM Imaging

SEM images were taken on either a Jeol 7000F FEG-SEM (Jeol Ltd., Tokyo, Japan) or an FEI Dualbeam FIB-SEM (FEI, Hillsboro, Oregon, USA). Electron voltages were $10\,\mathrm{kV}$ unless the debris started to suffer from beam damage (e.g. swelling or cracking), in which case the beam voltage was lowered to $5\,\mathrm{kV}$. Secondary electron images were collected from the typical Everhart-Thornley detector on the Jeol 7000F, however, images generated by the FEI system used the 'through-lens detector' (TLD) on 'ultra-high resolution' (UHR) mode.

Images were focused, astigmatism was corrected for and the magnification was chosen to achieve a full frame image of the particle. A long scan of 26 s was taken without averaging to produce a clear, low noise image that was saved as a .tif file.

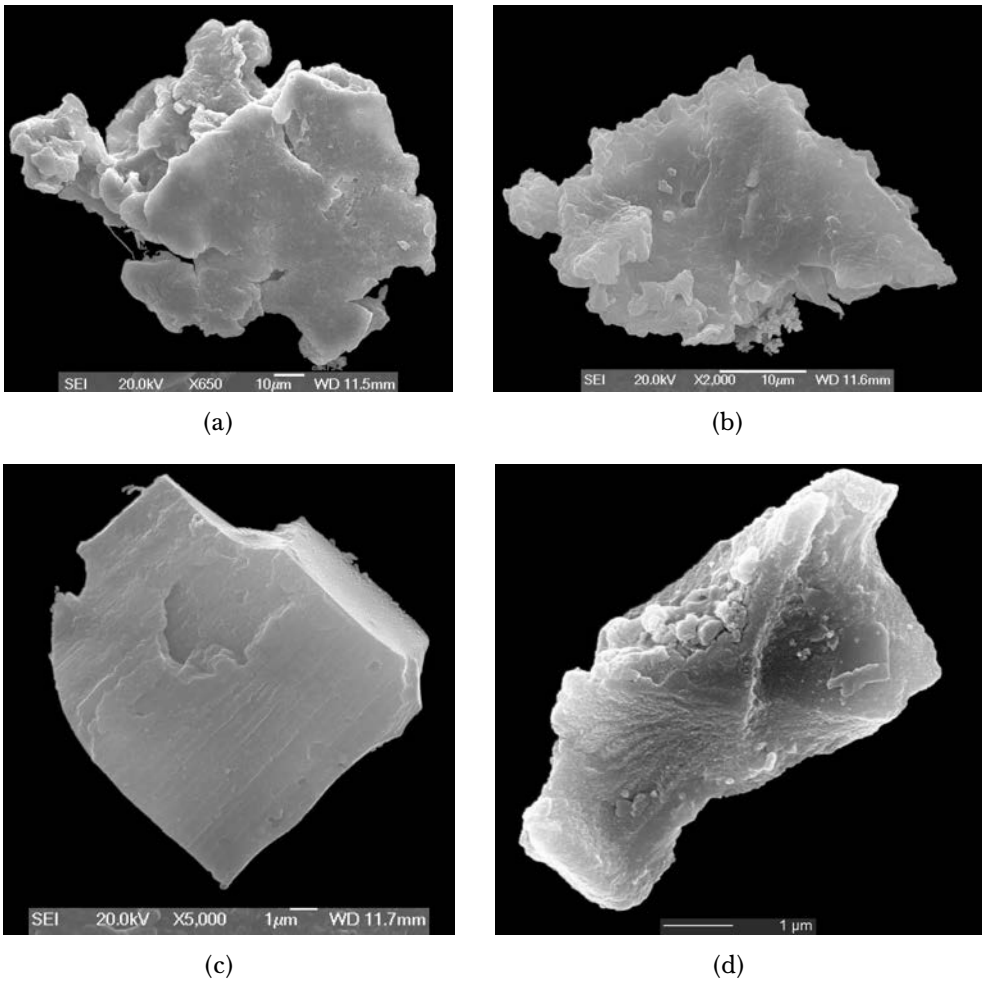

(a) (b)

(c) (d)

FIGURE 4.3 – Figures (a)–(b) are example training images for the adhesion class. Figures ((c)–(d) are examples of debris of the chip class.

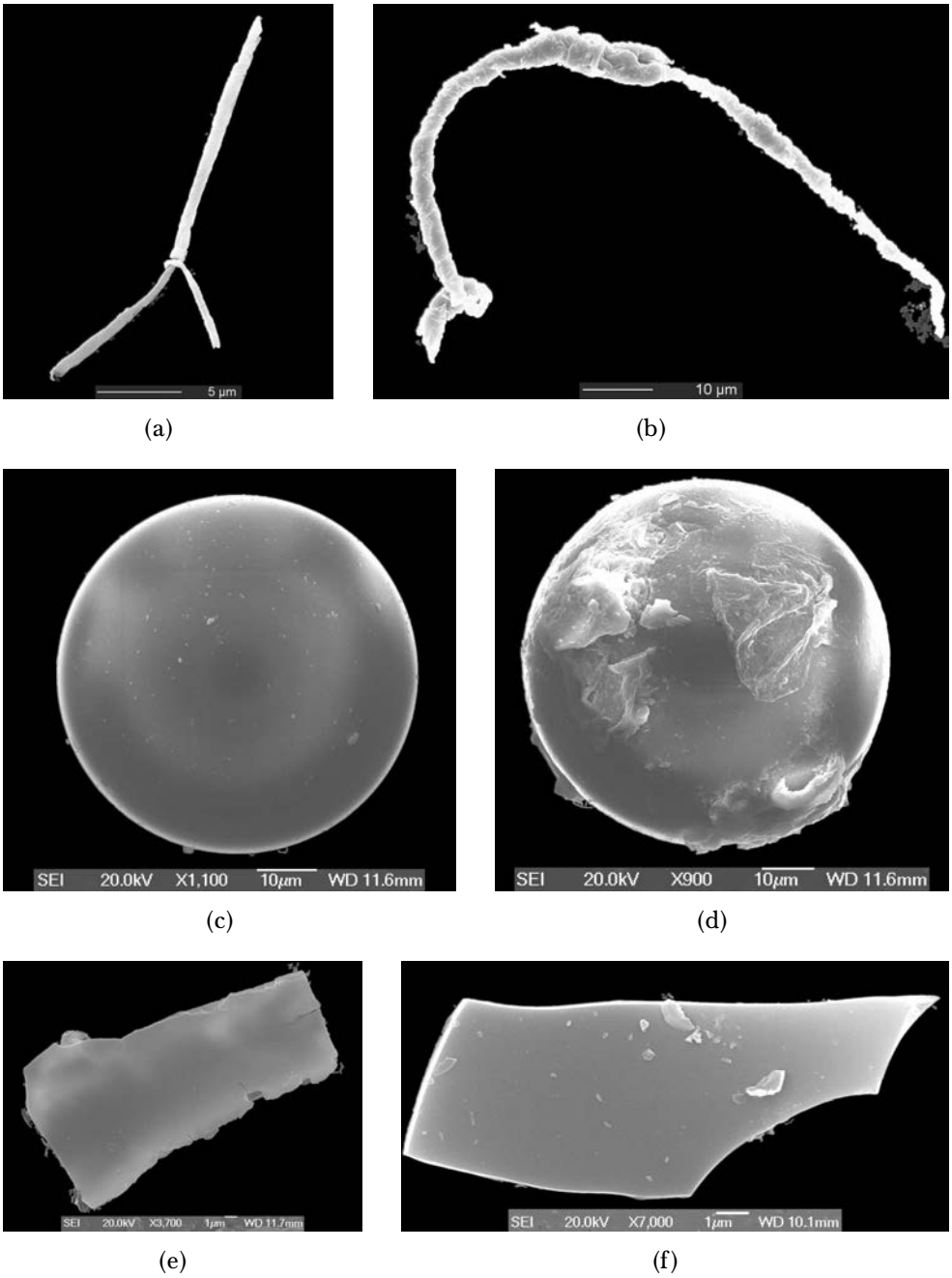

FIGURE 4.4 – Figures (a)–(b) are examples of debris of the fibril class, (c)–(d) are large spherical debris and figures (e)–(f) are sheets/flake debris.

4.2.3 Image Processing & Background Removal

Images were analysed in MATLAB (MathWorks, Natick, Massachusetts, USA) using the Image Processing Toolbox. The size, aspect ratio, and wear particle morphology were calculated using

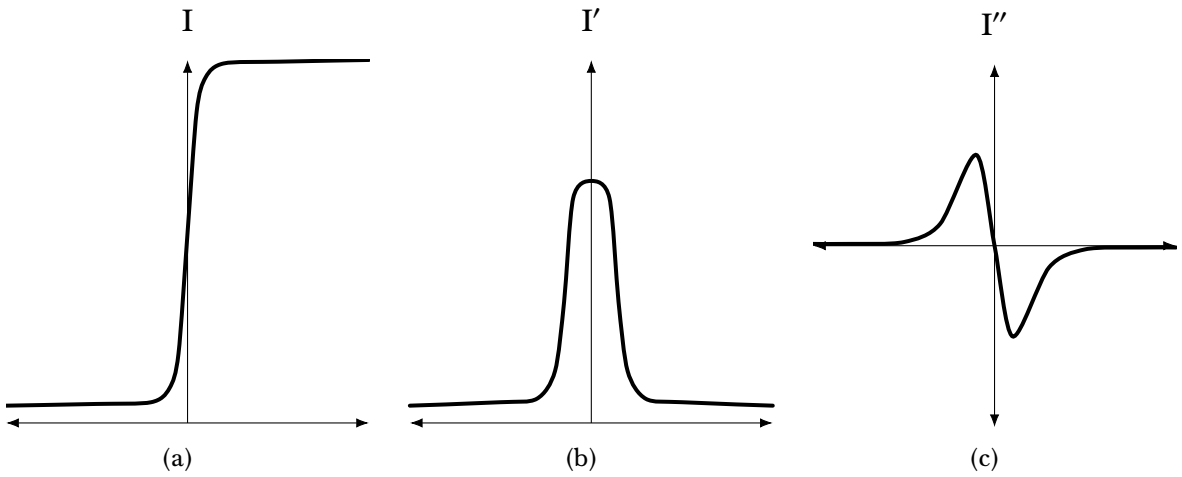

FIGURE 4.5 – Demonstration of how double differentiation and zero-crossing can find edges in an intensity map. (a) shows an example of intensity data of a line perpendicular to an edge. (b) shows the first derivative, and ((c)) shows the second derivative. Where the line crosses zero in (c) is the location of the edge.

the VLFeat library (Vedaldi and Fulkerson, 2010c).

The size and shape of the particles were assessed by examining the region properties of the foreground of a binary image of the particles, created using either 'Sobel' or 'Canny' edge detection algorithms, to segment the particles from the background areas. Sobel edge detection is more computationally efficient, but less able to deal with weak edges. Canny edge detection uses a two step process to improve weak edge performance without introducing noise. First a low sensitivity threshold is used to detect strong edges, this is followed by a high sensitivity threshold—but only in areas at the end of a strong edge so to bridge weak edge gaps. Edge detection uses calculus to find gradients in pixel intensity, the 'Sobel' detector will find edges using intensity values in a 3×3 grid around each pixel to approximate the gradient function. This function is then differentiated (see figure 4.5(b)) and a threshold value defines what is and is not an edge.

The code used to remove the background of an image and detect

particle size is shown in code snippet 4.1. This example uses the Canny method, once edges are detected, the image is dilated to fill in gaps and smooth edges (Gonzalez et al., 2009). Enclosed rings of edges in the logical array are then filled and small objects (only a few pixels in size which are likely either noise or parts of the background) are removed along with objects that are only partially in the image. The resulting logical array is then multiplied with the original image, effectively deleting all but the particle in the image.

CODE 4.1 – MATLAB script for the removal of the background of an SEM image.

```
function [ output ] = Background_removal( particle_image )
    I = imread( particle_image ); %loads image
    BWs = edge( I, 'canny' ); % Use "canny" algorithm to find
↪   edges
    se90 = strel( 'line', 4, 90 );
    se0 = strel( 'line', 4, 0 );
    BWsdil = imdilate( BWs, [se90 se0] ); % dilate lines to
↪   remove gaps
    BWdfill = imfill( BWsdil, 'holes' ); % Fill in holes
    BWfiltered = bwareaopen( BWdfill, 30000 ); %remove shapes
↪   below certain area
    seD = strel( 'diamond', 3 ); %smooth edges
    BWsmoothed = imerode( BWfiltered, seD );
    BWfinal = bwareaopen( BWsmoothed, 10000 ); %remove small
↪   shapes that were cut off
    output = immultiply( I, BWfinal ); % multiply origonal
↪   image by binary image
end
```

Once an image is segmented into background and particle, the area in pixels can be extracted and scaled against the scale bar. The particle size was then determined using Equation 4.1 given below, and aspect ratio was calculated following ASTM F1877-05 (American Society for Testing and Materials, 2009).

$$\text{ECD} = \sqrt{\frac{4 \times n_p}{\pi} \times \left(\frac{s_m}{s_p}\right)^2} \tag{4.1}$$

where, n_p is the number of white pixels in the binary image, s_m is the length of the scale bar in μm and s_p is the length of the scale bar in pixels. The units of ECD are μm.

The images were sorted into classes based on the following criteria:

Adhesion – Wear debris generated by the HFRR in the smooth ball, higher frequency setting. (figures 4.3(a)–4.3(b))

Chip – Wear debris generated by the HFRR in the rough ball setting. (figures 4.3(c)–4.3(d))

Fibril – Wear debris that have formed into long fibrils with high aspect ratio. (figures 4.4(a)–4.4(b))

Large Sphere – Wear debris that was of $> 5\,\mu\text{m}$ in diameter and it appears to be of a spherical shape. (figures 4.4(c)–4.4(d))

Flake – Wear debris that appear flat and sheet-like. (figures 4.4(e)–4.4(f))

Images were processed using the MATLAB image processing toolbox to remove the background. This ensures that features on the filter that may be common between different images, did not cause erroneous positive matches not based on the particle morphology. The background was removed from the image by edge based image segmentation and the outline of the particle was found using 'Canny' Edge detection, any pixels that lie outside this outline were replaced

with zeros. This algorithm was used as it had greater robustness when presented with edges that have weak sections, i.e. difficult for a computer to distinguish from noise (Canny, 1986). However, it was vital for images to be in focus and of high quality in terms of brightness and contrast for edge detection to work satisfactory. The largest connected binary object was found and image multiplication was used to set the background intensity value to zero. Examples of wear debris once the background have been stripped are shown in figures 4.3 and 4.4.

4.2.4 Machine Learning

SIFT descriptors were generated of the images. The descriptors have the form of a 128 dimension vector, with the Euclidean distance between a pair of descriptors being a measure of how similar the key points they represent are. The visualisation of a selection of descriptors is shown in figure 4.6.

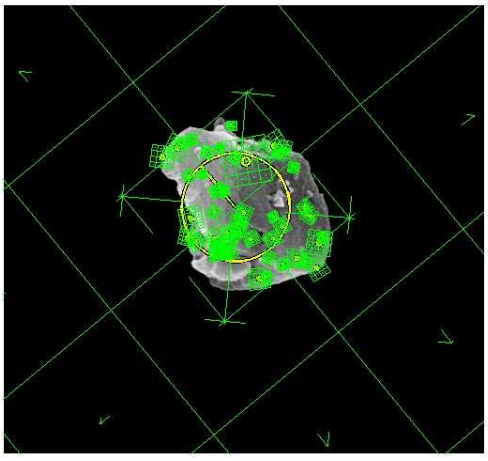

FIGURE 4.6 – A wear Particle showing a selection of Sift Descriptors and Frames.

Five Images of each class were selected randomly without replacement to be training images.

To increase computational efficiency, rather than comparing the

descriptors of unknown images against the entirety of the descriptor data of the training images, clusters of similar descriptors were found and averaged. The individual means of these clusters form the 'words' used in the solver's vocabulary and this is known as a 'bag of words' method. An example using 4 clusters of random coordinate data is shown in figure 4.7, the blue dots are the cluster means, and the lines are the Voronoi polygons that divide the clusters.

FIGURE 4.7 – Example of k-means clustering using 4 clusters of normally distributed random coordinates (black dots). The blue dots are the cluster means and the lines are the Voronoi polygons which partition the clusters.

To generate the 'words' used to describe the particles, all the descriptors were concatenated, and the means of the clusters of descriptors were found. The mean value for each cluster was found using a k-means algorithm (Hartigan and Wong, 1979), where k is the number of 'words.' An amount of 'words' were chosen based on a preliminary study, measuring the accuracy of the solver and computational time. As shown in figure 4.9, the complexity was linear with respect to the number of 'words', but the accuracy did not improve beyond 600 'words'.

For rapid nearest-neighbour searches, i.e. finding the closest matching 'word' for the descriptor in Euclidean space, the vocabulary was indexed by generating a k-d tree (Bentley, 1975). This is an efficient way to find the 'word' with the shortest orthogonal distance between descriptor vectors.

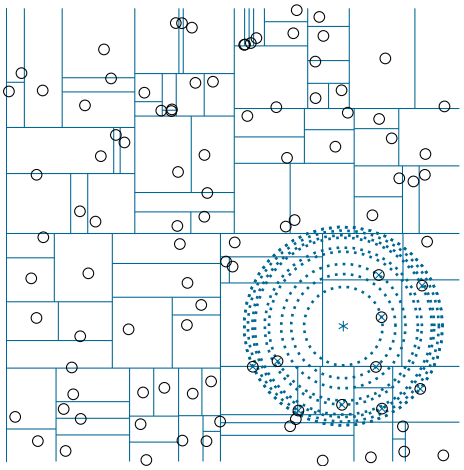

FIGURE 4.8 – Example of kd-tree indexing. The black circles are uniformly distributed random points, the blue lines are the kd-tree partitions. The 10 closest neighbours to the point shown by the astrix is shown by the dashed blue circles.

To make comparisons between images of how far their descriptors differ from the 'words' efficiently, the closest match (which did not exceed a threshold) were tallied and a histogram of how many descriptors matched what 'word' was computed. The histogram can be seen as a compact précis of the descriptor data.

The SVM is a binary solver—it only categorises something as belonging to a class, or that it does not. To train the SVM it requires both the histograms of the training image which belong to a class, and all of the training histograms that do not.

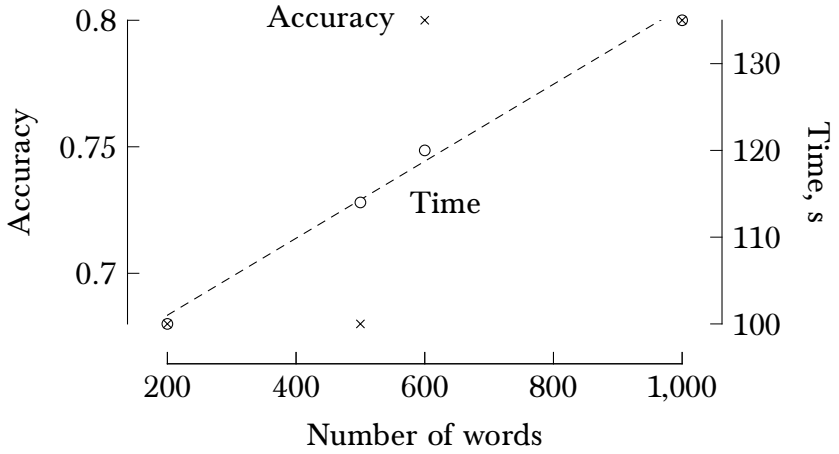

FIGURE 4.9 – Accuracy and time against number of 'words' in vocabulary. Note the time increases linearly with the number of 'words', but accuracy was constant except for the step increase at 600 'words'.

Performance analysis

By varying the seed used in the pseudo-random number generator, different images were selected for training and testing, the accuracy of the image classification algorithm was assessed using different combinations of training and test images. The process of training and assessing images was repeated five times with different seeds and averaging the results; the number of matches for each class was then found.

The number of matches found was subdivided into which class the image truly belonged to, thereby generating a confusion matrix of true and false positives.

4.3 Results

4.3.1 Accuracy

Table 4.1 shows the overall accuracy of the SVM for all the classes combined ± the standard deviation, the accuracy was $77.60 \pm 4.56\,\%$. The accuracy was found by taking the mean of the true positives (the diagonal of the confusion matrix [table 4.2]) of the solver.

TABLE 4.1 – Accuracy of SVM. Average accuracy = $77.60 \pm 4.56\,\%$

Random Seed	1	2	3	4	5
Accuracy	80 %	76 %	76 %	72 %	84 %

4.3.2 Confusion Matrix

Table 4.2 shows the confusion matrix, which shows the percentage of images found to be a match by the SVM. The rows show which class of debris the SVM was classifying for, and the columns show

how many matches were found from each class the image actually belongs to.

TABLE 4.2 – Confusion matrix of SVM. Rows indicate the particle class the SVM has been trained to find and columns indicate percent of particles determined to be a match.

	Large Sphere	Adhesion	Fibril	Chip	Sheet
Large Sphere	100	0	0	0	0
Adhesion	0	100	0	0	0
Fibril	0	20	68	0	12
Chip	16	20	0	64	0
Sheet	4	0	16	24	56

4.3.3 ROC Curves

Figures 4.10–4.11 show the ROC curves for each class of debris. The ROC curves shown are a measure of the true positive rate (recall) against true negative rate at different discrimination thresholds. A good classifier will have both a high rate of true positives and true negatives (the area under curve (AUC) will approach 100 %). Random chance is shown with a dashed red line and the performance of the classifier is the solid blue line.

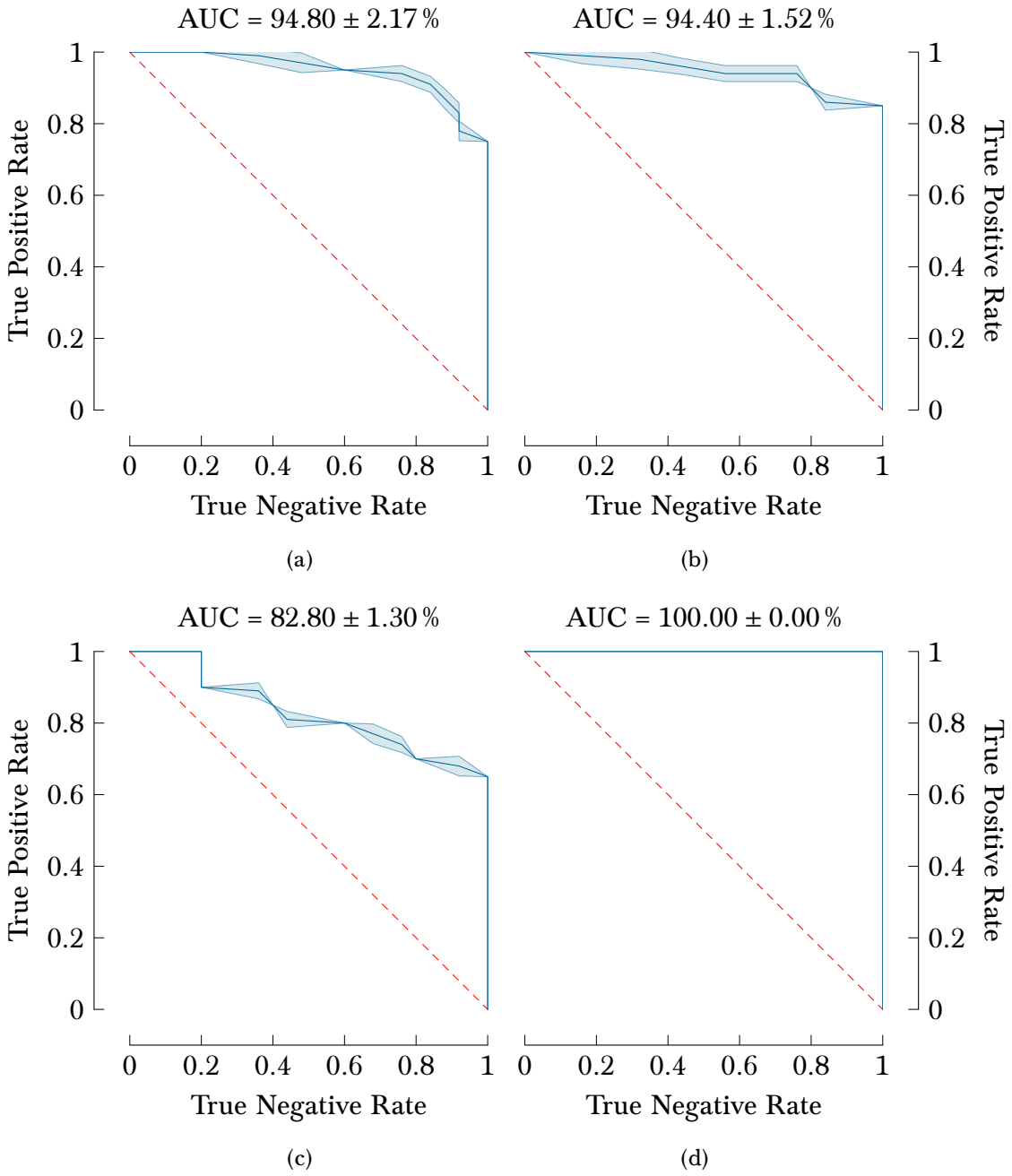

FIGURE 4.10 – ROC curves of the SVM for each class. (a) is the ROC curve for fibril debris classification, (b) is the ROC curve for adhesive particle classification. The ROC curve for chips is figure (c) and the ROC curve for spherical particles is (d). The dashed red line (--) is a ROC curve of random chance, the blue line (—) is the mean ROC curve and the shaded area is the standard deviation of the mean curve. AUC = area under curve.

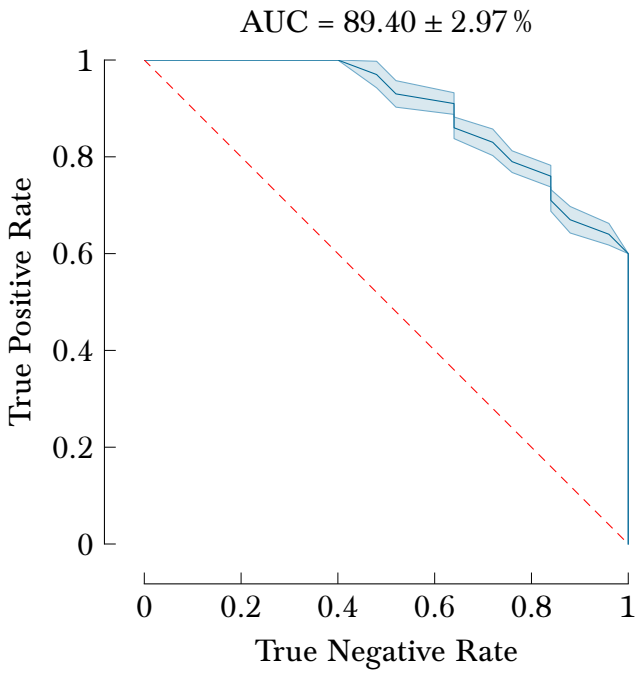

FIGURE 4.11 – The ROC curve for sheets/flakes. The dashed red line (--) is a ROC curve of random chance, the blue line (—) is the mean ROC curve and the shaded area is the standard deviation of the mean curve. AUC = area under curve.

4.4 Discussion

This study has examined the suitability of SIFT and a parametric classification algorithm typically used for general computer vision, applied specifically for the use of wear debris analysis. It assesses the overall accuracy, as well as the response within each class of wear debris.

The use of image analysis and machine learning for the automated characterization of debris greatly speeds up the analysis of large quantities of SEM images. It has been shown that the use of general computer vision techniques are applicable for examining micrographs of wear debris when given training images of different debris morphologies, and is comparable to bespoke methodologies (Kumar, Mukherjee, et al., 2013; Stachowiak, Stachowiak, et al., 2008). While computers have long been used to do basic analysis for finding size, aspect ratio and roundness of particles, the recognition of what an image contains remains a challenging problem in all fields of computer science. By using more general machine learning and image analysis tools than those used in previous studies of debris analysis, the breakthroughs discovered outside of the field of tribology can be re-purposed for examining wear debris with greater accuracy and with fewer inefficiencies attempting to recreate redundant methods.

While debris analysis commonly suffers from the subjective nature of interpreting images, by training a computer vision algorithm using debris either of pronounced class, or generated in a sterile environment that greatly favours certain wear regimes, characterising the debris with known confidence levels is possible.

4.4.1 Accuracy

The overall accuracy of this method, shows a high rate of classification accuracy, correctly identifying debris 77.6 % of the time. An accuracy of 77.6 % was in-line with the capabilities of similar methods using the same descriptor generation and classifier when performed on the caltech-101 and the PASCAL VOC 2007 classification challenge (Chatfield et al., 2011; Vedaldi and Fulkerson, 2010a). It was found that the accuracy does vary between different random seeds, implying that the quality of training images has some impact on the accuracy of the SVM.

4.4.2 Confusion Matrix

The SVM achieves good accuracy (100 %) for feature rich debris (adhesion [figure 4.3(a)–4.3(b)] and large spheres[figure 4.4(c)–4.4(d)]), and reasonable accuracy for fibrils [figure 4.4(a)–4.4(b)] and chips [figure 4.3(c)–4.3(d)] (64–68 %), especially considering only a single descriptor type was used for characterisation. However, for feature poor debris like sheet/flakes [figure 4.4(e)–4.4(f)] the classifier accuracy was <60 % (although still better than chance). It is possible with the use of a more sophisticated classifier, for example, one that uses multiple metrics to describe the image, that the classification will be less prone to error when analysing particles with few key features.

4.4.3 ROC Curves

As shown in figure 4.10, the ROC curves for large spheres, fibrils and adhesive particles are all >90 %; demonstrating the SVM is highly capable, correctly identifying debris of these morphologies without

erroneously including incorrect matches. The AUC for sheets and chips was >80 %.

4.4.4 Applications to Biomedical Engineering

The field of biomedical engineering places great importance on wear debris analysis, since the debris have such a pronounced effect on the life of an implant (Green, Fisher, Bridget Matthews, et al., 2000; Harris, 1995; Ingham and Fisher, 2000). However, comparisons between papers from different research groups is challenging—both due to the subjective nature of debris characterisation and the variety of methodologies used. Some efforts have been made to create debris quantifiers, but these have yet to be adopted by the community as a whole, despite the methods having been published for some time (Kumar, Mukherjee, et al., 2013). It is the intention that by demonstrating the viability of using freely available machine learning and computer vision techniques developed by specialists in computer science, tribologists will be able to produce, and reproduce comparable results without the need to perform redundant development of complex computer algorithms to analyse images.

4.5 Chapter Summary

This chapter has investigated the accuracy of using an SVM classifier to characterise SEM images quantised with SIFT descriptors. The general conclusions of this chapter were:

- The overall accuracy was $77.6 \pm 4.6\,\%$.
- The average AUC of the ROC curves was $92.28 \pm 6.49\,\%$.

- Debris classes that contained particles which had many morphological features were classified at a greater rate with fewer false positives than classes with fewer features.

Overall the performance was good, but further work to improve on the ideas in this chapter could include using a multivariate classifier, incorporating data from multiple quantifications (e.g. size and aspect ratio data in addition to SIFT) of debris to classify images. It will be important to maintain 'up to data' knowledge of literature in computer vision to take advantage of relevant improvements as they are discovered, for example improving illumination invariance and reducing computational complexity (Alitappeh et al., 2012).

Chapter 5

The Evolution of UHMWPE Wear Debris in *In Vitro* Simulation

Chapter Overview

In this chapter, the size, shape and morphology of UHMWPE wear debris from Charité Total Disc Replacements was studied in detail through the use of computer vision and electron microscopy. An introduction to the study is presented in §5.1, §5.2 presents the materials and methods specific to this chapter. The results and discussion are §§5.3–5.4, respectively. A conclusion is given in §5.5.

This chapter is based on the publication: D. G. Eckold et al. (2015). "The evolution of polymer wear debris from total disc arthroplasty". In: ***Biotribology*** 1–2, pp. 42–50.

5.1 Introduction

Ultra-high molecular weight polyethylene (UHMWPE) is currently used in the SB Charité and PRODISC-L total disc replacements (TDRs), both made by DePuy Synthes Spine (Raynham, MA, USA). These material choices were grandfathered in from hip and knee implant design, where the polymer on metal combination has had decades of success since John Charnley introduced his low-friction implant in 1962 (Charnley, 1972).

In this chapter, the wear debris from a 5 million cycle *in vitro* wear test of a Charité implant was examined using computer vision techniques described in chapter 4. The Charité was the first available TDR (Lu, Hai, et al., 2015; Putzier et al., 2006), and as such has been studied in clinical trials extensively, however there are fewer *in vitro* studies of TDRs than hips and knees, and even fewer on the wear debris.

The wear debris can subsequently be compared with what is known to occur in other joint replacements, such as those reviewed by Nine et al. (2014). In addition to comparisons of form, the wealth of studies into the biological effects of debris of various materials, sizes and shapes is also of great relevance to spinal arthroplasty. The debris and wear scars seen from revision and reclamation surgeries of Charité implants can also be compared—demonstrating whether the *in vitro* studies accurately recreate the tribology that occurs *in vivo*.

5.2 Materials and Methods

5.2.1 *In Vitro* Wear Tests

In vitro wear debris was generated by Moghadas, Mahomed, Shepherd, et al. (2015), using a Charité TDR (figure 4.2, see §3.1.3). The study involved long term wear tests where the lubricant containing wear debris was replaced at 12 intervals over 5 million cycles. The tests were conducted using a Bose ElectroForce Spinal Disc Fatigue/Wear system (SD-F/W). The implant was run in a bath of $30\,\mathrm{g\,l^{-1}}$ calf bovine serum lubricant (Sera Laboratories Int, West Sussex, United Kingdom) according to BS ISO standard 18192-1:2011 (British Standards Institution, 2011b), this is outlined in §3.2 page 32. The lubricant samples were taken at the following cycle counts: 0.25, 0.75, 1, 1.25, 1.5, 1.75, 2, 2.25, 2.5, 3, 4 and 5 million cycles. The bovine serum samples were refrigerated at $4\,^{\circ}\mathrm{C}$ until the debris was isolated and analysed.

5.2.2 High Frequency Reciprocating Rig

To generate wear debris of specific morphologies, the high-frequency reciprocating rig (HFRR) was employed using deionised water as a lubricant. This was to generate abrasion and adhesion wear debris to train the parametric classifier discussed in Chapter 4. The procedure for using the HFRR is described in §3.3, using UHMWPE specimens detailed in §3.1.1.

5.2.3 Wear Debris Analysis

Once digested by the method in §3.4 page 46, the wear debris were imaged using an FEI dualbeam FEG-SEM with the process outlined

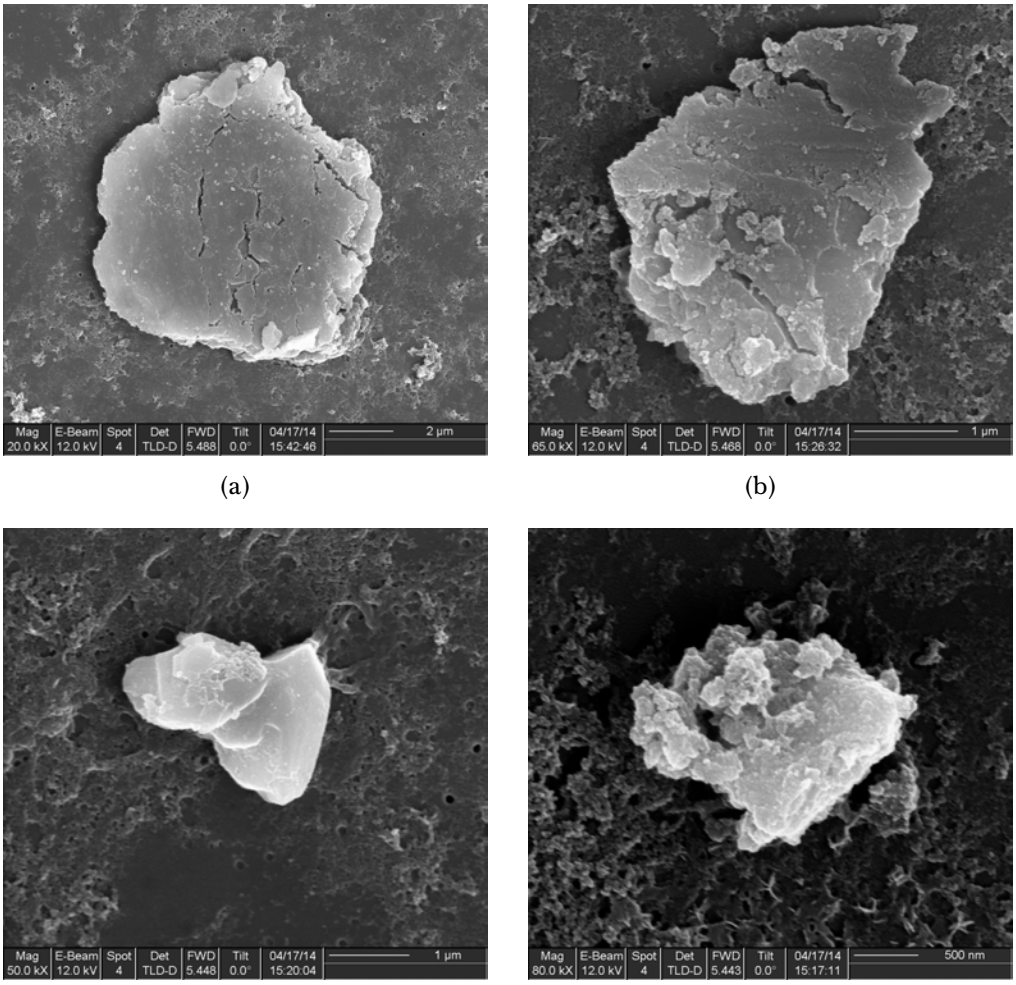

(a) (b)

(c) (d)

FIGURE 5.1 – Example particles for training of adhesion: (a) and (b); and abrasion: (c) and ((d)).

in §3.5 page 47. A total of 480 images were taken of the wear debris from the *in vitro* simulation, 40 of each lubricant sample in addition to 20 training images from the HFRR tests (see §3.3 page 36). A Support Vector Machine (SVM) was used to classify these images into the following classes based on the training images shown in figures 5.1 and 5.2.

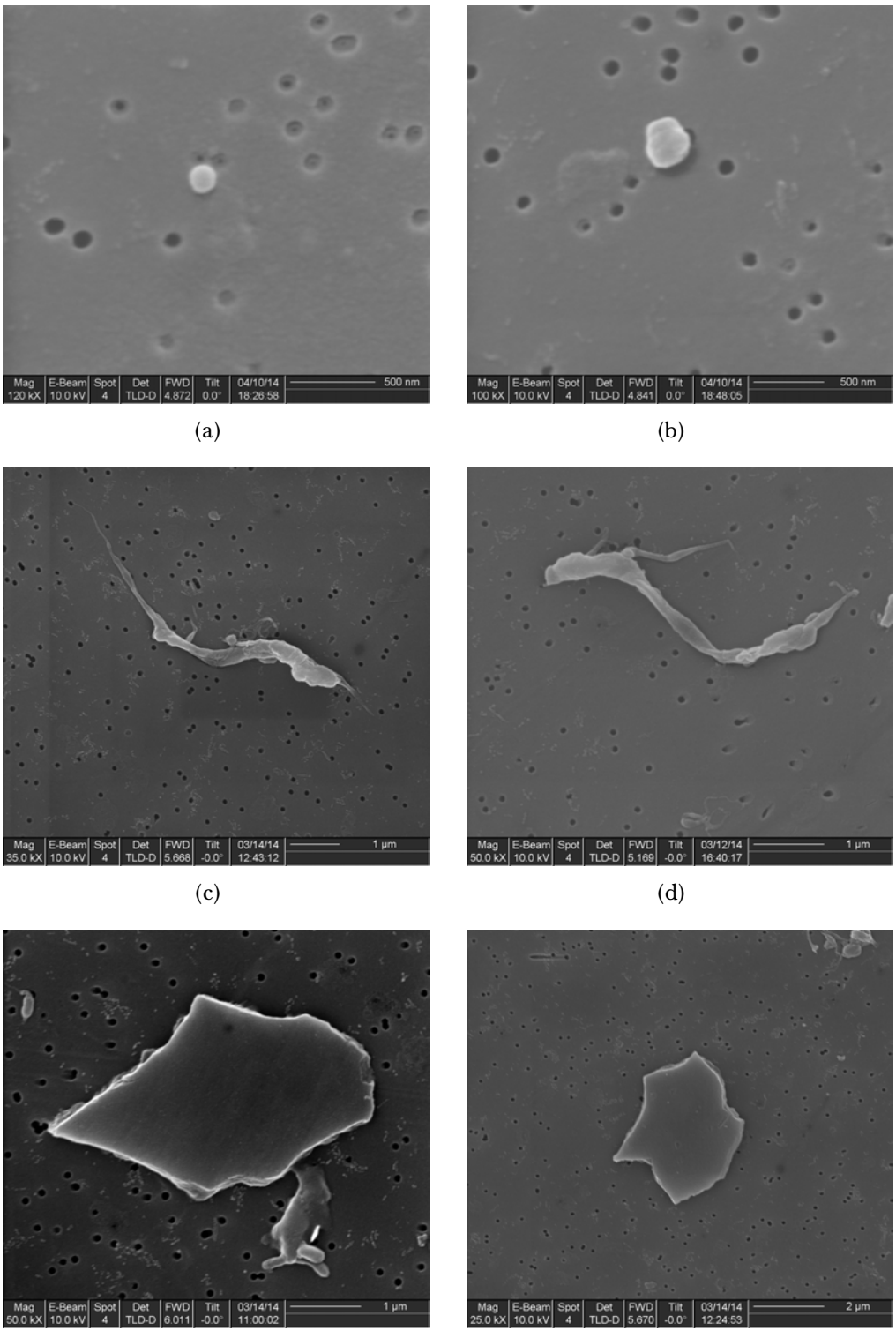

(a) (b)

(c) (d)

(e) (f)

FIGURE 5.2 – SEM Micrographs of debris of the following morphologies: small spheres, (a) and (b); fibrils, (c) and (d) and flake debris, (e) and (f).

Figures 5.1(a)–5.1(b)

Shows debris generated by adhesion—Images of adhesive wear debris are taken from the HFRR test using high speed and a smooth ball (can be of any size).

Figures 5.1(c)–5.1(d)

Shows debris generated by abrasion—Images of abrasive wear are taken from the HFRR test using a roughened ball (typically medium sized {between 1 and $10\,\mu\mathrm{m}$}, with a low aspect ratio).

Figures 5.2(a)–5.2(b)

Shows Spherical debris—Training images of micro-spheres are taken from *in vitro* simulation debris images, chosen based on clarity of image (focus, contrast and brightness) and the obviousness of belonging to that specified morphological class (typically very small {less than $1\,\mu\mathrm{m}$}).

Figures 5.2(c)–5.2(d)

Fibril debris—Training images of fibrils are taken from *in vitro* simulation debris images chosen based on clarity of image (focus, contrast and brightness) and the obviousness of belonging to that specified morphological class (typically medium to large greater than $10\,\mu\mathrm{m}$, and of high aspect ratio).

Figures 5.2(e)–5.2(f)

Sheet/Flake debris—Training images of sheet/Flakes are taken from *in vitro* simulation debris images chosen based on clarity of image (focus, contrast and brightness) and the obviousness of belonging to that specified morphological class. (typically medium sized between 1 and $10\,\mu\mathrm{m}$, with a medium aspect ratio).

The size of wear debris was computed using edge detection, as described in §4.2.3, to segment images into foreground and background areas. The pixel area of the foreground, i.e. the wear particle, was then converted to an equivalent circle diameter (ECD) using equation 4.1.

Once particle sizes and aspect ratios were calculated, a statistical distribution was fitted[1] using the 'fitdist' function in R (R Core Team, 2014) and the 'fitdistrplus' package (Delignette-Muller and Dutang, 2015), the appropriateness of this distribution was assessed using a one-sample Kolmogorov-Smirnov test, where any p-value >0.050 implies the data could belong to the named distribution. The distribution parameters and confidence intervals were calculated by bootstrapping[2] the resultant distribution with 1000 re-samples and using a parametric method (see code 5.1).

The total number of particles was also calculated using Equation 5.1, with the mass lost taken directly from Moghadas, Mahomed, Shepherd, et al. (2015) and Moghadas (2012). This equation was solved in R using a *Monte Carlo* simulation with 50×10^3 simulations. The mean and confidence intervals were then found by bootstrapping as above (see code 5.2).

$$n_{\text{total}} = \frac{N(M_{\text{lost}})}{\frac{\pi}{6}\overline{\log N(ECD)}^3 \times \rho} \tag{5.1}$$

where, n_{total} is the total number of particles, $N(M_{\text{lost}})$ is the normally distributed mass lost, $\overline{\log N(ECD)}$ is the mean of the log-normal

[1] Note, a log-normal distribution necessitates starting at 0, however, since the aspect ratio must be ≥ 1, the data was temporarily shifted by -1 in aspect ratio for fitting, and then the distribution was shifted back by 1 in the x-axis

[2] Bootstrapping is a non-parametric method for calculating statistical parameters and confidence intervals by using random re-sampling (Efron, 1979).

distribution of particle diameters in each sample, and ρ is the density of the debris material.

The distribution M_{lost} had parameters $\mu = 12$ µm and $\sigma = 1.4$ µm (Moghadas, 2012). For the total mass loss, the ECD distribution parameters were found using the bootstrap method as explained in the previous paragraph.

Code 5.1 – R code for fitting log normal distributions to ECD data.

```
fitECD.lnorm <- fitdist(datECD, "lnorm", method = "mle") # fit
↪  lnorm distribution using maximum likelihood estimations
fitECD.boot <- bootdist(fitECD.lnorm, bootmethod = "param",
↪  niter = 1000) # Bootstrap fitted distribution
↪  parametrically with 1000 iterations.
summary(fitECD.boot) # show fit parameters and confidence
↪  intervals.
```

Code 5.2 – R code for *monte carlo* solution to number of particles produced.

```
n.sims <- 5e4
no <- replicate(n.sims, {
  d <- rlnorm(n = 1000
              , meanlog = fitECD.boot$CI[1, 1]
              , sdlog = fitECD.boot$CI[2, 1]
  ) # generate lnorm distribution using fitted parameters from
↪  bootstrap
  m <- rnorm(n = 1, mean = 12, sd = 1.4) # generate normal
↪  distribution for weight loss
 m*5e-6/((pi/6)*0.93*(mean(d)*1e-6)^3) # solve
↪  n_total = (5×10^-6×N(12,1.4)) / ((0.93π/6)·log N(ECD)^3)
})
```

The classification of wear debris was performed by using Scale-Invariant Feature Transforms (SIFT) as an image quantiser, and a SVM for each particle morphology as described in Chapter 4. The

SVM was trained with 10 images of each classification as shown in figures 5.1–5.2.

5.3 Results

5.3.1 Size Distributions

Figure 5.3 shows the total distribution for particle ECDs over all the samples, from 0.25 million to 5 million cycles. It can be seen that the size of the particles follow a log-normal distribution (H_0 = log-normal distribution, p-value = 0.463), the mode of particles has an ECD of $0.88\,\mu m$. The log normal distribution has parameters $\mu = 501.400 \times 10^{-3}$, $95\,\%$ CI=[410.600×10^{-3}, 592.200×10^{-3}] and σ =1.011, $95\,\%$ CI=[950.900×10^{-3},1.077] Therefore the most common size for UHMWPE particles from a spinal implant simulation are within the 0.1-$1\,\mu m$ range, which has been found to be most problematic in biological systems (Cunningham et al., 2013; Green, Fisher, Bridget Matthews, et al., 2000)—a total of $33\,\%$ of the debris were sub-micron. The largest particle found was $46.34\,\mu m$ in diameter, the minimum found was $0.15\,\mu m$.

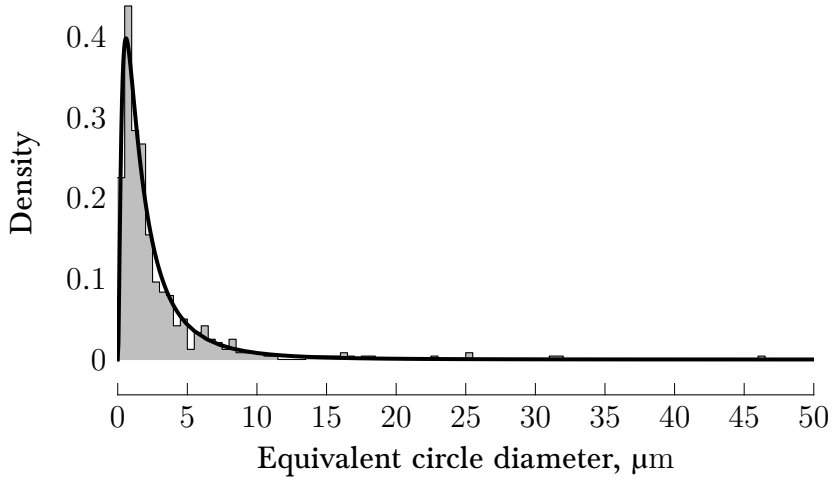

FIGURE 5.3 – Size distribution of all samples combined. Mode = $0.88\,\mu m$, mean ± SEM = $2.89 \pm 0.20\,\mu m$.

Figures 5.4–5.5 shows the individual distributions of debris particle size at the various cycle counts. It can be seen that there is a change in mean particle size as the number of cycles transitioned between 2 and 3 million cycles, shown in figure 5.6. The total amount of particles that were $\geq 0.100\,\mu\mathrm{m}$ in diameter, released after all 5 million cycles was 29.139×10^{12}, $95\,\%$ CI[7.314×10^{12}, 102.970×10^{12}]. The number of particles released is shown to exponentially increase per million cycles, shown in figure 5.7.

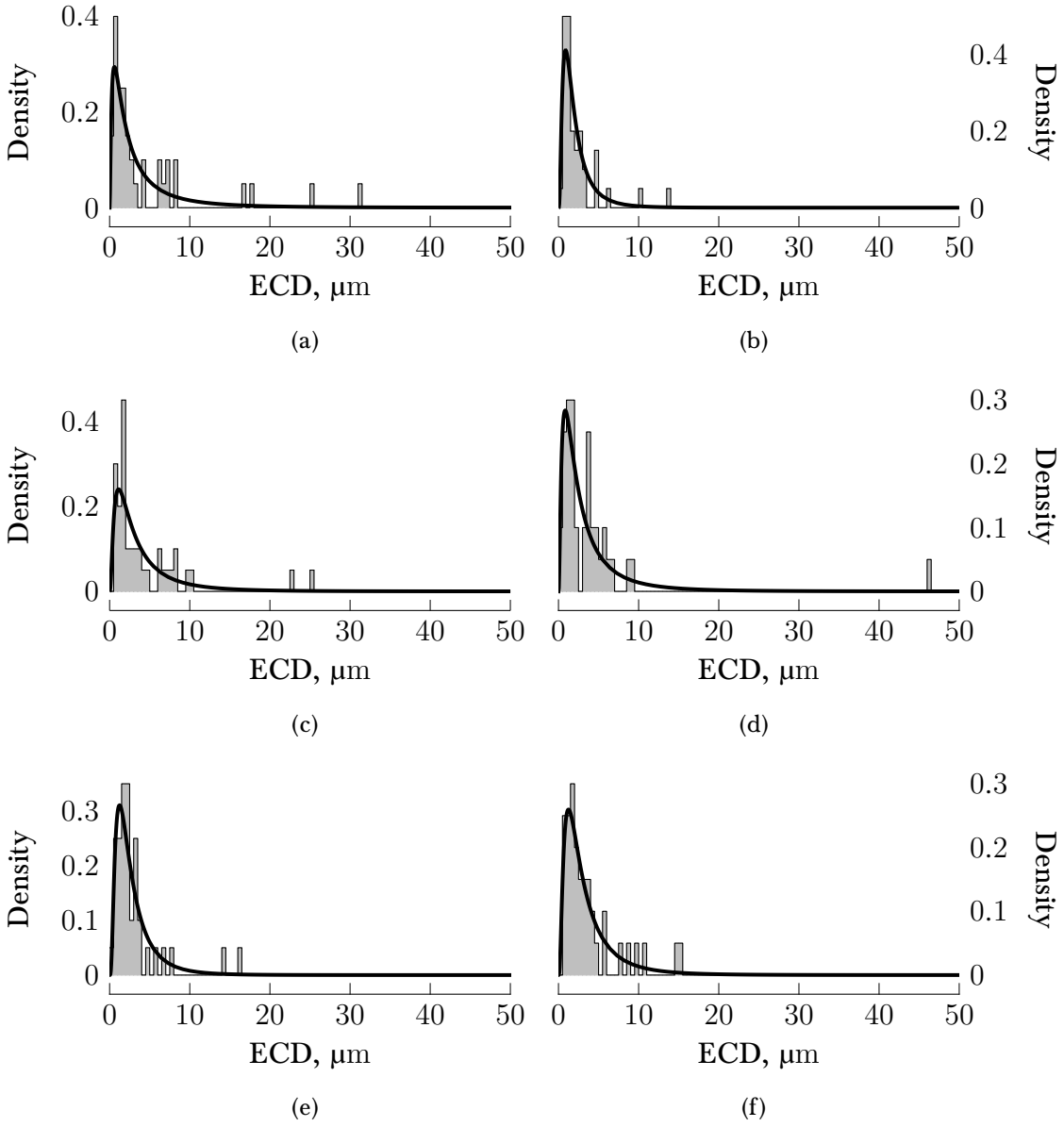

FIGURE 5.4 – Size distributions of (a) 0.25 million cycles (b) 0.75 million cycles (c) 1 million cycles (d) 1.25 million cycles (e) 1.5 million cycles (f) 1.75 million cycles.

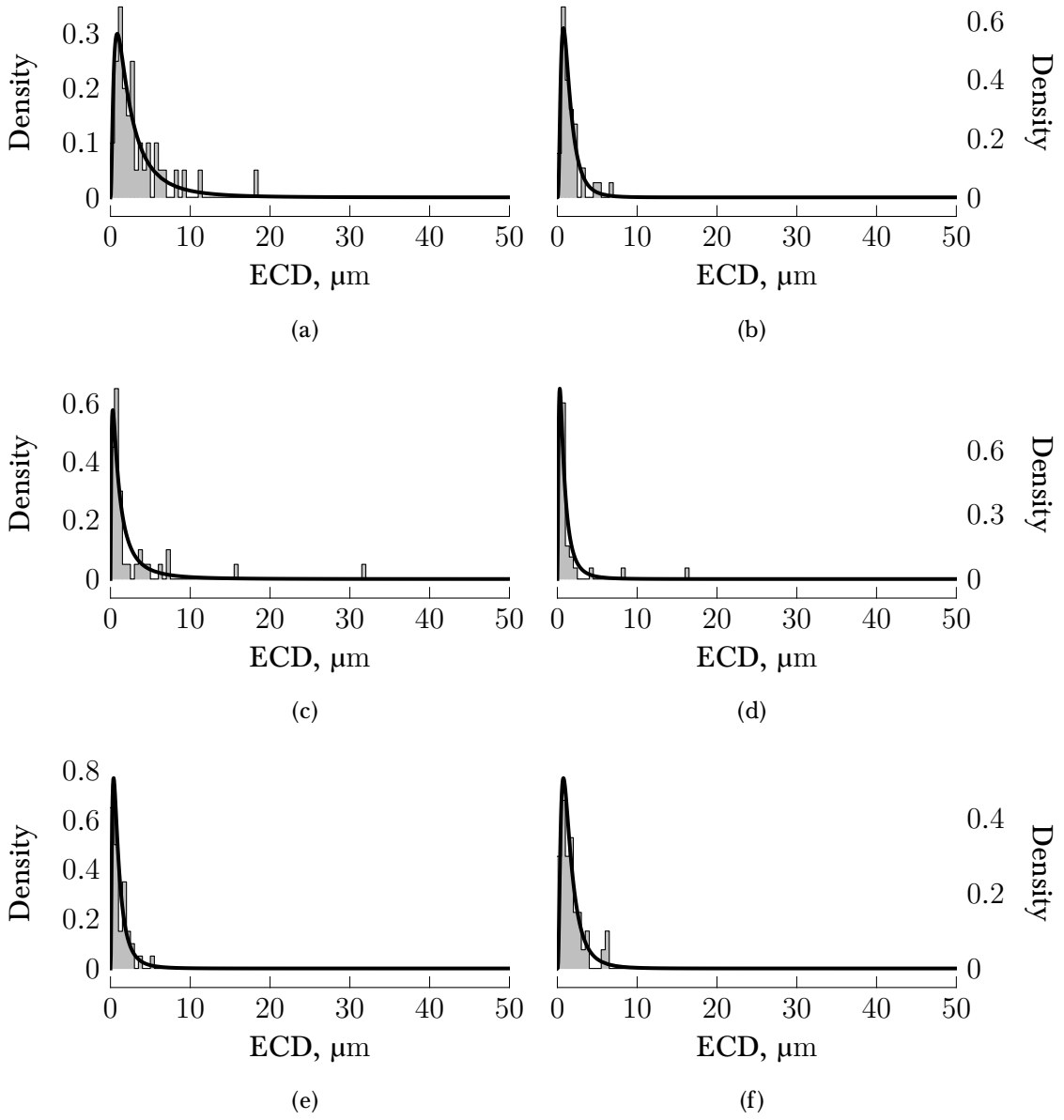

FIGURE 5.5 – Size distributions of (a) 2 million cycles (b) 2.25 million cycles (c) 2.5 million cycles (d) 3 million cycles (e) 4 million cycles (f) 5 million cycles.

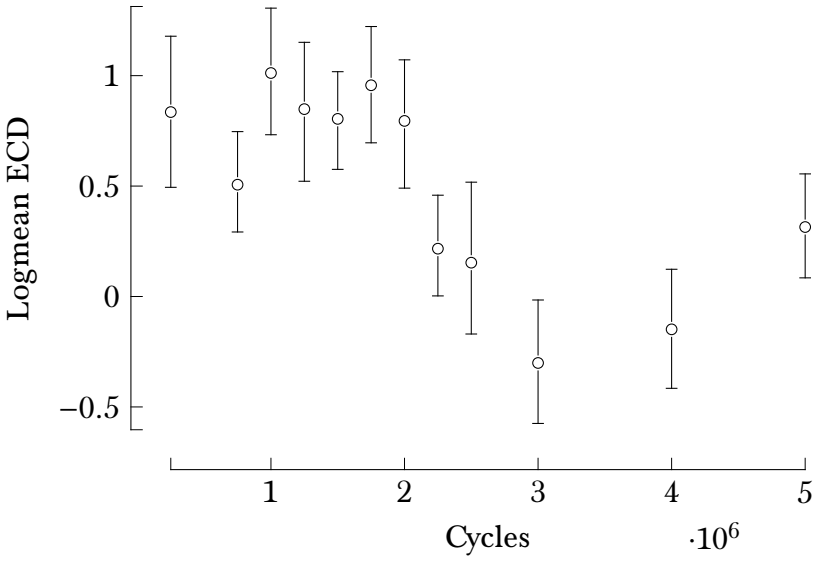

FIGURE 5.6 – Logmean μ of individual particle distributions showing a change in size between 2 and 3 million cycles. Error bars reprisent 95 % confidence intervals for the mean.

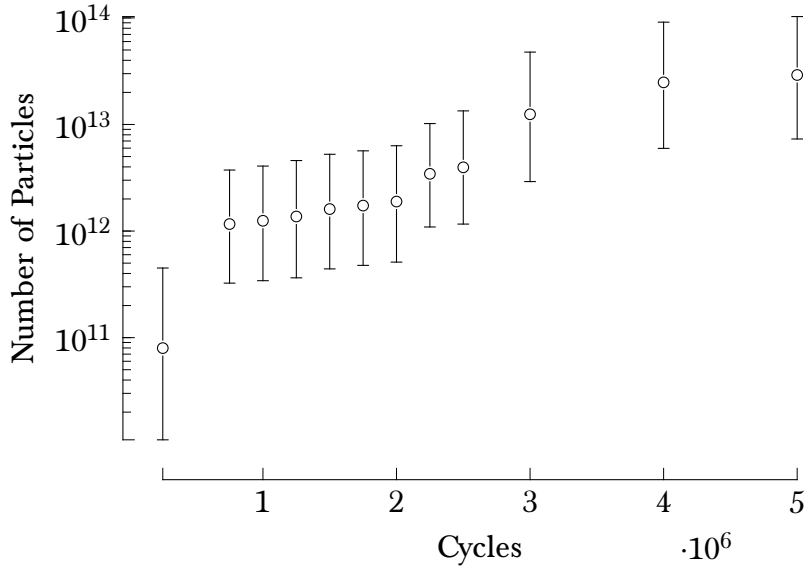

FIGURE 5.7 – Cumulative sum of the number of particles $>100 \times 10^{-3}$ µm, showing an exponential trend. Error bars are 95 % confidence intervals about the mean.

5.3.2 Aspect Ratio

The distribution of the aspect ratio for all particles is shown in figure 5.8, and the individual distributions are shown in figures 5.9–5.10. The majority of the collected debris has an aspect ratio that falls between 1 and 3 (83 %), and follows a log-normal distribution (H_0 = log-normal distribution, p-value = 0.118).

The relationship between particle size and aspect ratio is shown in the density map given in figure 5.11. A delta shaped trend can

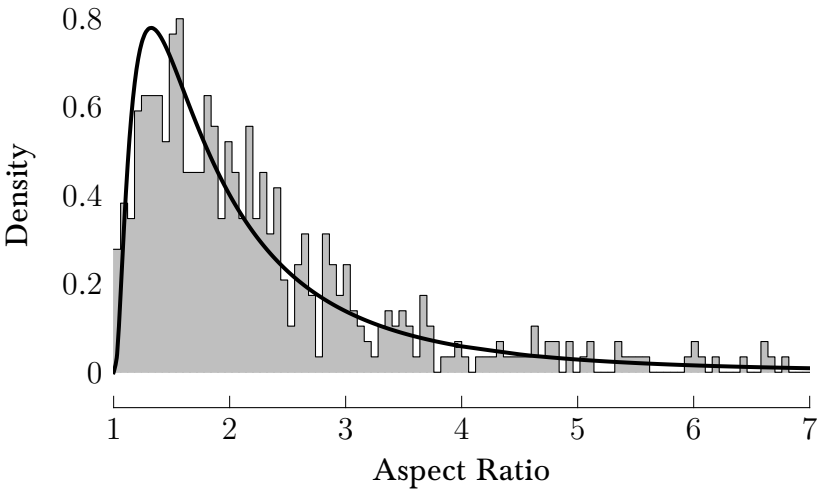

FIGURE 5.8 – Distribution for aspect ratio's of all samples. Mode = 1.550, mean ± SEM = 2.25 ± 0.05.

be clearly observed, with small and large particles having fewer instances of large aspect ratios. Particles between $1\,\mu m$ and $10\,\mu m$ in diameter show the greatest range in aspect ratio. This is a behaviour that has been observed previously in knee implants despite the differences in the kinematics the implant is subject to (Gladkis et al., 2011; Sprecher et al., 2004).

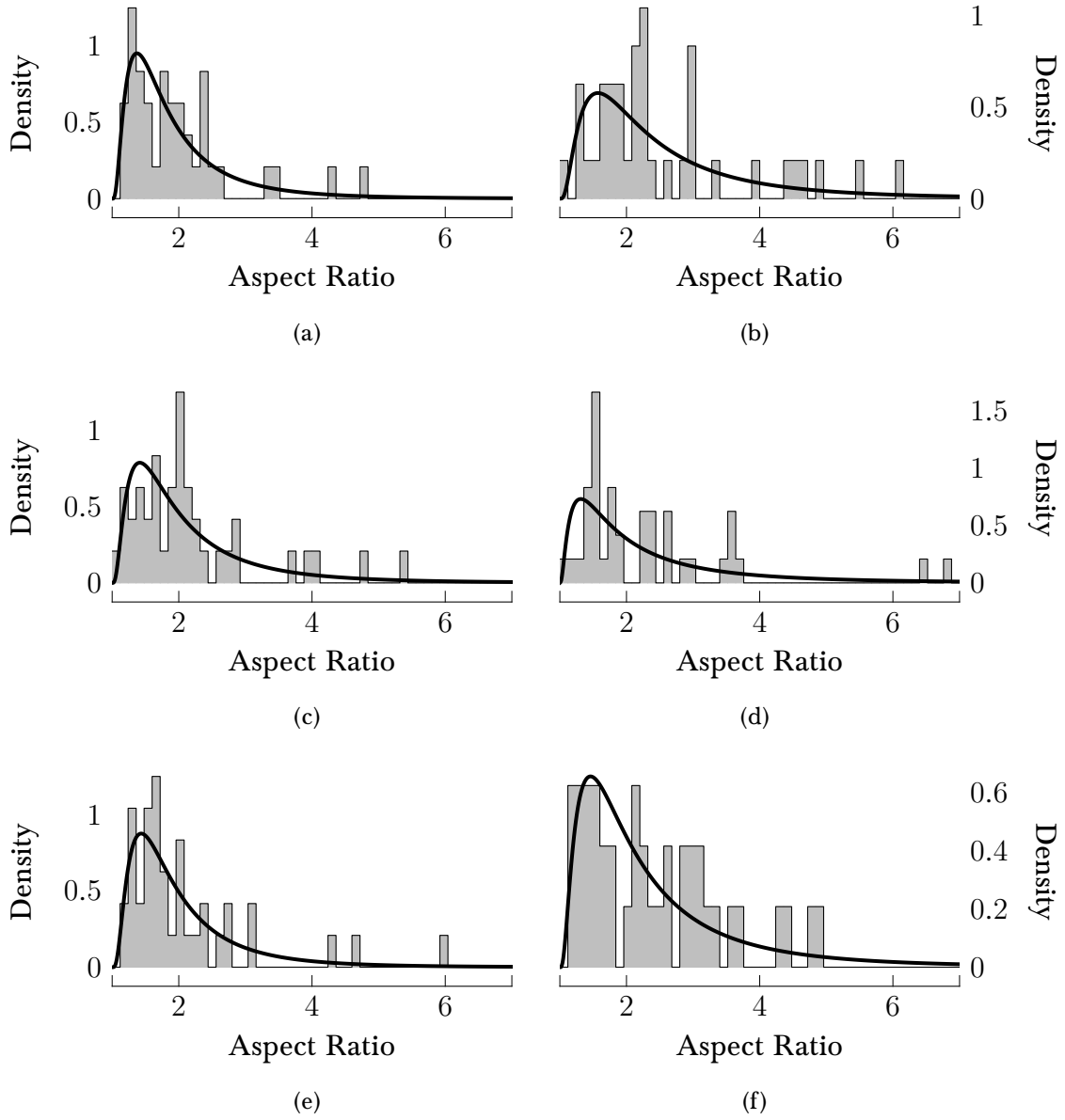

FIGURE 5.9 – Aspect ratio distributions of wear debris (a) 0.25 million cycles (b) 0.75 million cycles (c) 1 million cycles (d) 1.25 million cycles (e) 1.5 million cycles (f) 1.75 million cycles.

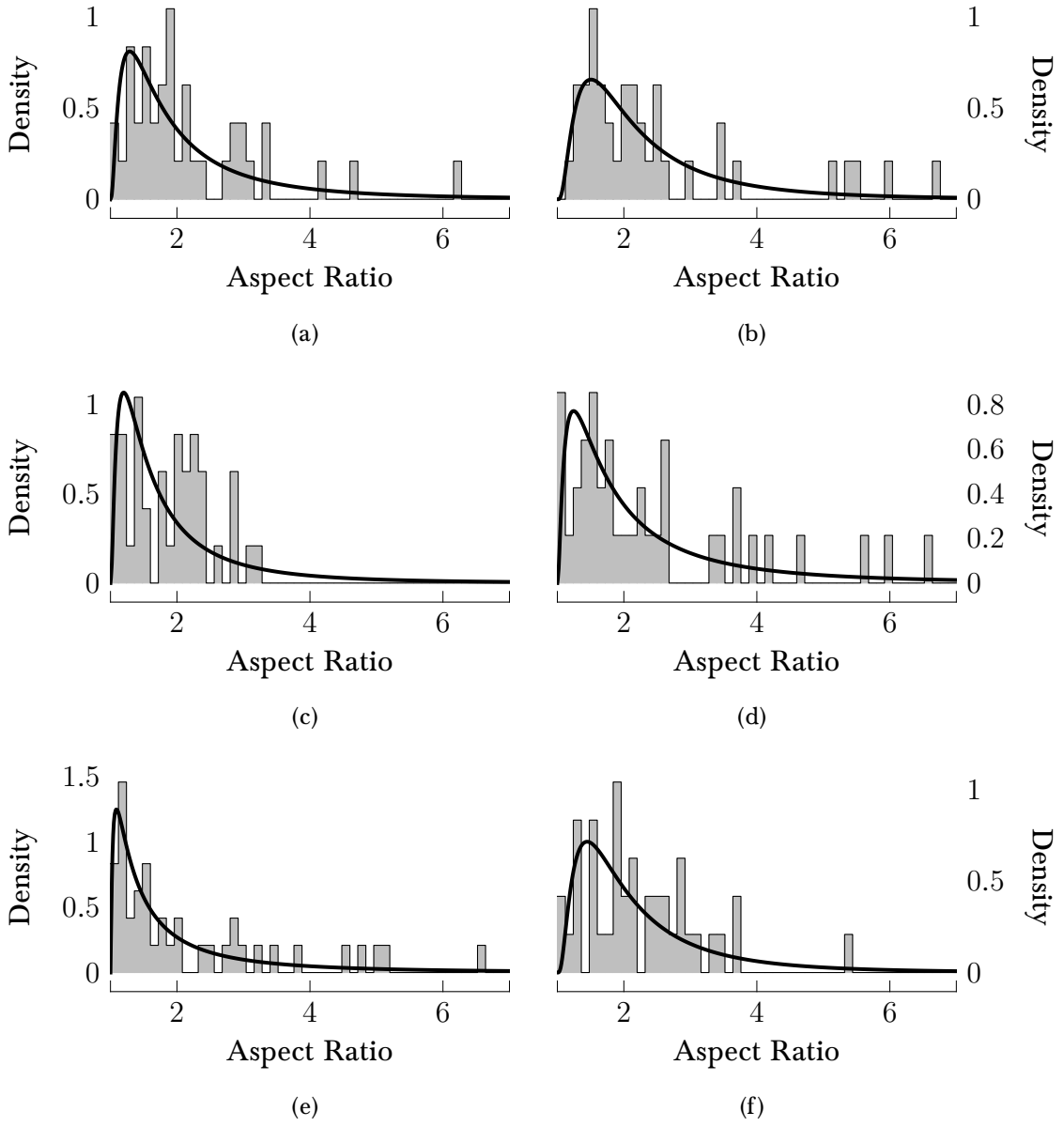

FIGURE 5.10 – Aspect ratio distributions of wear debris (a) 2 million cycles (b) 2.25 million cycles (c) 2.5 million cycles (d) 3 million cycles (e) 4 million cycles (f) 5 million cycles.

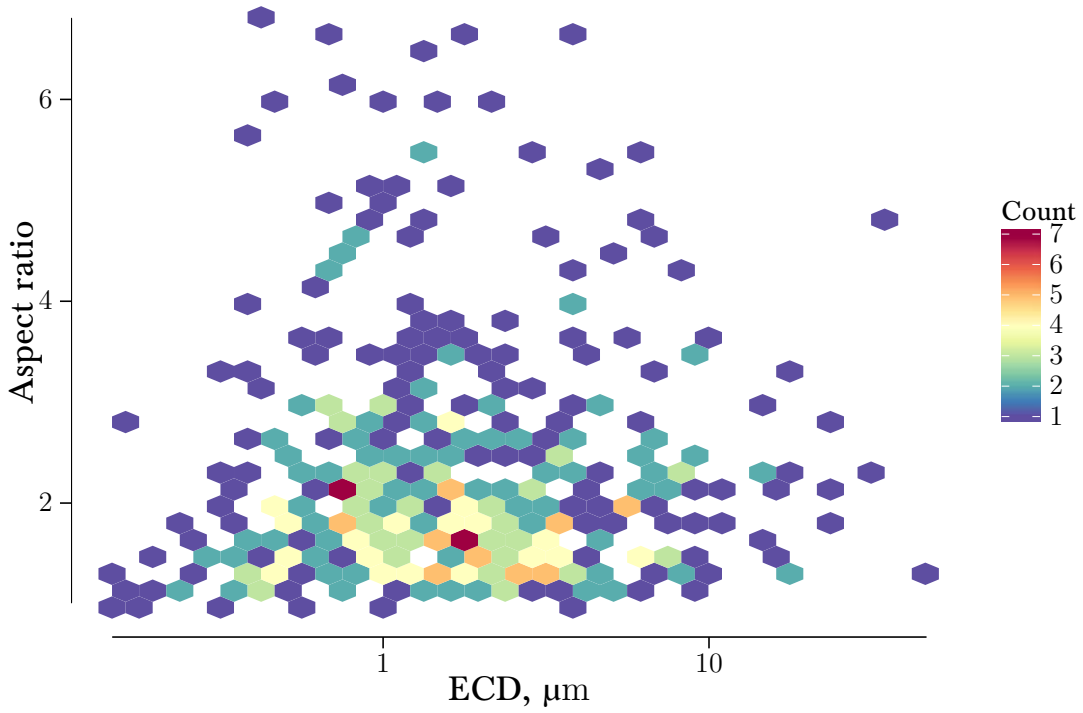

FIGURE 5.11 – Density map of 500 data-points showing the relationship between aspect ratio and ECD.

5.3.3 Debris Morphology

The debris particles taken from TDR simulation tests comprised a wide variety of morphologies. These will have been shaped by both the complicated kinematics of the implant device and the material properties of the frictional surfaces. Table 5.1 summarises the observed debris extracted from the lubricant from each interval of the endurance test.

TABLE 5.1 – The observed debris, extracted from the lubricants at the defined stage of the endurance tests. Also listed are the debris morphologies that were found to be most dominant.

Cycles	Debris Present	Dominant Debris
1M	Fibril, Adhesion, Abrasion, Flake	Fibril & Abrasion
2M	Fibril, Adhesion, Abrasion, Flake	Fibril & Adhesion
3M	Fibril, Adhesion, Sphere, Abrasion	Fibril & Sphere
4M	Fibril, Sphere, Flake, Abrasion	Sphere & Fibril
5M	Fibril, Sphere, Abrasion	Fibril & Abrasion

5.4 Discussion

This study has examined the attributes of UHMWPE debris created in a spinal implant simulation, and the distributions of such debris geometry. From the size distributions shown in Table 2.1, the UHMWPE debris from the spinal simulator was somewhat in agreement with that of other TJRs (Gladkis et al., 2011; Koseki et al., 2005; Lapcikova et al., 2008; Richards et al., 2008; Tipper et al., 1997; Visentin et al., 2004; Wang, Ge, et al., 2010; Zolotarevová, Entlicher, et al., 2010). However it is difficult to make direct comparisons as test, sample preparation and assessment methodologies and equipment vary between research groups (Nine et al., 2014). Additionally, it has been found that *in vitro* and explant studies produce greatly different morphologies or size distributions (ibid.). However, the morphology of wear scars of explanted Charité cores (Kurtz, Ooij, et al., 2007) match the debris found in this study. The measured aspect ratios are also similar to other reported values (Gladkis et al., 2011; Kobayashi et al., 1997; Nine et al., 2014; Topolovec, Cör, et al.,

2014). Additionally a study on the size, aspect ratio and roundness of debris from periprosthetic tissue of SB Charité III TDRs found very similar ECD and aspect ratio distributions (Punt, Baxter, et al., 2011; Veruva et al., 2014). This validates the kinematics of *in vitro* simulations of TDRs using a Bose ElectroForce SD-F/W system—in part validating other studies using the same procedure, such as those conducted by Moghadas et al. (2013b) and Moghadas, Mahomed, Shepherd, et al. (2015) or Xin et al. (2013), and the observational algorithms used to generate this data.

This study suffers from the same limitations found in other studies that use an SEM to characterise debris. These limitations include the large time requirement needed to image and analyse a large quantity of debris. The current study's use of a SIFT and SVM algorithms have taken steps to reduce this time. Some debris, particularly those of high aspect ratio, being prone to clumping together, despite efforts to ensure debris was dispersed. An additional issue with high aspect ratio particles is they can bend and curve back on themselves, resulting in a lower reported aspect ratio. By using an acidic digestion technique, and using $100 \times 10^{-3}\,\mu\mathrm{m}$ filters, both the metallic debris, and those smaller than $100\,\mathrm{nm}$ are lost. This is due to the chemical reactivity of metallic debris, causing them to react with the acid and dissolve. While it is possible that some small wear debris ($<0.1\,\mu\mathrm{m}$) would be present on the filter surface, these would have been removed by the MATLAB script to remove the filter holes as features prior to analysis by machine learning. It is difficult to compare studies of debris, as different characterisation methodologies can have large influences on the results.

However, the most common debris present in total in all 5 million

cycles was fibril debris (figure 5.2(c)–5.2(d)). This form of debris is sometimes associated with ploughing wear that has been gouged from the UHMWPE surface (Stachowiak and Podsiadlo, 2006; Stachowiak, Stachowiak, et al., 2008). This ploughing is associated with abrasive wear. It can also be attributed to the entrainment and 'rolling' of other debris as particles pass through the contact zone, leading to deformation and the formation of long 'string-like' fibrils. Other debris appears to vary in frequency and is dependent on the number of cycles that have passed. During the initial cycles, adhesion (figure 5.1(a) - 5.1(b)) and abrasion (figure 5.1(c) - 5.1(d)) debris are abundant. As the wear test continued their numbers decreased. This is consistent with a running-in period and importantly matches the wear damage found on explanted Charité cores (Kurtz, Ooij, et al., 2007). Wear debris of elongated shape have been shown to have the greatest inflammatory response and macrophage activation (Yang et al., 2002), suggesting the high rates of fibril debris could trigger osteolysis.

The use of the HFRR to generate training images did not incorporate the effects of cross-shear. Whilst this has been shown to have a significant effect on the amount of wear produced, it has been shown that morphology of the wear track possessed similar features that were associated with adhesion/abrasion for both reciprocating and double elliptical sliding (Ge et al., 2008). *Ipso facto* as the wear tracks are similar so to must be the debris. They found evidence that fatigue was the differentiating factor between the tracks. The HFRR generated debris was judged to display enough of the characteristic properties of these classes of wear debris (adhesion and abrasion) to allow for the correct classification.

After 2 million cycles had elapsed, small spheres below $1\,\mu m$ in diameter began to form (figure 5.2(a)–5.2(b)); with their frequency increasing as more cycles elapsed. Spherical particles can be associated with the exfoliation of the contact surfaces as a result of fatigue (Middleton et al., 1974; Scott and Mills, 1973). The increase in occurrence of spherical particles of small diameter coincided with the general decrease in average ECD. It is these sub-micron spheres that are most likely to cause an inflammatory response (Green, Fisher, Bridget Matthews, et al., 2000; Ingham and Fisher, 2000). Examination of periprosthetic tissue samples from revision surgeries of lumbar TDRs show evidence of macrophage activation in wear debris containing tissue samples, indicative of inflammation (Punt, Cleutjens, et al., 2009; Veruva et al., 2014). It was found that although the mean particle size decreased as the wear test progressed, the UHMWPE cores that generated the wear debris had a constant mass loss of $12.0 \pm 1.4\,mg$/million cycles (Moghadas, Mahomed, Shepherd, et al., 2015; Moghadas, 2012). Since the volume of material lost remained constant, the number of wear particles released increased exponentially, as the individual size of the wear debris decreased.

5.5 Chapter Summary

This chapter has investigated the nature of debris produced from an *in vitro* simulation of a TDR implant, using SEM micrographs analysed with computer vision techniques. Being able to measure and then correlate debris generated during *in vitro* simulation is a vital step to understand and eventually mitigating against tribological failure of implanted devices. The general conclusions from this

chapter are:

- Using an integrated debris morphology assessment tool that combined the Scale Invariant Feature Transform (SIFT) to extract key point data from individual images and a Support Vector Decision Machine (SVM) to filter images, increased the efficiency in assessing the debris images.
- The majority occurrence of debris was fibril in morphology. This implied that a combination of micro-machining wear and/or entrainment of debris between the bearing surfaces occurred.
- Debris showed a decreasing trend in size as the wear test progressed, and was mainly fibril/spherical in morphology.
- Abrasion and adhesion predominately occurred before 2 million cycles, between 2–5 million cycles, small spherical particles (associated with fatigue and entrainment) became more prevalent.
- Debris morphology matches that found in reclamation studies.
- Measured UHMWPE debris is predominantly of a size that is known to cause inflammation and possibly osteolysis. The modal equivalent circle diameter of the debris was $880 \times 10^{-3}\,\mu\mathrm{m}$ and the mean ± SEM was $2.98 \pm 0.20\,\mu\mathrm{m}$.

Chapter 6

Sintered PEKK: A Possible Bearing Material for Spinal Arthroplasty?

Chapter Overview

In this chapter, the suitability of Sintered Polyetherketoneketone (PEKK) as an alternative to UHMWPE is explored. An introduction and rational for this material and manufacturing choice is given in §6.1, the methods used which are unique to this chapter are given in §6.2. The results can be found in §6.3 and these are discussed in §6.4. A conclusion to this chapter can be found in §6.5.

6.1 Introduction

Sintered Polyetherketoneketone (PEKK) is a relative newcomer to tribology and biomedical engineering, it is part of the 3D printing revolution. By using selective laser sintering (SLS), a rapid prototyping technology, individual devices can be tailored specifically for the patient. In addition to the ability to create bespoke implants from computed tomography (CT) scans of patients, rather than mass producing standard sizes and requiring the surgeon to compromise between the ideal size and of the sizes available. It is thought that the surface morphology created through the sintering process may have interesting and possibly wear debris reducing properties; these are explored within this chapter.

6.1.1 Theory

PEKK

Chemically, PEKK is as a close relative of Polyetheretherketone (PEEK), the key difference being PEKK has two ketone groups (figure 6.1(a)) for every ether (figure 6.1(b)), while for PEEK the opposite is true. The full chemical formula for PEKK is shown in figure 6.2.

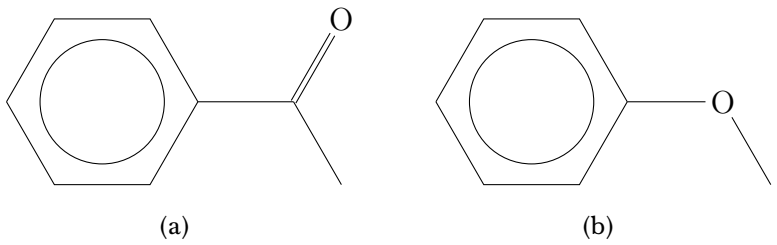

FIGURE 6.1 – A ketone (a) and an ether (b) molecule.

Due to this chemical similarity it was thought that the tribological properties of PEKK may also be similar. There is similarity

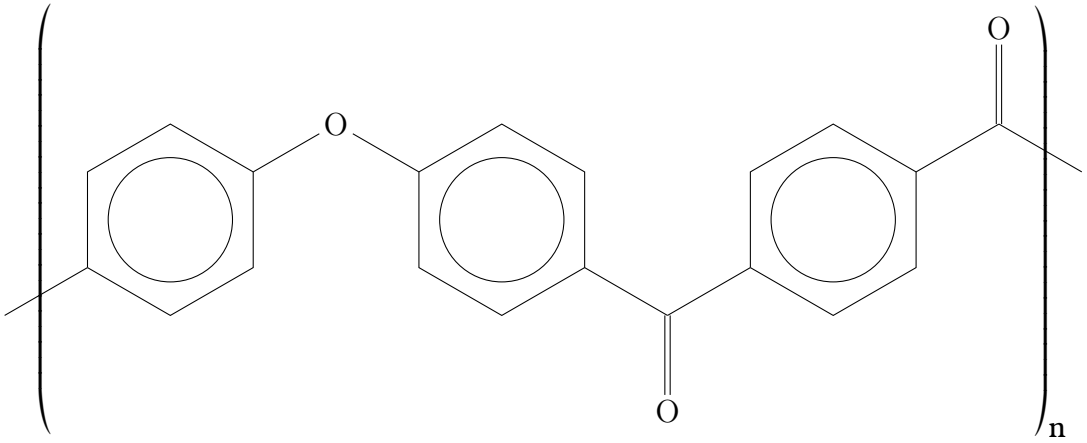

FIGURE 6.2 – Molecular structure of PEKK.

in mechanical properties of PEEK and PEKK, they share similar values in density, tensile strength and modulus. However, PEKK is found to have a lower coefficient of friction, but the Rockwell M hardness varies by grade (80–103) (*MatWeb, Your Source for Materials Information* 2016). The hardness of the exact grade of PEKK used in this study is unpublished. The wear and tribology of PEEK is well studied and has shown low wear rates (Lu and Friedrich, 1995; Stolarski, 1992). The excellent mechanical properties and bio-activity have led to various applications of PEEK and its relatives in biomedical engineering (Jagur-Grodzinski, 1999; Katti, 2004; Kurtz and Devine, 2007). Spinal implants made of PEEK have been successful both as spinal fusion cages (Toth et al., 2006) and also in cervical disc replacements (Kraft et al., 2012; Nabhan et al., 2007; Xin et al., 2013). The wear resistance of PEKK is not well explored, with few papers examining it—but so far it has promising results (Kewekordes et al., 2014).

Sintered surfaces

The use of SLS in biomedical implants is not new. Sintered polymers have been used for scaffold production for many years (Tan et al.,

2004) and SLS PEEK in particular has been shown to be an excellent material for biomedical implants (Schmidt et al., 2007). The use of SLS permits a variable porosity in the material, from $15\,\%$ to virtually $0\,\%$ (ibid.), which would allow for the impregnation of lubricants should it be desired. The material's properties are anisotropic, the tensile strength is lower in the z-axis (i.e. in the direction the layers of material are applied) to the x, y-axis (Hoskins, 2015; Schmidt et al., 2007).

Sintered PEKK manufactured by Oxford Performance Materials has FDA approval for use in bone replacement surgeries[1] and other implants, such as cervical disc fusions are being actively explored (Jordan DeFelice, Oxford Performance Materials, Private Communication, 05/06/2013).

The use of dimpled surfaces has been known to improve tribological and wear performance, by acting either as micro-hydrodynamic bearings or reservoirs of lubricant in areas with poor film coverage (Erdemir, 2005; Etsion, 2004; Roy et al., 2015). The abrasive wear and friction has been shown to be reduced in dimpled hip and knee implants (Chyr et al., 2014; Ito et al., 2000; Qiu et al., 2014). While the fiction and wear performance of sintered parts has not been extensively researched, there are studies that have shown sintered surfaces have good wear resistant properties (Kumar and Kruth, 2008; Takacs et al., 2004; Tsouknidas, 2011).

Wear debris cause issues either when they are trapped between bearing surfaces where they act as a third body greatly increasing abrasive wear; or when they are expelled into surrounding tissue,

[1] *Oxford Performance Materials Receives FDA Clearance for 3D Printed OsteoFab® Patient-Specific Facial Device* 2015.

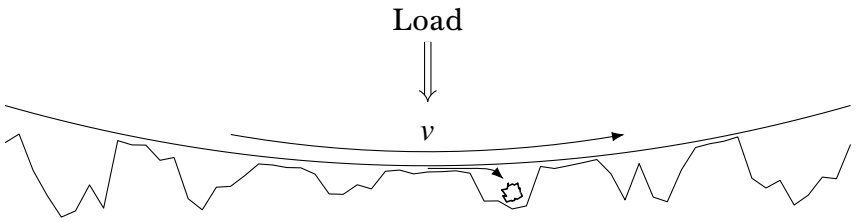

FIGURE 6.3 – Cross-section of a rough surface contact. Showing a wear particle becoming trapped in a void.

where they can cause biological reactions as discussed in chapter 2. Therefore, there are two possible solutions, either reduce/prevent the generation of wear debris through material choice—something that has eluded engineers for decades, or to trap debris somewhere they cannot cause harm. If a surface has many voids or dimples, it is possible that wear debris will fall into them, and subsequently become trapped. This idea is illustrated in figure 6.3.

6.2 Method

6.2.1 Geometric Analysis

The geometric tolerance of the printed PEKK specimens was assessed by comparing the measured geometry with that of the theoretical measurements based on drawings sent to the manufacturer. Five samples of the high-frequency reciprocating rig (HFRR) stubs were measured in diameter and thickness 5 times in different positions using vernier callipers (Fischer Scientific, UK). To measure the spinal disc socket, 3 specimens were scanned on the Alicona Infinite Focus, as described in §3.6. However the disc was bolted to a 3D printed jig to ensure consistent alignment between scans. The jig was designed by N. C. Green (University of Birmingham) and 3D printed by S. Rowan (University of Birmingham). An engineering drawing is shown in appendix B. The $10\times$ magnification lens was used with three steps of decimation—this was required to reduce

the number of data points to within the limits of the equipment's memory. Once scanned, the sphericity and radius of the socket was measured in MATLAB using a sphere fitting algorithm written by Jennings (2013). Briefly, this script attempts to minimise equation 6.1.

$$\sum \left((x - xc)^2 + (y - yc)^2 + (z - zc)^2 - r^2 \right)^2 \tag{6.1}$$

where, x, y & z are the coordinate data, xc, yc & zc are coordinates for the sphere centre and r is the radius.

The mean radius of each disc socket was calculated by doing the following:

1. The dataset was translated to be centred about the socket's centre, using a preliminary run of the 'sphereFit' algorithm.

2. Data points beyond an $8\,\mathrm{mm}$ patch about the socket centre in x and y was excluded as they were beyond the lip of the socket.

3. A random sample without replacement, of size 10×10^3, of the coordinate data was taken, the radius was found for this sub-sample by minimising equation 6.1.

4. Step 3 was repeated 50×10^3 times, appending each calculated radius to a vector of radii.

5. The mean and standard deviation for the resultant distribution of radii was calculated.

Figure 6.4 shows the socket part of the original STL file sent to the Oxford Performance Materials, the manufacturers of the PEKK parts, see appendix. The sphereFit algorithm finds a radius for

the cup of 10.341 mm—close to the 10.35 stated in the engineering drawing found in Appendix A of Moghadas (2012, p. 176).

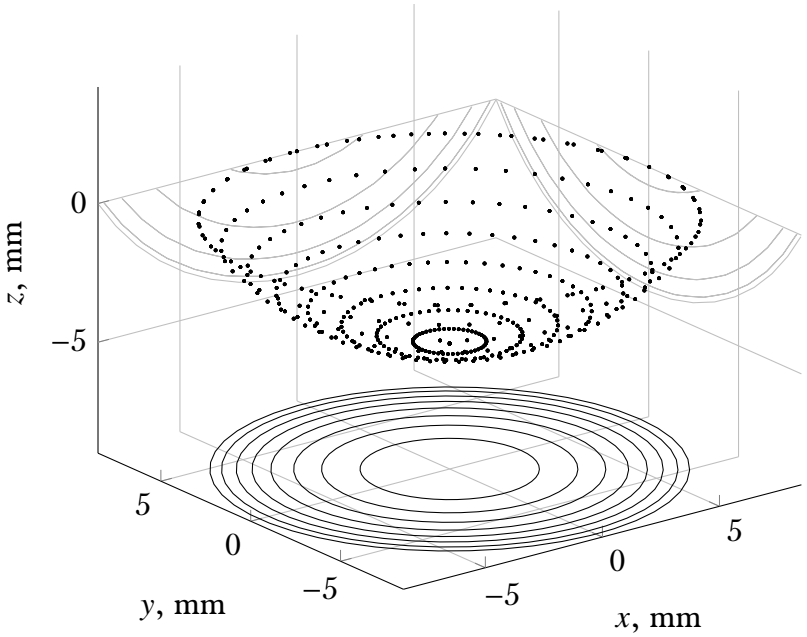

FIGURE 6.4 – Cup section of original STL file sent to manufacturer.

Roughness

The roughness of the socket area of the PEKK implant was measured using the Alicona Infinite Focus's measurement suite software. The socket area first had the sphereical form removed to create a flat plain maintaining the waviness and roughness geometries using the form remove tool. The roughness was then measured using the roughness measuring tool taking a path bisecting the centre of the socket. The path was the full width of the socket area (>10 mm in length), thereby complying with ISO standard 4287 (British Standards Institution, 2009). The lens used for the scan was the 10x magnification, therefore, also complying with table 3.2.

Cross Section

An HFRR specimen was embedded in epoxy resin on the cylindrical edge. Once cured, the specimen was ground until the midpoint of

TABLE 6.1 – Grinder-polisher process.

Surface	Abrasive	Load (N)	Speed (rpm)	Time (min:sec)
CARBIMET abrasive disc	220 to 320 grit SiC	22	240–300	Until plain
Trident cloth	6 µm diamond suspension	27	120–150	6:00
Trident cloth	3 µm diamond suspension	27	120	4:00
MICRO-CLOTH	0.050 µm colloidal silica suspension	27	120–150 (contra)	2:00

the cylinder and polished using a Buehler grinder-polisher (Buehler, ITW Test & Measuement GmbH, Düsseldorf, Germany). The grinding and polishing followed the 4 step process in table 6.1 (*Buehler Reference Documentation* 2001).

The polished surface was then examined on the Alicona Infinite Focus (see §3.6), the 10× lens was used to create a mosaic image of the cross section, topology data was not used as this would cause areas with poor focus or lighting conditions to not be recorded.

6.2.2 Frictional Properties

The frictional properties were measured using two methods: i. using the HFRR (see §3.3) with bovine serum at a concentration of $20\,\mathrm{g\,L^{-1}}$ at $10\,\mathrm{Hz}$ with a normal load of $100\,\mathrm{g}$, and ii. by measuring the frictional torque using the Bose Spinal Disc Fatigue/Wear system (SD-F/W) against a Cobalt Chrome Molybdenum alloy (CoCrMo) ball (see §3.2) to generate Stribeck curves using the method below. The engineering drawing of the ball is shown in B.

Stribeck curves

Stribeck curves are a plot of friction factor against Sommerfeld number. The shape of the curve can be used to infer the lubrication regime, an example is shown in figure 6.5. Each regions of the curve relates to one of the three lubrication regimes (see §2.2.2): i. region 1 is associated with boundary lubrication (figure 2.10(a)), ii. region 2 is associated with the transitioning regime i.e. mixed lubrication (figure 2.10(b)), and iii. hydrodynamic lubrication (figure 2.10(c))—which region 3 is associated with.

The friction and velocity are normalised to friction factor, f̃; and Sommerfeld number, Z, respectively. This allows a comparison between specimens with differing geometries, loads, ranges of motion, etc. to be made. The definitions of friction factor and Sommerfeld number are given in equations 6.2–6.3 (Scholes and Unsworth, 2000):

$$\tilde{f} = \frac{\tau}{R^* W} \tag{6.2}$$

$$Z = \frac{\eta u R^*}{W} \tag{6.3}$$

where,

$$u = \frac{\omega R^*}{2} \tag{6.4}$$

$$\omega = \frac{2\pi\theta}{180} \cdot f \tag{6.5}$$

where τ is the frictional torque, R^* is the combined radius (from equation 3.4), W is the normal load. η is the lubricant viscosity, u is the entraining velocity, f is the frequency and θ is the angular displacement.

To find the frictional torque in flexion and in lateral bend, the spine simulator was moved in a singular axis while under the average

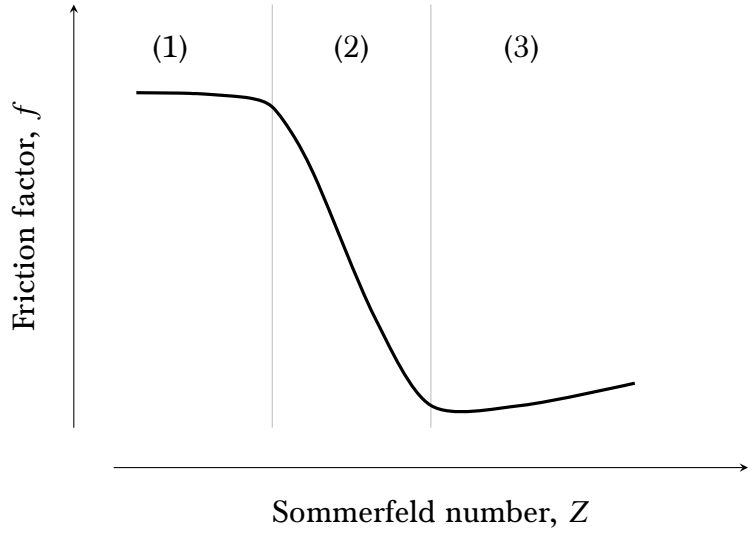

FIGURE 6.5 – The Stribeck curve, showing change in friction factor with Sommerfeld number. The different regions imply differing lubrication mechanisms, with (1) being boundary lubrication, (2) being mixed, and (3) being hydrodynamic.

load (1200 N) specified by the ASTM standard 2423 (American Society for Testing and Materials, 2005). The motion was run for 100 cycles at 8 frequencies: 0.25–2 Hz in steps of 0.25 Hz. The motion of flexion/extension could not be measured over the full range as the load cell was limited to 15 N m. Therefore, the range was limited to ±3°, this was also required for the testing of ultra-high molecular weight polyethylene (UHMWPE) (Moghadas et al., 2013a). Lateral bend frictional torques were measured using the same range specified in British Standards Institution (2011b), ±2°. Each motion was repeated 4 times to get an average before changing to the next axis or frequency. The frictional torque was determined from the mean of the peaks absolute value of the final 10 cycles.

The peaks were found using continuous wavelet transforms (CWTs) (equation 6.6) as the raw signal was noisy (Du et al., 2006; Muzy et al., 1994). The CWT finds peaks that exist on multiple scales—thereby finding the true peaks in a noisy signal. The implementation of the CWT used was the 'wmtsa' package in R (Constantine and Percival, 2013). See figure 6.6 for an example of peaks found on the last 10 cycles of a Stribeck test. The function

(code A.5) written to calculate the final 20 peaks and troughs is shown in appendix A page 145.

$$W(a,b) = \frac{1}{\sqrt{a}} \times \int f(x).\psi \left(\frac{(x-b)}{a} \right) \mathrm{d}x \tag{6.6}$$

where, $W(a,b)$ is the wavelet transform, a is >0 and defines the scale, b is real and defines the shift. $f(x)$ is the time series data and ψ is the *mother wavelet* function.

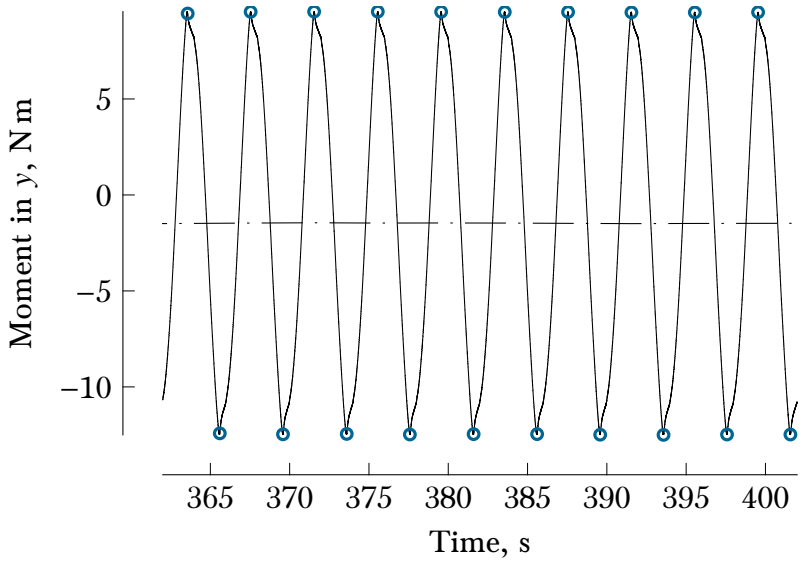

FIGURE 6.6 – The last 10 peaks and troughs found using CWT of moment data from an example friction test.

Stribeck curves were plotted for the lubricant concentration of bovine serum at a protein concentration of $1.2\,\mathrm{g\,l^{-1}}$. The friction coefficient for the high concentration bovine serum was tested and compared with UHMWPE using the HFRR. The viscosity of lubricants where measured on a AR-G2 rheometer (TA Instruments, West Sussex, UK). In the case of the high concentration bovine serum, the measurements were made by Moghadas (2012, p. 75); the low concentration bovine serum was measured by N. C. Green and J. Bowen (University of Birmingham). The viscosities are shown in table 6.2:

The low bovine serum concentration has the same viscosity as ringers solution (ibid., p. 75). The composition of the lubricant

TABLE 6.2 – Viscosities of bovine serum lubricant at different concentrations.

Low concentration ($1.2\,\mathrm{g\,l^{-1}}$)	High concentration ($30\,\mathrm{g\,l^{-1}}$)
$0.71 \pm 0.02\,\mathrm{mPa\,s}$	$1.4 \pm 0.4\,\mathrm{mPa\,s}$

between bearing surfaces in total disc replacements (TDRs) is not known, but is thought to be similar to interstitial fluid, the properties of which are between Ringer's solution and dilute bovine serum (Fogh-Andersen et al., 1995; Sherwood, 2011). Therefore, the low concentration solution of bovine serum can be considered a 'worst case scenario' for lubrication in a TDR.

6.2.3 Wear Test

The wear test was performed according to §3.2, however the concentrations of bovine serum was changed to the low concentration used in §6.2.2. While ideally both concentrations would have been used for the wear testing of of the PEKK implant, due to time constraints only one condition could be run. As shown by Moghadas et al. (2013a), the lubrication regime does not change between ringer solution and bovine serum, only magnitude of frictional torque. Therefore, if the implant is capable of surviving in the low concentration, then the implant would have demonstrated it is capable of functioning at the lower limit of conditions a TDR may possibly meet. In addition to the mass balance measurements, Alicona Infinite Focus scans were taken prior to testing and after 1 million cycles according to §3.6.

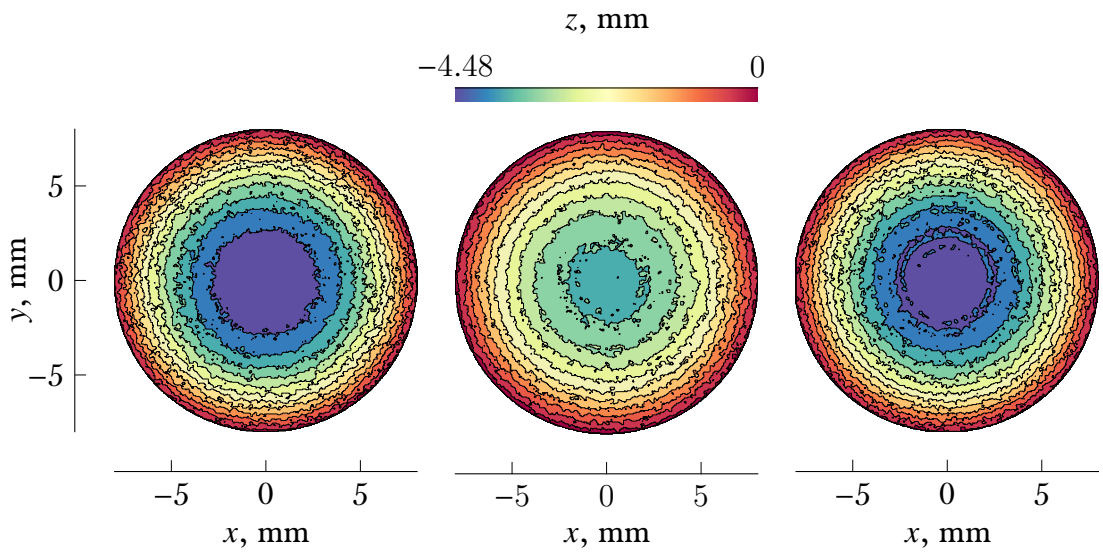

FIGURE 6.7 – Contour plots of the central 8 mm patches of three disc sockets.

6.3 Results

6.3.1 Geometric Analysis

Accuracy

Examining the sintered PEKK sockets samples on the Alicona Infinite Focus and importing the data into MATLAB, the dimensions can be compared with the original STL sent to the manufacturer.

TABLE 6.3 – PEKK socket radii, measured using the Alicona Infinite Focus and MATLAB.

Disc 1, mm	Disc 2, mm	Disc 3, mm	Mean ± SD
11.788 ± 0.009	11.477 ± 0.008	11.432 ± 0.007	11.610 ± 0.178

Table 6.3 shows the radii of the socket in the sintered PEKK discs, found using the sphere fit algorithm written by Jennings (2013), using a 8 mm radius patch of data about the centre of the socket. The contour plots of discs 1–3 are shown in figure 6.7. The radius data shows the cup is 12 % larger than specified. Such a large difference in radius has a pronounced effect on the contact pressure exerted on

TABLE 6.4 – Vernier calliper measurements of HFRR stubs diameter.

	Diameter, mm					
	Specimen 1	Specimen 2	Specimen 3	Specimen 4	Specimen 5	
	10.12	10.15	10.11	10.23	10.08	
	10.16	10.06	10.15	10.20	10.10	
	10.14	10.09	10.11	10.23	10.11	
	10.12	10.06	10.05	10.26	10.06	
	10.26	10.11	10.05	10.19	10.09	
Mean	10.16	10.09	10.09	10.22	10.09	10.13
SD	0.05	0.03	0.04	0.02	0.02	0.06

TABLE 6.5 – Vernier calliper measurements of HFRR stubs nominal thickness.

	Thickness, mm					
	Specimen 1	Specimen 2	Specimen 3	Specimen 4	Specimen 5	
	3.90	3.80	3.81	3.88	3.81	
	3.89	3.80	3.75	3.87	3.80	
	3.89	3.77	3.74	3.86	3.86	
	3.89	3.78	3.79	3.85	3.82	
	3.89	3.77	3.78	3.88	3.82	
Mean	3.89	3.78	3.77	3.87	3.82	3.83
SD	0.00	0.01	0.03	0.01	0.02	0.05

the bearing surfaces. By using equation 3.1 in §3.3.1, a theoretical contact pressure (assuming smooth contact) for the manufactured sockets was 106.77 MPa. Substantially more than that of UHMWPE using the geometry of a Charité core (see §3.3.1).

Tables 6.4 and 6.5 show vernier calliper measurements for 5 HFRR specimens, chosen at random. The original drawing specified 10 mm diameter by 4 mm thickness discs. Therefore, the disc is 1.3 % larger in diameter and 3.5 % thinner than specified.

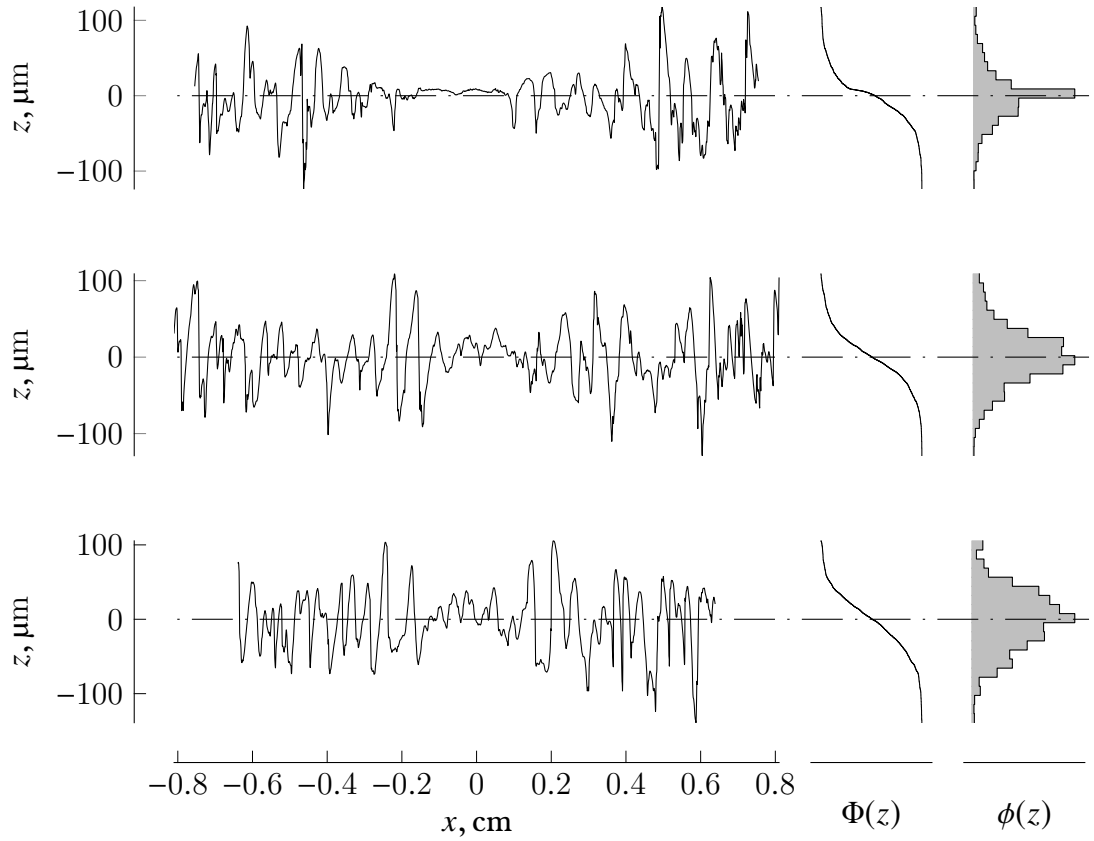

FIGURE 6.8 – Roughness profiles of three PEKK discs, including the 'bearing curve' $\Phi(z)$ and the height distribution $\phi(z)$.

Roughness

The average surface roughness was $28.287 \pm 4.114\,\mu\mathrm{m}$, the profiles that this was calculated from are shown in figure 6.8. Note how the central section $\approx 0.2\,\mathrm{cm}$ in width has a lower peak height compared with the outer sections. This was caused by the 3D printing process having a course vertical resolution leading to a striation effect. This caused the central section of the cup to be flat, with stair stepped geometry leading to the edge of the socket section approximating the geometry of a sphere.

Figure 6.8 also shows both the cumulative height distribution 'bearing area' curves ($\Phi(z)$) and the height distribution ($\phi(z)$). The

mean ± standard deviation (SD) roughness skewness (R_{sk}) and roughness kurtosis (R_{ku}) was -0.011 ± 0.253 and 3.622 ± 0.606 respectively. The roughness has similar parameters to a normal distribution, allowing calculations of contact area to be performed (Greenwood, 1967; Greenwood and Tripp, 1967).

Cross-section

Figure 6.9 shows an Alicona Infinite Focus imaging only scan of the cross section. The scan shows the cross section was slightly bowed from material swelling during printing and some voids. Other than the few voids, the material appears homogeneous and fully sintered, i.e. no stratifications of unsintered PEKK, with only the surfaces showing signs of the manufacturing process.

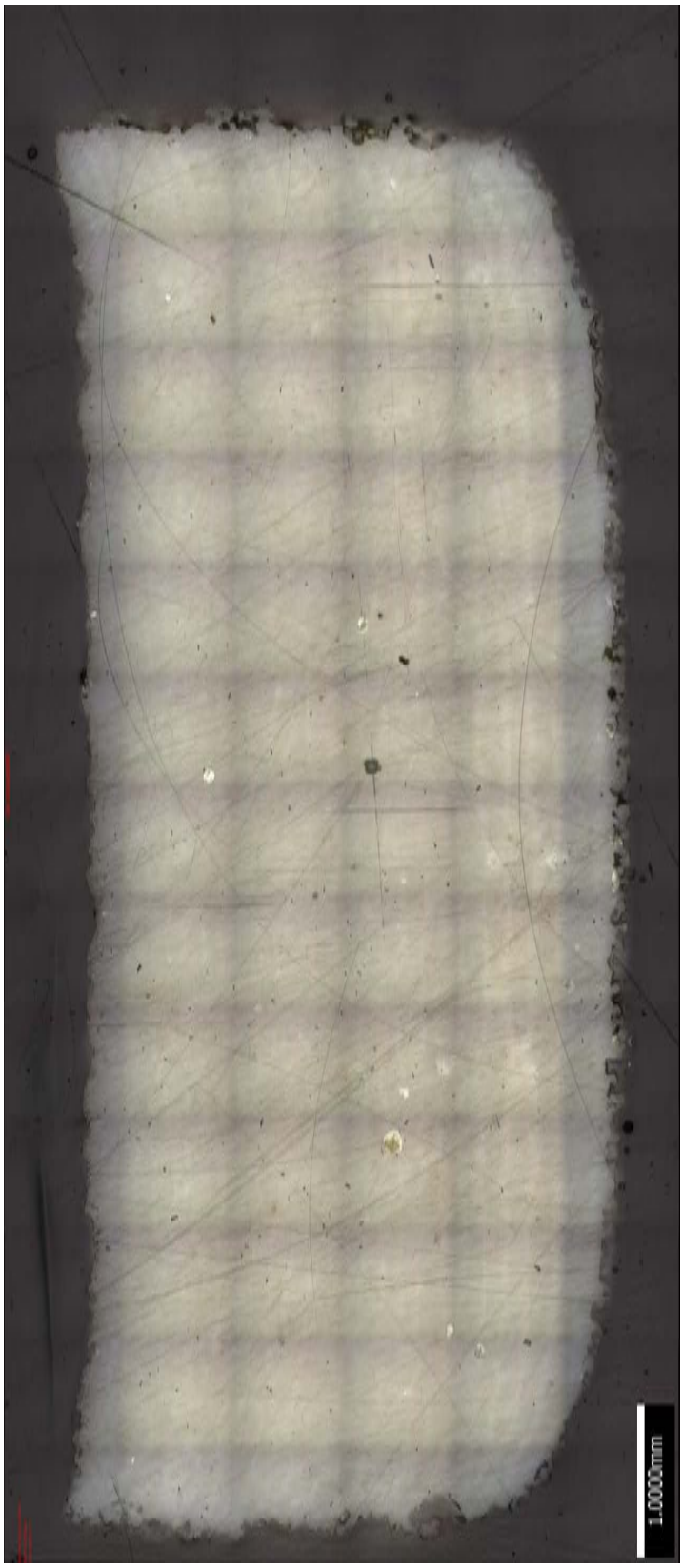

FIGURE 6.9 – The cross-section of an HFRR specimen.

6.3.2 Frictional properties

The friction coefficient for PEKK in bovine serum of concentration $20\,\mathrm{g\,L^{-1}}$ is shown in figure 6.10. The friction coefficient was measured using the HFRR using a normal load of $100\,\mathrm{g}$, a $2\,\mathrm{mm}$ stroke and frequency of $10\,\mathrm{Hz}$. This is compared with UHMWPE under identical conditions.

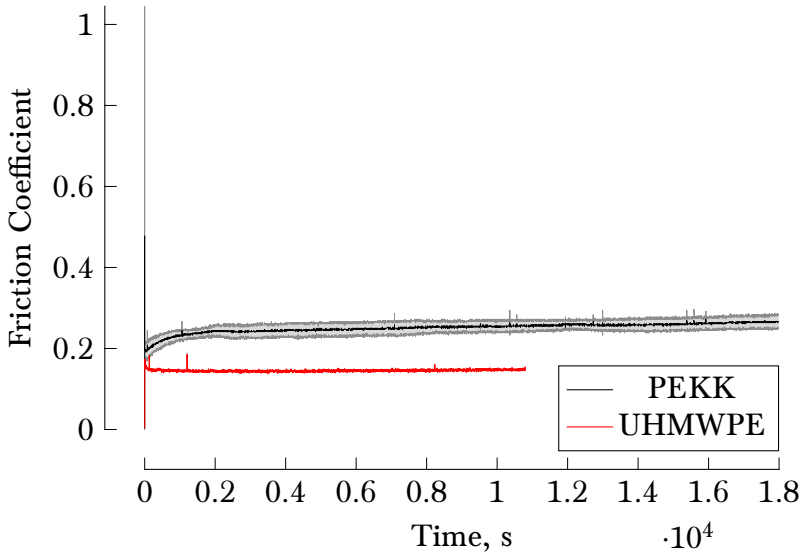

FIGURE 6.10 – Mean friction coefficient of five PEKK disc in bovine serum. The shaded grey area represents SD.

Frictional torques from low concentration of bovine serum are shown in figure 6.11. Unfortunately, due to time constraints and the lead time for SeraLabs to restock bovine serum only a single implant could be tested at the high protein concentration Without repeated measurements it is not possible to know if the results are a statistical fluke or representative. There is a single point on figure 6.11(a) which has a much greater variance than the other points. This could have been due to the implant being incorrectly realigned during repeated measures.

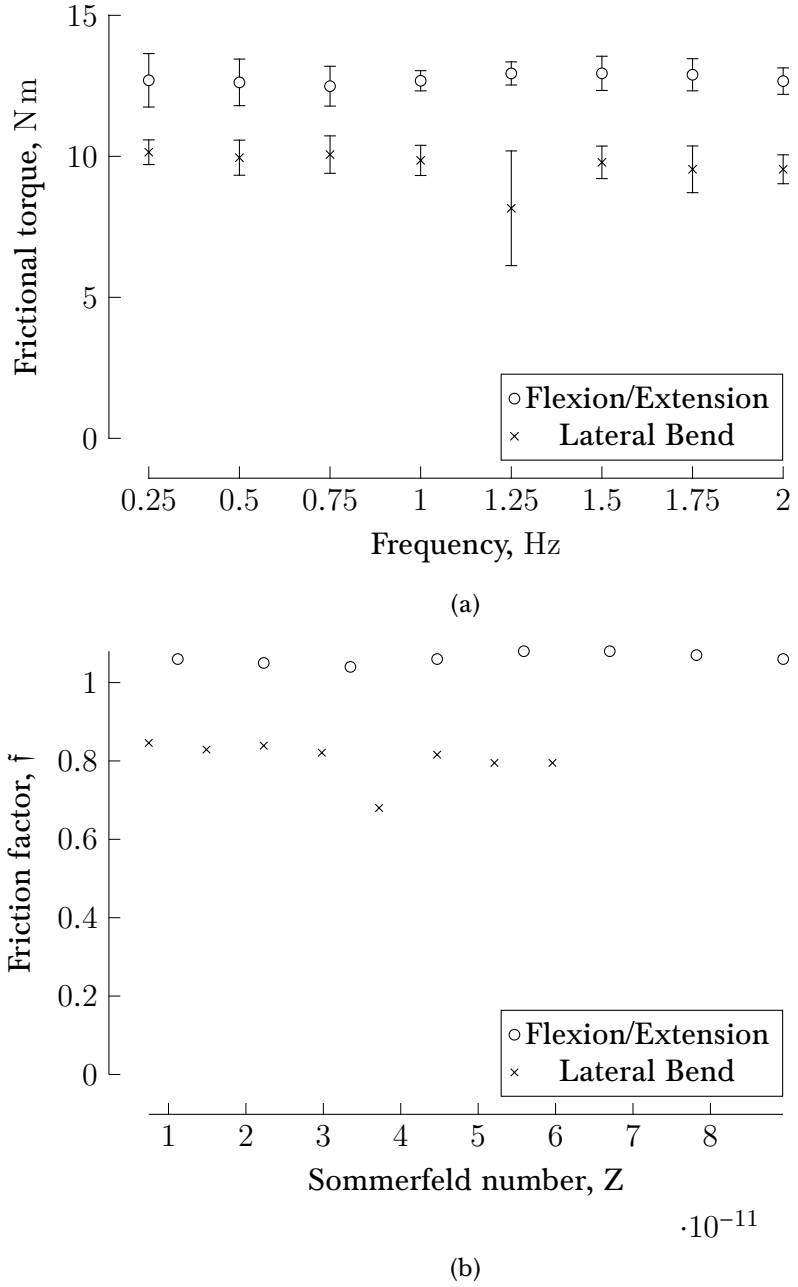

FIGURE 6.11 – The mean ± SD frictional torques for flexion/extension and lateral bend using the low concentration (a), and the Stribeck curves for these torques (b).

6.3.3 Material Loss

The mass losses of each implant as the long term *in vitro* wear test progresses are shown in figure 6.12. After 1 million cycles in the low concentration bovine serum lubricant, the implant had suffered enough loss of mass for the shoulders of the metal ball to impact on the socket rim. For this reason the test was stopped at this point.

TABLE 6.6 – R output for segmented linear regression.

```
        ***Regression Model with Segmented Relationship(s)***

Call:
segmented.lm(obj = fit, seg.Z = ~x, psi = list(x = 0.5))

Estimated Break-Point(s):
    Est.  St.Err
0.61480 0.06091

t value for the gap-variable(s) V:  0

Meaningful coefficients of the linear terms:
     Estimate Std. Error t value Pr(>|t|)
x    0.007160   0.001273   5.625   0.0302 *
U1.x 0.023000   0.004221   5.448       NA
---
Signif. codes:  0 ‘***’ 0.001 ‘**’ 0.01 ‘*’ 0.05 ‘.’ 0.1 ‘ ’ 1

Residual standard error: 0.0007115 on 2 degrees of freedom
Multiple R-Squared: 0.9971,  Adjusted R-squared: 0.9927

Convergence attained in 2 iterations with relative change 3.173161e-18
```

The rate of mass lost was determined by linear regression, for the polymer socket a regression line with an intercept of 0 was fit using the R command: `fit<-lm(colMeans(y)~0+x)`. The coefficient for gradient ± the standard error was 0.3810 ± 0.0155 g/million cycles (R^2: 0.991, p-value: 16.4×10^{-6}). The mass loss for the metal ball was fitted with a segmented linear regression using the ‘segmented’ R package (Muggeo, 2003, 2008). This command requires an initial linear fit, found using the command mentioned above; the relationship formula, seg.Z; and an initial estimate of the breakpoint(s), psi. A variety of initial values for the breakpoints were tested with no significant difference in output. The output of this function is shown in table 6.6.

Figure 6.13 shows an implant after 1 million cycles. Note the

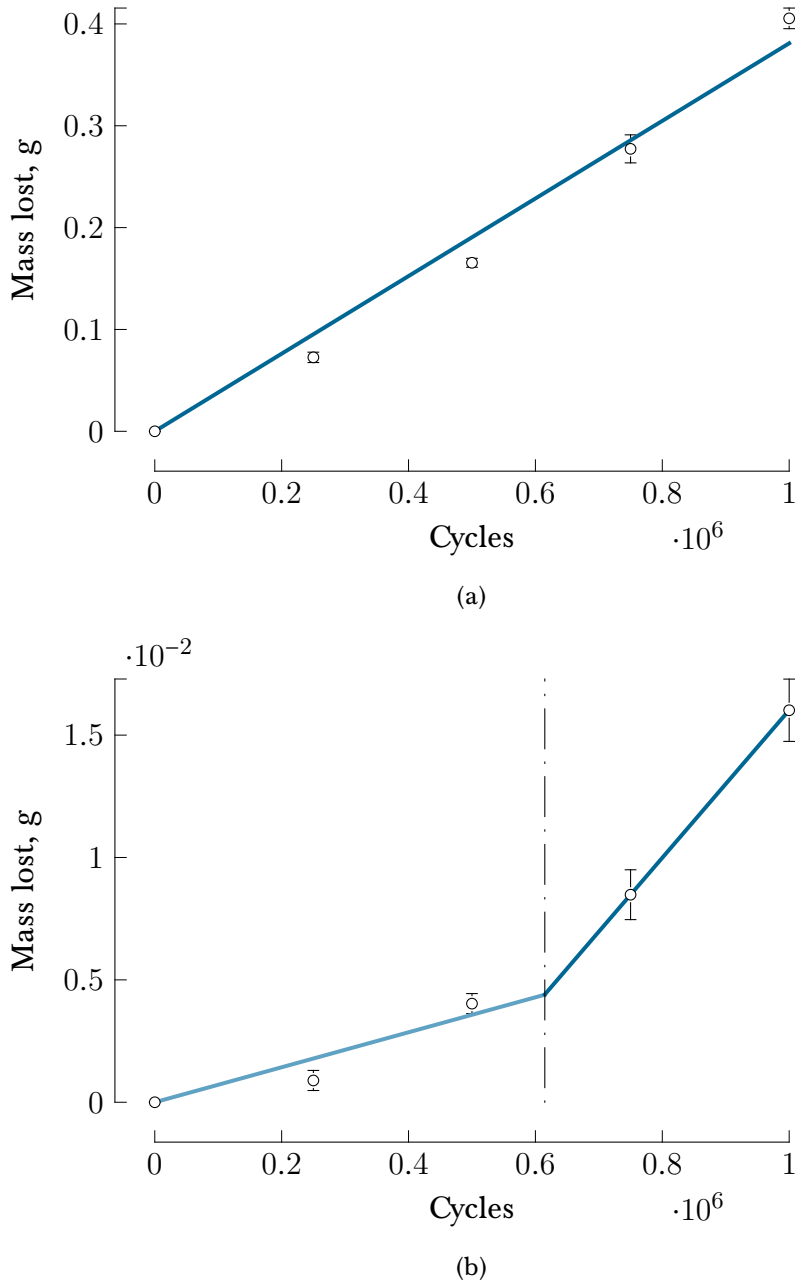

FIGURE 6.12 – The mean ± SD mass loss of the implants where: (a) is the mass lost from the PEKK sockets fitted with a linear regression; and (b) is the mass lost from the metal balls, fitted with a segmented linear regression with one breakpoint. Note, some error bars are smaller than the data points.

wear on the shoulders of the ball and socket, where the socket's wear has been so severe, there has been impact and rubbing between the shoulders at the extreme limits of the flexion-extension axis. The bovine serum lubricant (photographed in figure 6.14) shows that after each 0.25 million cycles there was large amounts of wear debris released into the lubricant.

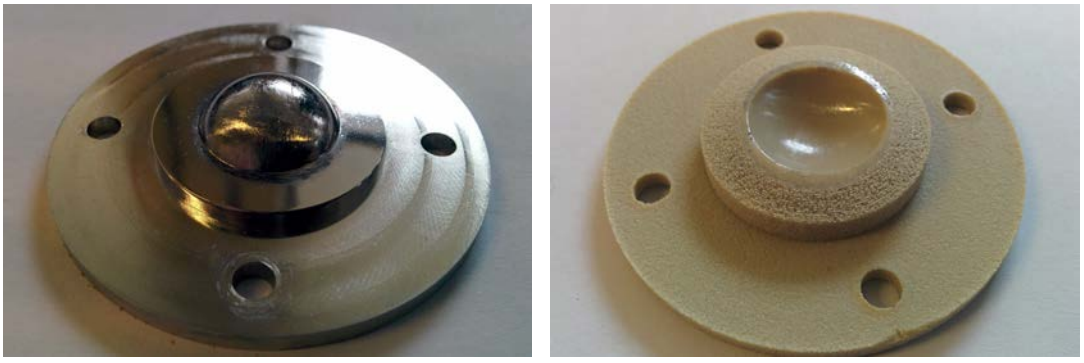

(a) (b)

FIGURE 6.13 – The (a) metal and the (b) PEKK implants after 1 million cycles.

(a) (b)

FIGURE 6.14 – The low concentration bovine serum (a) prior to wear tests, and (b) after 0.25 million cycles; the opaqueness is due to wear debris

Alicona Wear Volume

To measure the wear rate volumetrically, the PEKK discs were scanned before testing and then at 1 million cycles. Example before and after scans of the PEKK socket from the Alicona are shown in figure 6.15. The black areas are where the Alicona was unable to measure data, caused by the sides of the implant becoming more reflective (polished by the wear process) and steeper. Due to the amount of missing data it was not possible to accurately measure volumetric loss with this method, although it was successful for the measurement of wear scars in ceramic-on-ceramic cervical disc wear tests (Green, N. C., unpublished results, University of Birmingham)

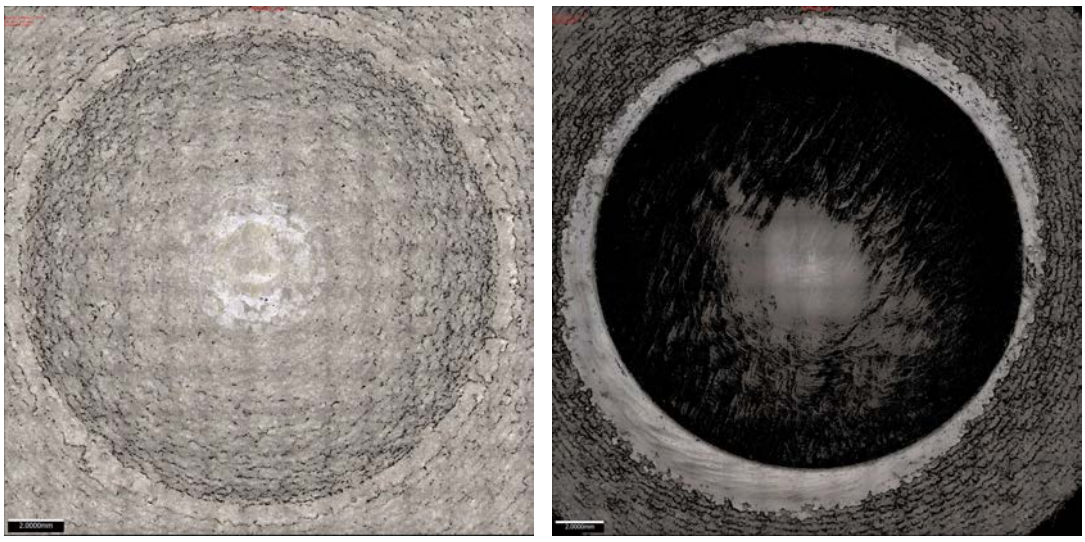

(a) (b)

FIGURE 6.15 – The implant scanned by the Alicona Infinite Focus (a) before the wear test, (b) after 1 million cycles. The black areas are missing data points.

as shown in table 3.3.

Note the scratch marks on the rim of the socket which has been worn flat in the direction of maximum extension and on the base of the socket, these scratches are characteristic of abrasive wear, likely from third body wear particles.

6.4 Discussion

6.4.1 Material properties and tolerances

The geometric analysis shows the sintered PEKK is capable of accurately reproducing simple geometries to $<5\,\%$ error from specified. However the 3D printing process seems unable to accurately reproduce curved surfaces in the z-axis to the tolerances required for the bearing area of a total joint replacement (TJR) (British Standards Institution, 2011c). The clearance between the metal ball and PEKK socket was $\approx 4\times$ larger than specified. From the drawings the

clearance should have been $0.35\,\mathrm{mm}$. By using the Hertzian elastic contact equations in §3.3.1, it can be seen that the contact pressure exerted on the bearing contact is much greater than what is seen in a Charité implant.

If this manufacturing method is to be used for implant manufacture, designs would need substantial changes and careful thought to take advantage of the manufacturing process compared to traditionally manufactured implants. Both to minimise issues inherent to the manufacturing process and to compensate for shrinkage causing inaccuracy in manufactured parts. Shrinkage is a common problem in SLS components, and it's minimisation often requires empirical experimentation (Raghunath and Pandey, 2007; Wang, 1999).

From the roughness profiles it can be seen that the R_{sk} is close to 0 (equal volumes of peaks to troughs). Ideally, a heavy negative R_{sk} would be preferred, as a minimisation of peaks would increase real contact area—decreasing contact pressures and therefore stresses. The negative R_{sk} would maintain the presence of pits, enabling the entrapment of lubricant and debris (Ito et al., 2000).

6.4.2 Tribology

As shown in figure 6.11, the frictional torques of the sintered PEKK was higher than that of UHMWPE (Moghadas et al., 2013a) in ringers solution—despite the same viscosities. However, this was not unexpected, as the surface finish and material choice are not optimised for low friction, which is not the same as low wear.[2] From the HFRR, in the high concentration of bovine serum, the mean friction coefficient after bedding in for PEKK is 0.256 ± 0.003.

[2] A case in point is the 'Teflon' hip implant mentioned in § 2.1.

The mean friction coefficient after bedding in for UHMWPE was 0.148 ± 0.001. The friction coefficient for PEKK is 1.7 times higher than UHMWPE. By comparing the Stribeck curves of the low concentration of bovine serum to the 'ideal' Stribeck curve in figure 6.5, it is apparent that in the lubrication regime was boundary (the friction factor is invariant to Sommerfeld number). As shown by Moghadas et al. (ibid.), the shape of the Stribeck curve does not appreciably change between ringers solution and bovine serum, i.e. the curves show boundary lubrication in both lubricants. Therefore, it is likely that the PEKK implant would still be in boundary lubrication in the high concentration of bovine serum.

The mass loss of the PEKK socket was linear and catastrophic, losing 0.3810 ± 0.0155 g/million cycles. This wear rate is 31.75 times higher than the UHMWPE wear rate reported by Moghadas, Mahomed, Shepherd, et al. (2015) who's results were in agreement with other literature (Prokopovich et al., 2011; Vicars et al., 2009). The implant did not survive 1 million cycles. After each 0.25 million cycles there was large quantities of wear debris present in the bovine serum lubricant (see figure 6.14), *in vivo* this would have been released into periprosthetic tissue where PEKK debris may illicit an immune reaction.

The mass loss for the CoCrMo ball had two gradients, an initial wear rate of $(7.16 \pm 1.27) \times 10^{-3}$ g/million cycles; after the first 0.614 ± 0.061 million cycles the wear rate increased to a gradient of $(30 \pm 4) \times 10^{-3}$ g/million cycles.[3] It is not unusual for metal components to have a segmented mass loss, however the second section is usually a smaller gradient (Dowson et al., 2004; Moghadas et al.,

[3]the gradient of the second segment is the sum of coefficients 'x' and 'U1.x' from table 6.6.

2013b). The acceleration of wear of the metal implant was likely multi-factorial With the PEKK disc wearing rapidly, the surface morphology with debris trapping pits was soon replaced with a smooth surface. As the PEKK implant continued to wear at the same rate, this would have increased the amount of wear debris entrained between the bearing surfaces causing third body wear. The wear scars show scratching visible to the unaided eye demonstrating that abrasion was the main wear mode.

It is difficult to predict if a SLS produced material will have wear properties that are comparable or better to the traditionally manufactured counterpart (Kumar and Kruth, 2008). There are several factors in the manufacturing process which relate to the wear resistance of SLS components (Tsouknidas, 2011). While literature shows that SLS materials can be capable bearing materials, it does not appear that PEKK is suitable. Future work using sintered polymers for spinal implants may include the use of a filler material which can greatly increase the wear resistance (ibid.). Using polytetrafluoroethylene (PTFE) as a filler my offer greater reduction in wear (Burris and Sawyer, 2006), as may carbon fibre reinforcement (Wang, Lin, et al., 1999).

6.5 Chapter Summary

So again, to quote Shiers (1954): 'These results are not good—they are bad.' The wear rate of sintered PEKK was an order of magnitude higher than UHMWPE. Despite the PEKK only being wear tested at the low concentration of bovine serum, since the spinal implant operates in boundary lubrication, it is unlikely that the wear rate will

be reduced sufficiently for this material combination to be considered a viable option for spinal implants.

The geometric tolerance for the SLS process requires several iterations of adjustments on design, in future work controlling factors like laser speed may improve the geometric accuracy and wear abilities of sintered PEKK. By including both control over manufacturing parameters, and the inclusion of filler materials in the sintered polymer, it may be possible to produce an implant with favourable wear properties that can entrap wear debris.

Chapter 7

Overall Conclusions & Future Work

This thesis aimed to analyse the wear debris of ball and socket spinal implants from *in vitro* testing. By utilising robust methods in computer vision and machine learning for classification of wear debris it was found that *in vitro* testing of spinal implants reproduces similar sizes and morphologies to wear debris found in periprosthetic tissue recovered during revision surgery (Nine et al., 2014).

It was found that spinal implants using ultra-high molecular weight polyethylene (UHMWPE) also produce wear debris in the size range of 0.1–$1\,\mu\mathrm{m}$, the range shown both *in vivo* and *in vitro* to the greatest risk to inflammatory responses, and therefore osteolysis (Green, Fisher, Stone, et al., 1998). The mean size of wear debris from Charité implants was $2.89 \pm 0.20\,\mu\mathrm{m}$, however as the size distribution was log-normal, the most common size was $0.880\,\mu\mathrm{m}$. By checking these values against results from other particle sizing methods, such as low angle laser light scattering or analytical centrifuge, the results from this method could be verified. The aspect ratio of wear debris averaged 2.25 ± 0.05, similar to Punt, Baxter, et al. (2011). The most common morphology of wear debris was fibrils, long thin strands of UHMWPE. This morphology is often caused by abrasion or debris becoming entrained between the bearing surfaces – rolling the debris into cylindrical strands. This debris morphology is also seen a lot in literature for other joint replacement devices and in spines (Kurtz, Ooij, et al., 2007; Punt, Baxter, et al., 2011; Veruva et al., 2014). This morphology has been shown to cause more aggressive immune reactions compared to other morphologies (Yang et al., 2002).

The method for analysing wear debris was based upon Scale-Invariant Feature Transforms (SIFT), and it's capabilities in wear

debris analysis proved to be comparable to other, bespoke wear debris characterisation algorithms, as shown in chapter 4. By removing the need for the considerable programming expertise required to create an algorithm capable of recognising wear debris greatly increases the accessibility and reproducibility of wear debris analysis. The average accuracy of the machine learning algorithm using SIFT as an image quantizer was $77.60 \pm 4.65\,\%$. This accuracy is in-line with the performance of SIFT in general use—demonstrating that it is equally as good at characterising debris (Chatfield et al., 2011; Vedaldi and Fulkerson, 2010a). It was found that different wear debris morphologies were easier for the SIFT quantizer and Support Vector Machine (SVM) classifier to recognise than others. Fibrils, adhesive particles and spheres were the most likely to be successfully classified with few instances of false positives. Chips and sheets or flakes, however, were more challenging to classify. This was due to the sparsity of surface features present on these debris forms. In future efforts for wear debris recognition algorithms, a multi-factor classifier could be employed; by using multiple features of a debris particle, such as size and aspect ratio or energy-dispersive X-ray spectroscopy (EDS) data, the classifier would be less prone to miss-classification due to a particle being featureless in a particular metric. Additionally, different methods for isolating wear debris could be used, that do not lose small particles though filter holes, such as centrifuge sedimentation onto a silicon wafer (Visentin et al., 2004).

From this research, it is apparent that UHMWPE may be unsuitable for spinal implants, the material is already avoided for use in young patients for hip implants. As degenerative disc disease

(DDD) is typically found between the ages of 30–50, a young age for arthroplasty surgery, it is likely that patients will suffer the same 'particle disease' as UHMWPE hips. Therefore, different material combinations need researching to reduce the amount of damaging wear debris being released into periprosthetic tissue.

Based on literature suggesting the use of voids in a bearing surface may reduce abrasive wear and prevent the release of wear debris (Ito et al., 2000), and that selective laser sintering (SLS) manufactured parts can have favourable wear characteristics compared with the same material traditionally manufactured (Tsouknidas, 2011). In chapter 6 a polymer-on-metal implant was tribologically tested in an attempt to reduce wear debris release into periprosthetic tissue. The polymer chosen was Polyetherketoneketone (PEKK) as it had already been successfully used in SLS manufactured form in surgery; as a relative of Polyetheretherketone (PEEK) the wear debris could have less aggressive biological responses than UHMWPE (Kurtz and Devine, 2007; Toth et al., 2006). However, it was found that SLS PEKK does NOT perform well as a bearing material. The PEKK implants wore at 0.3810 ± 0.0155 g/million cycles, 31.75 times the rate of UHMWPE. An important parameter for wear is the hardness of the material, therefore both PEKK and possible PEKKs with a filler material should be hardness tested to ensure suitability as a bearing material.

In future work, the use of sintered PEKK may be possible by adding a filler material to the polymer matrix (Burris and Sawyer, 2006; Tsouknidas, 2011). Additionally, laser parameters influence the wear properties of an SLS manufactured product, and the dimensional accuracy of the SLS process. Through experimentation and

design iterations, an optimal parameters and geometries could be found that compromise wear behaviour with geometric tolerances. The wear of PEKK and other alternate materials should be performed in a lubricant that better replicated the fluid found *in vitro* between two vertebræ, possibly using hyaduronic acid and other bio-lubricants diluted in deionised water. It should be noted that albumin and other proteins can act as a sticking agent depending on the hydrophobic nature of the surfaces (Heuberger et al., 2005), this should therefore be taken into account when selecting bearing surfaces. Ideally, the lubricant in question would not contain proteins, allowing for long term wear tests which do not require cleaning every 0.25 million cycles. This would allow the effect of removing wear debris regularly to be measured compared with the standard protocol.

Appendix A

Code Functions

Code A.1 – `lumbarContact.m` calculates the maximum contact pressure and contact area.

```
function [P,a] = lumbarContact(F,r,R,Y,V)

    %  r radius of ball - CoCrMo Ball
    %  R radius of socket
    y = 240e9; %youngs modulus ball
    % Y youngs modulus socket
    v = 0.3; %poisson's ratio ball - CoCrMo
    % V poisson's ratio socket

    E = 1 / (((1 - v^2)/y) + ((1 - V^2)/Y)); %combined elastic modulus E*
    eR = 1 / ((1 / r) + (1 / R)) ; %effective radius
    a = ((3 * F * eR) / (4 * E)) ^ (1/3) ; %contact area
    P = (3 * F) / (2 * pi * a^2) ; %maximum contact pressure p0
end
```

CODE A.2 – linTemp.m is used to solve the temperature equation for unidirectional sliding, Eq 3.8.

```
function [T,maxTemp]=linTemp()
F = 0.981;
mu = 0.02;
freq=30;
omega = 2*pi*freq;
amp = 1e-3;
U = amp*omega;


K = 00.41; %thermal conductivity
ro = 930; %density
c = 1840; %specific heat capacity j/Kg

alpha = K/(ro*c); %thermal diffusivity
y = 210e9; %youngs modulus ball
Y = 0.9e9; %youngs modulus socket/disk
v = 0.3; %poisson's ratio ball
V = 0.46; %poisson's ratio socket/disk


%% ------ Hertzian contact ------------
rad = 0.003; %radius of ball
R = Inf; %radius of socket/disk

E = 1 / (((1 - v ^ 2) / y) + ((1 - V ^ 2) / Y)); %combined elastic
 ↪ modulus
eR = 1 / ((1 / rad) + (1 / R)) ; %effective radius
l = ((3 * F * eR) / (4 * E)) ^ (1 / 3) ; %contact area radius
P = (3 * F) / (2 * pi * l ^ 2) ; %maximum contact pressure
q = mu * P * U;
Pe = U * l / (2 * alpha);

%% ------ Temp calculation -------------

maxTemp=(2 / sqrt(pi)) * (q * l / K) * 1 / sqrt(Pe);
normT = @(T) T .* (alpha * sqrt(Pe) / (q * l));
N= [linspace(-2, -1.2, 5) linspace(-1.21, -0.6, 40) linspace(-0.6, 0.8,
 ↪ 8) linspace(0.8, 1.2, 20) linspace(1.2, 3, 40)];
x=N .* l;

tau = @(t) 0 - t;
myFunc2 = @(t, s, x) (1 ./ t) .* ((1 - (s / l) .^ 2) .^ (1 / 2)) .* exp(-
 ↪ (((x - s - U .* t) .^ 2) ./ (4 .* alpha .* t)));
for ii = 1:length(x)
```

```
42    T1(ii) = (q / (2 * pi * alpha)) * integral2(@(t, s)myFunc2(t, s,
      ↪  x(ii)), 0,
      ↪  Inf,-l,l,'method','iterated','AbsTol',1e-13,'RelTol',1e-8);
43  end
44  figure(2)
45  T = normT(T1);
46  plot(x/l,normT(T1))
```

Code A.3 – oscTemp.m is used to solve the temperature equation for oscillating sliding, Eq 3.14.

```
function [T,maxTemp]=oscTemp()
F = 0.981;
mu = 0.02;
freq=30;
omega = 2*pi*freq;
amp = 1e-3;

K = 00.41; %thermal conductivity
ro = 930; %density
c = 1840; %specific heat capacity j/Kg

alpha = K/(ro*c); %thermal diffusivity
y = 210e9; %youngs modulus ball
Y = 0.9e9; %youngs modulus socket/disk
v = 0.3; %poisson's ratio ball
V = 0.46; %poisson's ratio socket/disk


%% ------ Hertzian contact ------------
rad = 0.003; %radius of ball
R = Inf; %radius of socket/disk

E = 1 / (((1 - v ^ 2) / y) + ((1 - V ^ 2) / Y)); %combined elastic
 ↪ modulus
eR = 1 / ((1 / rad) + (1 / R)) ; %effective radius
l = ((3 * F * eR) / (4 * E)) ^ (1 / 3) ; %contact area radius
P = (3 * F) / (2 * pi * l^2) ; %maximum contact pressure
U = amp * omega;
q = mu * P * U;
Pe = U * l / (2 * alpha);

%% ------ Temp calculation -------------

normT = @(T) T .* (alpha * sqrt(Pe) / (q * l));
normT2 = @(T) T .* (alpha/(2 * q * l));

t = [linspace(0.001, 0.01, 5) linspace(0.01, 1, 50) linspace(1, 5, 10)
 ↪ linspace(5, 100, 10) linspace(100, 1000, 10)];

tau = @(t) 0 - t;
myFunc2 = @(t, s, x) (abs(sin(omega .* (t)))./(t .^ (3 / 2))) .* ((1 - (s
 ↪ / l) .^ 2) .^ (1 / 2)) .* exp(- (((x - s - amp .* (1 + sin(omega .*
 ↪ t))) .^2) ./ (4 .* alpha .* t)));

```

```
for ii = 2:length(t)
  T1(ii) = (q / (2 * pi * alpha)) * integral2(@(t, s)myFunc2(t, s, 0),
  ↪ t(ii - 1), t(ii), -l, l, 'method', 'iterated', 'AbsTol', 1e-13,
  ↪ 'RelTol', 1e-8);
  end
figure(1)
T = normT(T1);
semilogx(t,normT(cumsum(T1)))
xlabel('Time, s')
ylabel('T')

figure(3)
plot(t,(cumsum(normT(T1))))
xlabel('Time, s')
ylabel('T')
```

CODE A.4 – genAliconaImport.m imports csv tuplets data from the Alicona Infinate Focus into MATLAB and performs various mathematical or plotting functions depending upon the inputs given.

```
function [ output, struct] = genAliconaImport(filename, varargin)

    %   Import alicona data to matlab from a text file. It takes the form
    %   of
    %   [primary, struct] = genAliconaImport('path/to/file.txt',
    'option1',
    %   value1, ..., 'optionN', valueN);


    %   This program will assume a single line header and footer on text
    files
    %   unless otherwise specified with the options:
    %   'startRow' & 'endRow'.

    %   To find the volume between the surface and the z plane, set
    %   'findVolume' to true.

    %   To plot the data, set 'plot' to one of the following:
    %   'contour', 'contourf', 'contour3', 'mesh', or 'surf'.

    %   To crop data, use 'crop' followed by [xmin,xmax,ymin,ymax]. N.B.
    these
    %   must be scaled to the new size!
    %

    % Author David Eckold

    %% input argument parser
    defaultStartRow = 2;
    defaultEndRow = (numel(textread(filename,'%1c%*[^\n]')))-1;
    defaultScale = 1;
    defaultInterp = 'natural';
    defaultFindVol = false;
    defaultPlot = false;
    defaultContourLayers = 20;
    defaultCrop = false;
    expectedInterp = {'nearest','linear','natural'};
    expectedPlot = { 'contour', 'contourf', 'contour3', 'mesh',
    'surf'};
    err = 'Value must be a positive number.';
    validationFunc = @(x) assert(isnumeric(x) && isscalar(x) && (x > 0),
    err);

```

```
38
39      p = inputParser;
40      addRequired(p,'filename',@ischar);
41      addParamValue(p,'startRow',defaultStartRow,validationFunc);
42      addParamValue(p,'endRow',defaultEndRow,validationFunc);
43      addParamValue(p,'scale',defaultScale,validationFunc);
44      addParamValue(p,'interpolant',defaultInterp,@(x)
    ↪   any(validatestring(x,expectedInterp)));
45      addParamValue(p,'findVolume',defaultFindVol,@islogical);
46      addParamValue(p,'plot',defaultPlot,@(x)
    ↪   any(validatestring(x,expectedPlot)));
47      addParamValue(p,'contourLayers', defaultContourLayers,
    ↪   validationFunc);
48      addParamValue(p,'crop', defaultCrop)
49
50      parse(p,filename,varargin{:});
51
52      %% Import data from Alicona file to tuplets.
53      startRow = p.Results.startRow;
54      endRow = p.Results.endRow;
55
56      formatSpec = '%13f%13f%f%[^\n\r]';
57
58      % Open the text file.
59      fileID = fopen(filename,'r');
60
61      dataArray = textscan(fileID, formatSpec, endRow(1) - startRow(1)+1,
    ↪   'Delimiter', '', 'WhiteSpace', '', 'HeaderLines', startRow(1) - 1,
    ↪   'ReturnOnError', false);
62
63      % Close the text file.
64      fclose(fileID);
65
66      % Create output variable
67      xyz = [dataArray{1:end-1}];
68
69      %% Convert Alicona tuplets to nxmx3 Mesh.
70      scale = p.Results.scale;
71
72      x = xyz(:,1); y = xyz(:,2); z = xyz(:,3);
73      x = x*scale; y = y*scale; z = z*scale;
74      dx = abs(x(find(diff(x), 1) + 1) - x(1));
75      dy = abs(y(find(diff(y), 1) + 1) - y(1));
76
77      if p.Results.crop == 0
78          xvg = min(x):dx:max(x);
79          yvg = min(y):dy:max(y);
```

```
80      elseif length(p.Results.crop) == 4;
81          xvg = p.Results.crop(1):dx:p.Results.crop(2);
82          yvg = p.Results.crop(3):dy:p.Results.crop(4);
83      else
84          error('Incorrect number of inputs')
85      end
86
87
88      F = scatteredInterpolant(x,y,z,p.Results.interpolant,'none');
89      [vx,vy] = ndgrid(xvg,yvg);
90      vz = F(vx,vy);
91
92      %% write outputs and plot graphs if called for
93
94      if p.Results.findVolume == 1
95          output = dx*dy*sum(vz(:));
96          struct.xyz(:,:,1) = vx;
97          struct.xyz(:,:,2) = vy;
98          struct.xyz(:,:,3) = vz;
99      else
100         output(:,:,1) = vx;
101         output(:,:,2) = vy;
102         output(:,:,3) = vz;
103     end
104
105     struct.d = [dx dy];
106     struct.F = F;
107
108     if p.Results.plot ~= 0
109         figure
110         if any(strcmp(p.Results.plot,{'contour', 'contourf',
    ↪ 'contour3'})) == 1;
111             feval(p.Results.plot, vx, vy, vz, p.Results.contourLayers)
112             c = colorbar;
113             ylabel(c, 'z, m')
114         else
115             feval(p.Results.plot, vx, vy, vz);
116             zlabel('z, m')
117         end
118         ylabel('y, m')
119         xlabel('x, m')
120     end
121 end
```

CODE A.5 – `findPeaks.R` takes the dataframe of block data containing Mx.Moment and My.Moment data columns, and outputs the abs of the final 20 peaks and troughs of the chosen moment axis. This function is called by 'meanFriction' which will calculate the mean and standard deviation from two dataframes.

```
require(wmtsa)

#This function will output the final 20 absolute values of peaks and troughs of
#a time series given time series data 'data' and axis 'Mx' or 'My'.

meanFriction<-function(data1,data2,axis){
  lst1<-findPeaks(data1,axis)
  lst2<-findPeaks(data2,axis)
  meanfric<-findMean(lst1,lst2)
  return(list(meanfric,lst1$SD,lst2$SD))
}


findPeaks<-function(data,axis){
  data.Split<- split(data,cumsum(is.na(data$Points)))
  switch(axis,
         Mx={
           extract <-lapply(
             data.Split, function(xl) tail(na.omit(xl$Mx.Moment), n=40000)
           )
           extract<-lapply(extract,function(x) x-mean(x))
         },
         My={
           extract<-lapply(
             data.Split, function(xl) tail(na.omit(xl$My.Moment), n=40000)
           )
           extract<-lapply(extract,function(x) x-mean(x))
         }
  )
  Peaks <- lapply(
    extract,function(x)
      wavCWTPeaks(
        wavCWTTree(
          wavCWT(
            abs(
              x
            )
          )
        )
      )
```

```
  )
  peakValues<-lapply(
    Peaks,function(xl) tail(xl$y[xl$y>10],n=24)
  )
  peakTimes<- lapply(
    Peaks,function(xl2) tail(xl2$x[xl2$y>10],n=24)
  )
  peakValues.avg<-lapply(
    peakValues, function(xd) mean(head(xd,n=20))
  )
  meandat <- mean(unlist(peakValues.avg))
  sddat<- sqrt(var(unlist(peakValues.avg)))
  listdat<- list("Mean"=meandat,"SD"=sddat,"Peaks"=peakValues,"Peak
  ↪  times"=peakTimes)
# listdat<-list("Peaks"=peakValues,"Time"=peakTimes)
return(listdat)
}

findMean<-function(ls1,ls2){
  m<- mean(c(ls1$Mean,ls2$Mean))
  sd<-sqrt(var(c(ls1$Mean,ls2$Mean)))
  return(list("Mean"=m,"SD"=sd))
}
```

Appendix B

Engineering Drawings

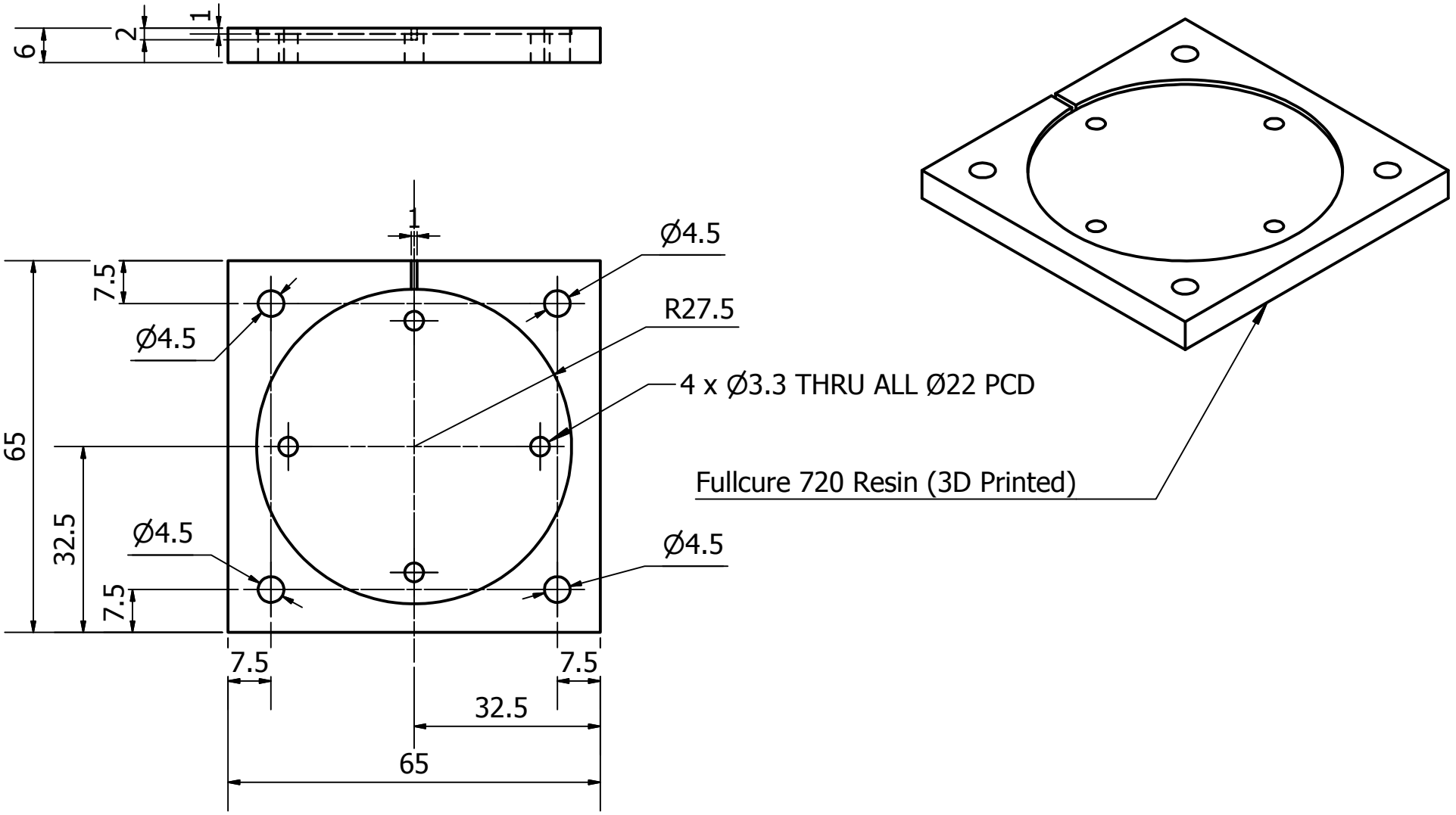

TOLERANCES
Tolerances unless otherwise stated:

Whole numbers	+/- 0.25
One decimal place	+/- 0.10
Two decimal places	+/- 0.05

DRAWN BY
Naomi Green

DIMENSIONS ARE IN mm

DATE
24/01/2014

3rd ANGLE PROJECTION

TITLE
Alicona Fixture

SIZE
A4

REV
1

SCALE 1:1

SHEET 1 of 1

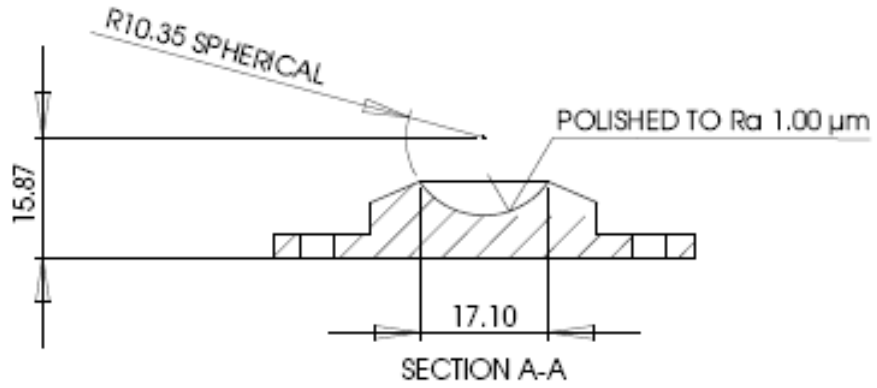

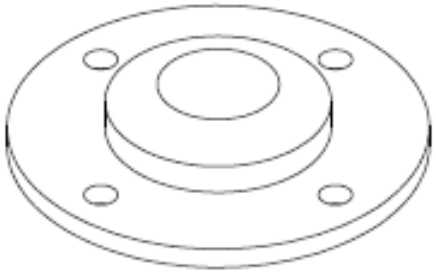

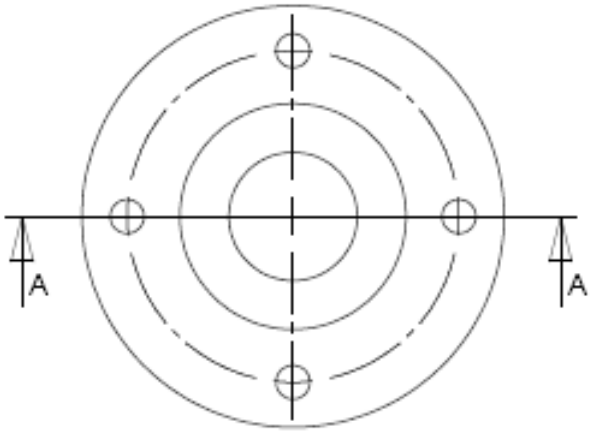

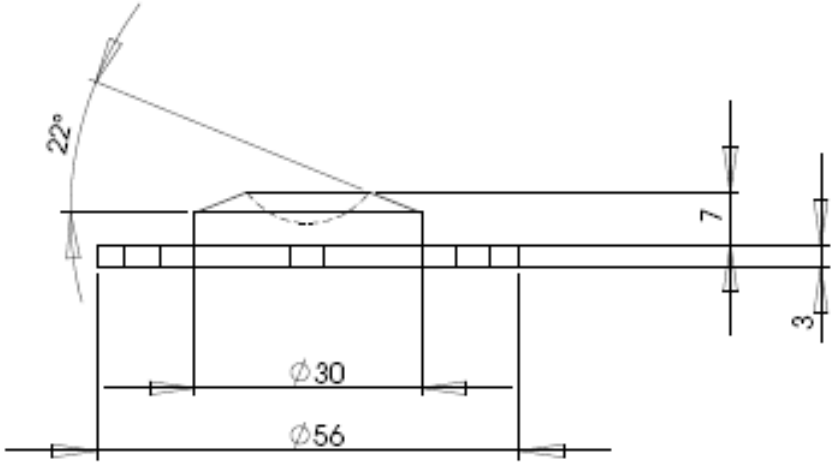

Tolerance unless otherwise stated:
whole numbers ± 0.25
one decimal place ± 0.10
two decimal places ± 0.05

MATERIAL
UHMWPE

DIMENSIONS ARE IN MM

DRAWN BY:
PARSHA MOGHADAS
09 DECEMBER 2010

SIZE A

DWG. NO. UB-implant-10-POM

REV 2

SCALE: 1:1

SHEET 1 OF 1

5 4 3 2 1

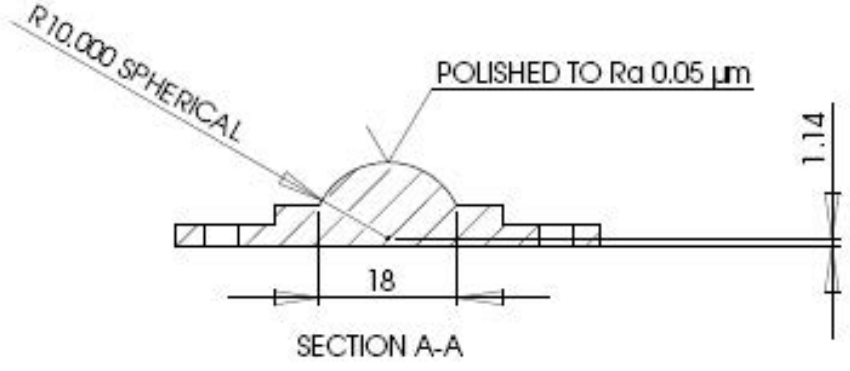

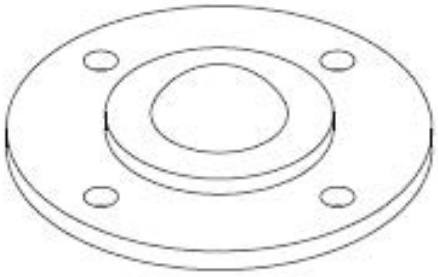

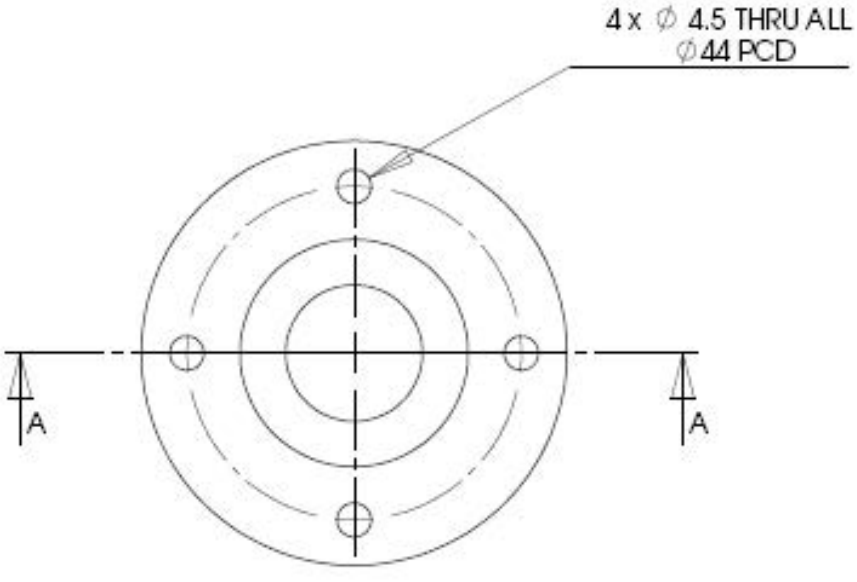

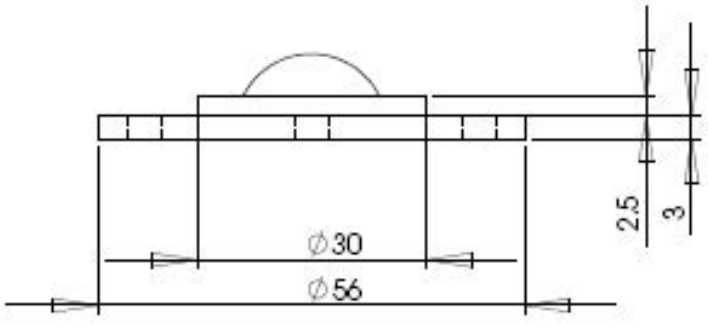

Tolerance unless otherwise stated:
whole numbers ± 0.25
one decimal place ± 0.10
two decimal places ± 0.05

MATERIAL
Cobalt Chrome to ASTM F799-96
(Co-27 Cr-5.5 Mo-0.06C)

DIMENSIONS ARE IN MM

DRAWN BY:
PARSHA MOGHADAS
09 December 2010

SIZE	DWG. NO.	REV
A	LB-implant-10-POM	2
SCALE: 1:1		SHEET 1 OF 1

5 4 3 2 1

List of References

Adams, M. A. and Dolan, P. (2012). "Intervertebral disc degeneration: evidence for two distinct phenotypes". In: ***Journal of anatomy*** 221.6, pp. 497–506.

Alicona Reference Documentation (2013). Alicona Imaging GmbG.

Alitappeh, R. J., Saravi, K. J., and Mahmoudi, F. (2012). "A New Illumination Invariant Feature Based on SIFT Descriptor in Color Space". In: ***Procedia Engineering*** 41, pp. 305–311.

ASTM F2423 - 05 Standard Guide for Functional, Kinematic, and Wear Assessment of Total Disc Prostheses (2005). Vol. 13.

ASTM F1877-05(2010) Standard Practice for Characterization of Particles (2009). Vol. 14.

Amstutz, H. C., Campbell, P., Kossovsky, N., and Clarke, I. C. (1992). "Mechanism and clinical significance of wear debris-induced osteolysis." In: ***Clinical orthopaedics and related research*** 276, pp. 7–18.

Anderson, D. P. (1982). ***Wear Particle Atlas. Revised***. DTIC Document, p. 163.

August, A., Aldam, C., and Pynsent, P. (1986). "The McKee-Farrar hip arthroplasty. A long-term study". In: ***Journal of Bone & Joint Surgery, British Volume*** 68.4, pp. 520–527.

Baer, W. S. et al. (1918). "Arthroplasty with the aid of animal membrane". In: ***Am J Orthop Surg*** 16, pp. 1–29.

Bentley, J. L. (1975). "Multidimensional Binary Search Trees Used for Associative Searching". In: ***Commun. ACM*** 18.9, pp. 509–517.

Bogduk, N. (2005). ***Clinical anatomy of the lumbar spine and sacrum***. Elsevier Health Sciences.

Boiman, O., Shechtman, E., and Irani, M. (2008). "In Defense Of Nearest-neighbor Based Image Classification". In: *2008 IEEE Conference on Computer Vision and Pattern Recognition*. IEEE, pp. 1–8.

Bosch, A., Zisserman, A., Mu, X., and Munoz, X. (2007). "Image Classification Using Random Forests And Ferns". In: *ICCV*. Vol. pages, pp. 1–8.

Briscoe, B. (1982). *Friction and wear in polymer-based materials.*

BS ISO 4288:1998 Geometric product specification (GPS). Surface texture. Profile method: Rules and procedures for the assessment of surface texture (1997).

BS ISO 18192-1:2008 Implants for surgery—Wear of total intervertebral spinal disc prostheses. Part 1: Loading and displacement parameters for wear testing and corresponding environmental conditions for test (2008).

BS ISO 4287: 2009 Geometrical Product Specifications (GPS)-Surface texture: Profile method–Terms, definitions and surface texture parameters (ISO 4287: 1997+ Cor 1: 1998+ Cor 2: 2005+ Amd 1: 2009)(includes Corrigendum AC: 2008 and Amendment A1: 2009) (2009).

BS ISO 17853:2011 Wear Of Implant Materials—Polymer And Metal Wear Particles – Isolation And Characterization (2011a). British Standards Online.

BS ISO 18192-1:2011 Implants For Surgery—Wear Of Total Intervertebral Spinal Disc Prostheses Part 1: Loading And Displacement Parameters For Wear Testing And Corresponding Environmental Conditions For Test (2011b). British Standards Institution.

BS ISO 7206-2:2011 Implants for surgery—Partial and total hip joint prostheses. Part 2: Articulating surfaces made of metallic, ceramic and plastics materials (2011c). British Standards Online.

Brown, S. R., Davies, W. A., DeHeer, D. H., and Swanson, A. B. (2002). "Long-term survival of McKee-Farrar total hip prostheses." In: ***Clinical orthopaedics and related research*** 402, pp. 157–163.

Bryant, M., Ward, M., Farrar, R., Freeman, R., Brummitt, K., Nolan, J., and Neville, A. (2014). "Characterisation of the surface topography, tomography and chemistry of fretting corrosion product found on retrieved polished femoral stems". In: ***Journal of the mechanical behavior of biomedical materials*** 32, pp. 321–334.

Buehler Reference Documentation (2001).

Burris, D. L. and Sawyer, W. G. (2006). "A low friction and ultra low wear rate PEEK/PTFE composite". In: ***Wear*** 261.3, pp. 410–418.

Canny, J. (1986). "A computational approach to edge detection." In: ***Transactions on pattern analysis and machine intelligence*** 8.6, pp. 679–698.

Carslaw, H. S. and Jaeger, J. C. (1959). ***Conduction of heat in solids***. Vol. 1.

Charnley, J. (1963). "Tissue reactions to polytetrafluorethylene". In: ***The Lancet*** 282.7322, p. 1379.

— (1972). "The long-term results of low-friction arthroplasty of the hip performed as a primary intervention". In: ***Journal of Bone & Joint Surgery, British Volume*** 54.1, pp. 61–76.

Chatfield, K., Lempitsky, V., Vedaldi, A., and Zisserman, A. (2011). "The devil is in the details: an evaluation of recent feature encoding methods". In: *BMVC*.

Chen, S., Li, Z., and Xu, Q. (2006). "Grey target theory based equipment condition monitoring and wear mode recognition". In: ***Wear*** 260.4-5, pp. 438–449.

Chyr, A., Qiu, M., Speltz, J. W., Jacobsen, R. L., Sanders, A. P., and Raeymaekers, B. (2014). "A patterned microtexture to reduce friction and increase longevity of prosthetic hip joints". In: ***Wear*** 315.1, pp. 51–57.

Constantine, W. and Percival, D. (2013). *wmtsa: Wavelet Methods for Time Series Analysis*. R package version 2.0-0.

Cook, R. B., Bolland, B. J., Wharton, J. A., Tilley, S., Latham, J. M., and Wood, R. J. (2013). "Pseudotumour formation due to tribocorrosion at the taper interface of large diameter metal on polymer modular total hip replacements". In: ***The Journal of arthroplasty*** 28.8, pp. 1430–1436.

Cook, R., Shearwood-Porter, N., Nicolae, C., Bolland, B., Latham, J., and Wood, R. (2013). "The Mechanism and Magnitude of Tribocorrosion Damage at the Cement-Stem Interface of Total Hip Replacements". In: ***Bone & Joint Journal Orthopaedic Proceedings Supplement*** 95.SUPP 34, pp. 36–36.

Cortes, C. and Vapnik, V. (1995). "Support-vector networks". In: ***Machine Learning*** 20.3, pp. 273–297.

Coventry, M. B. (1969). "Anatomy of the Intervertebral Disk." In: ***Clinical orthopaedics and related research*** 67, pp. 9–15.

Cramer, G. D. and Darby, S. A. (2013). ***Clinical Anatomy of the Spine, Spinal Cord, and ANS***. Elsevier Health Sciences.

Crawford, R. and Murray, D. (1997). "Total hip replacement: indications for surgery and risk factors for failure". In: ***Annals of the rheumatic diseases*** 56.8, pp. 455–457.

Cunningham, B. W., Hallab, N. J., Hu, N., and McAfee, P. C. (2013). "Epidural application of spinal instrumentation particulate wear debris: a comprehensive evaluation of neurotoxicity using an in vivo animal model". In: ***Journal of neurosurgery. Spine*** 19.3, pp. 336–350.

Delignette-Muller, M. L. and Dutang, C. (2015). "fitdistrplus: An R Package for Fitting Distributions". In: ***Journal of Statistical Software*** 64.4, pp. 1–34.

Dowson, D., Hardaker, C., Flett, M., and Isaac, G. H. (2004). "A hip joint simulator study of the performance of metal-on-metal joints: Part I: The role of materials". In: ***The Journal of arthroplasty*** 19.8, pp. 118–123.

Du, P., Kibbe, W. A., and Lin, S. M. (2006). "Improved peak detection in mass spectrum by incorporating continuous wavelet transform-based pattern matching". In: ***Bioinformatics*** 22.17, pp. 2059–2065.

Eckold, D. G., Dearn, K. D., and Shepherd, D. E. T. (2015). "The evolution of polymer wear debris from total disc arthroplasty". In: ***Biotribology*** 1–2, pp. 42–50.

Efron, B. (1979). "Bootstrap methods: another look at the jackknife". In: ***The annals of Statistics***, pp. 1–26.

Erdemir, A. (2005). "Review of engineered tribological interfaces for improved boundary lubrication". In: ***Tribology International*** 38.3, pp. 249–256.

Etsion, I. (2004). "Improving tribological performance of mechanical components by laser surface texturing". In: ***Tribology letters*** 17.4, pp. 733–737.

Everingham, M., Van Gool, L., Williams, C. K. I., Winn, J., and Zisserman, A. (2010). "The pascal visual object classes (VOC) challenge". In: ***International Journal of Computer Vision*** 88.2, pp. 303–338.

Ferry, J. D. (1980). ***Viscoelastic properties of polymers***. John Wiley & Sons.

Fogh-Andersen, N., Altura, B. M., Altura, B. T., and Siggaard-Andersen, O. (1995). "Composition of interstitial fluid." In: ***Clinical chemistry*** 41.10, pp. 1522–1525.

Ge, S., Wang, S., Gitis, N., Vinogradov, M., and Xiao, J. (2008). "Wear behavior and wear debris distribution of UHMWPE against Si_3N_4 ball in bi-directional sliding". In: ***Wear*** 264.7-8, pp. 571–578.

Gladkis, L. G., Timmers, H., Scarvell, J. M., and Smith, P. N. (2011). "Detailed three-dimensional size and shape characterisation of UHMWPE wear debris". In: ***Wear*** 270.7-8, pp. 455–463.

Gonzalez, R. C., Woods, R. E., and Eddins, S. L. (2009). ***Digital image processing using MATLAB***. Gatesmark Publishing.

Goodman, S., Fornasier, V., Lee, J., and Kei, J. (1990). "The histological effects of the implantation of different sizes of polyethylene particles in the rabbit tibia". In: ***Journal of biomedical materials research*** 24.4, pp. 517–524.

Gray, H. (1918). ***Anatomy of the human body***. Lea & Febiger.

Green, T. R., Fisher, J., Stone, M., Wroblewski, B., and Ingham, E. (1998). "Polyethylene particles of a 'critical size' are necessary for the induction of cytokines by macrophages in vitro". In: ***Biomaterials*** 19.24, pp. 2297–2302.

Green, T. R., Fisher, J., Bridget Matthews, J., Stone, M. H., and Ingham, E. (2000). "Effect of size and dose on bone resorption activity of macrophages by in vitro clinically

relevant ultra high molecular weight polyethylene particles". In: ***Journal of Biomedical Materials Research*** 53.5, pp. 490–497.
Greenwood, J. A. (1967). "The area of contact between rough surfaces and flats". In: ***Journal of Tribology*** 89.1, pp. 81–87.
Greenwood, J. A. and Tripp, J. H. (1967). "The elastic contact of rough spheres". In: ***Journal of Applied Mechanics*** 34.1, pp. 153–159.
Hallab, N. J. and Jacobs, J. J. (2009). "Biologic effects of implant debris". In: ***Bulletin of the NYU Hospital for Joint Diseases*** 67.2, pp. 182–188.
Harris, W. H. (1994). "Osteolysis and particle disease in hip replacement: a review". In: ***Acta Orthopaedica*** 65.1, pp. 113–123.
— (1995). "The problem is osteolysis." In: ***Clinical orthopaedics and related research*** 311.311, pp. 46–53.
— (2001). "Wear and periprosthetic osteolysis: the problem." In: ***Clinical orthopaedics and related research*** 393, pp. 66–70.
Hartigan, J. A. and Wong, M. A. (1979). "Algorithm AS 136: A K-Means Clustering Algorithm". In: ***Wiley for the Royal Statistical Society*** 28.1, pp. 100–108.
Haynes, D. R., Boyle, S. J., Rogers, S. D., Howie, D. W., and Vernon-Roberts, B. (1998). "Variation in cytokines induced by particles from different prosthetic materials." In: ***Clinical orthopaedics and related research*** 352, pp. 223–230.
Heuberger, M., Widmer, M., Zobeley, E., Glockshuber, R., and Spencer, N. (2005). "Protein-mediated boundary lubrication in arthroplasty". In: ***Biomaterials*** 26.10, pp. 1165–1173.
Hickey, S. D. and Hukins, D. W. L. (1980). "Relation between the structure of the annulus fibrosus and the function and failure of the intervertebral disc." In: ***Spine*** 5.2, pp. 106–116.
Hilibrand, A. S. and Robbins, M. (2004). "Adjacent segment degeneration and adjacent segment disease: the consequences of spinal fusion?" In: ***The Spine Journal*** 4.6, S190–S194.
Hirakawa, K., Bauer, T. W., Stulberg, B. N., and Wilde, A. H. (1996). "Comparison and quantitation of wear debris of failed total hip and total knee arthroplasty". In: ***Journal of biomedical materials research*** 31.2, pp. 257–263.
Hongtao, L., Shirong, G., Shoufan, C., and Shibo, W. (2011). "Comparison of wear debris generated from ultra high molecular weight polyethylene in vivo and in artificial joint simulator". In: ***Wear*** 271.5-6, pp. 647–652.
Hoskins, T. J. (2015). "The mechanical and tribological properties of PEEK gears". PhD thesis. University of Birmingham.
Hukins, D. W. and Meakin, J. R. (2000). "Relationship between structure and mechanical function of the tissues of the intervertebral joint". In: ***American Zoologist*** 40.1, pp. 42–052.
Hunt, T. M. (1993). ***Handbook of wear debris analysis and particle detection in liquids.*** Springer Science & Business Media.
Ingham, E. and Fisher, J. (2000). "Biological reactions to wear debris in total joint replacement." In: ***Proceedings of the Institution of Mechanical Engineers. Part H, Journal of engineering in medicine*** 214.1, pp. 21–37.
Ito, H., Kaneda, K., Yuhta, T., Nishimura, I., Yasuda, K., and Matsuno, T. (2000). "Reduction of polyethylene wear by concave dimples on the frictional surface in artificial hip joints". In: ***The Journal of arthroplasty*** 15.3, pp. 332–338.

Jagur-Grodzinski, J. (1999). "Biomedical application of functional polymers". In: ***Reactive and Functional Polymers*** 39.2, pp. 99–138.

Jennings, A. (2013). *Sphere Fit (least squared).* URL: https://www.mathworks.com/matlabcentral/fileexchange/34129-sphere-fit--least-squared- (visited on 02/19/2014).

Johnson, K. (1986). ***Contact mechanics***. Ninth. Cambridge University Press.

Joshi, R. P., Eftekhar, N. S., McMahon, D. J., and Nercessian, O. A. (1998). "Osteolysis after Charnley primary low-friction arthroplasty A COMPARISON OF TWO MATCHED PAIRED GROUPS". In: ***Journal of Bone & Joint Surgery, British Volume*** 80.4, pp. 585–590.

Joy, D. C. and Joy, C. S. (1996). "Low voltage scanning electron microscopy". In: ***Micron*** 27.3–4, pp. 247–263.

Katti, K. S. (2004). "Biomaterials in total joint replacement". In: ***Colloids and Surfaces B: Biointerfaces*** 39.3, pp. 133–142.

Kewekordes, T., Wille, S., and Kern, M. (2014). "Wear of polyetherketoneketone (PEKK) caused by different antagonists". In: ***Dental Materials*** 30, e77.

Kirk, T. B., Panzera, D., Anamalay, R., and Xu, Z. (1995). "Computer image analysis of wear debris for machine condition monitoring and fault diagnosis". In: ***Wear*** 181-183, pp. 717–722.

Knight, S. R., Aujla, R., and Biswas, S. P. (2011). "Total Hip Arthroplasty-over 100 years of operative history". In: ***Orthopedic reviews*** 3.2.

Kobayashi, A., Bonfield, W., Kadoya, Y., Yamac, T., Freeman, M. A., Scott, G., and Revell, P. A. (1997). "The size and shape of particulate polyethylene wear debris in total joint replacements." In: ***Proceedings of the Institution of Mechanical Engineers. Part H, Journal of engineering in medicine*** 211.1, pp. 11–15.

Koseki, H., Matsumoto, T., Ito, S., Doukawa, H., Enomoto, H., and Shindo, H. (2005). "Analysis of polyethylene particles isolated from periprosthetic tissue of loosened hip arthroplasty and comparison with radiographic appearance". In: ***Journal of Orthopaedic Science*** 10.3, pp. 284–290.

Kraft, M., Koch, D. K., and Bushelow, M. (2012). "An investigation into PEEK-on-PEEK as a bearing surface candidate for cervical total disc replacement". In: ***The Spine Journal*** 12.7, pp. 603–611.

Kuhns, J. G. and Potter, T. A. (1950). "Nylon arthroplasty of the knee joint in chronic arthritis." In: ***Surgery, gynecology & obstetrics*** 91.3, pp. 351–362.

Kumar, M., Mukherjee, P. S., and Misra, N. M. (2013). "Advancement and current status of wear debris analysis for machine condition monitoring: a review". In: ***Industrial Lubrication and Tribology*** 65.1, pp. 3–11.

Kumar, S. and Kruth, J.-P. (2008). "Wear performance of SLS/SLM materials". In: ***Advanced Engineering Materials*** 10.8, pp. 750–753.

Kurtz, S. M. and Devine, J. N. (2007). "PEEK biomaterials in trauma, orthopedic, and spinal implants". In: ***Biomaterials*** 28.32, pp. 4845–4869.

Kurtz, S. M., Ooij, A. van, Ross, R., de Waal Malefijt, J., Peloza, J., Ciccarelli, L., and Villarraga, M. L. (2007). "Polyethylene wear and rim fracture in total disc arthroplasty". In: ***Spine Journal*** 7.1, pp. 12–21.

Lancaster, J. (1968). "Relationships between the wear of polymers and their mechanical properties". In: *Proceedings of the Institution of Mechanical Engineers, Conference Proceedings.* Vol. 183. 16. SAGE Publications, pp. 98–106.

Lancaster, J. (1969). "Abrasive wear of polymers". In: ***Wear*** 14.4, pp. 223–239.
Lapcikova, M., Slouf, M., Dybal, J., Zolotarevova, E., and Entlicher, G. (2008). "Nanometer size wear debris generated from ultrahigh molecular weight polyethylene in vivo". In: ***Wear*** 2.2005, pp. 767–768.
Lowe, D. G. (2004). "Distinctive image features from scale-invariant keypoints". In: ***International Journal of Computer Vision*** 60.2, pp. 91–110.
Lu, S.-B., Hai, Y., Kong, C., Wang, Q.-Y., Su, Q., Zang, L., Kang, N., Meng, X.-l., and Wang, Y. (2015). "An 11-year minimum follow-up of the Charité III lumbar disc replacement for the treatment of symptomatic degenerative disc disease". In: ***European Spine Journal***, pp. 1–9.
Lu, Z. P. and Friedrich, K. (1995). "On sliding friction and wear of PEEK and its composites". In: ***Wear*** 181, pp. 624–631.
Marchand, F. and Ahmed, A. M. (1990). "Investigation of the laminate structure of lumbar disc anulus fibrosus." In: ***Spine*** 15.5, pp. 402–410.
MatWeb, Your Source for Materials Information (2016). URL: `http://www.matweb.com/index.aspx` (visited on 02/15/2016).
Middleton, J., Westcott, V., and Wright, R. (1974). "The number of spherical particles emitted by propagating fatigue cracks in rolling bearings". In: ***Wear*** 30.2, pp. 275–277.
Millett, P. J., Allen, M. J., and Bostrom, M. P. (2002). "Effects of alendronate on particle-induced osteolysis in a rat model". In: ***The Journal of Bone & Joint Surgery*** 84.2, pp. 236–249.
Milošev, I., Kovač, S., Trebše, R., Levašič, V., and Pišot, V. (2012). "Comparison of ten-year survivorship of hip prostheses with use of conventional polyethylene, metal-on-metal, or ceramic-on-ceramic bearings." In: ***The Journal of bone and joint surgery. American volume*** 94.19, pp. 1756–63.
Moghadas, P. M., Mahomed, A., Hukins, D. W. L., and Shepherd, D. E. T. (2013a). "Effect of lubricants on friction in laboratory tests of a total disc replacement device". In: ***Proceedings of the Institution of Mechanical Engineers, Part H: Journal of Engineering in Medicine*** 227.9, pp. 988–993.
— (2013b). "Wear in metal-on-metal total disc arthroplasty." In: ***Proceedings of the Institution of Mechanical Engineers. Part H, Journal of engineering in medicine*** 227.4, pp. 356–61.
Moghadas, P. M., Mahomed, A., Shepherd, D. E. T., and Hukins, D. W. L. (2015). "Wear of the Charité® lumbar intervertebral disc replacement investigated using an electromechanical spine simulator". In: ***Proceedings of the Institution of Mechanical Engineers, Part H: Journal of Engineering in Medicine*** 229.3, pp. 264–268.
Moghadas, P. M., Shepherd, D. E. T., Hukins, D. W. L., and Mahomed, A. (2012). "Polymer-on-Metal or Metal-on-Polymer Total Disc Arthroplasty". In: ***Spine*** 37.21, pp. 1834–1838.
Moghadas, P. M. (2012). "Tribology of ball-and-socket total disc arthroplasty". PhD thesis. University of Birmingham.
Muggeo, V. M. (2003). "Estimating regression models with unknown break-points." In: ***Statistics in Medicine*** 22, pp. 3055–3071.
— (2008). "segmented: an R Package to Fit Regression Models with Broken-Line Relationships." In: ***R News*** 8.1, pp. 20–25.
Muzy, J.-F., Bacry, E., and Arneodo, A. (1994). "The multifractal formalism revisited with wavelets". In: ***International Journal of Bifurcation and Chaos*** 4.02, pp. 245–302.

Myshkin, N. K., Petrokovets, M. I., and Kovalev, a. V. (2005). "Tribology of polymers: Adhesion, friction, wear, and mass-transfer". In: ***Tribology International*** 38.11-12 SPEC. ISS. Pp. 910–921.

Nabhan, A., Ahlhelm, F., Pitzen, T., Steudel, W., Jung, J., Shariat, K., Steimer, O., Bachelier, F., and Pape, D. (2007). "Disc replacement using Pro-Disc C versus fusion: a prospective randomised and controlled radiographic and clinical study". In: ***European Spine Journal*** 16.3, pp. 423–430.

Neukamp, M., Roeder, C., Veruva, S. Y., MacDonald, D. W., Kurtz, S. M., and Steinbeck, M. J. (2014). "In vivo compatibility of Dynesys spinal implants: a case series of five retrieved periprosthetic tissue samples and corresponding implants". In: ***European Spine Journal***.

Nine, M. D., Choudhury, D., Hee, A. Y., Mootanah, R., and Osman, N. (2014). "Wear Debris Characterization and Corresponding Biological Response: Artificial Hip and Knee Joints". In: ***Materials*** 7.2, pp. 980–1016.

Oxford Performance Materials Receives FDA Clearance for 3D Printed OsteoFab® Patient-Specific Facial Device (2015). URL: `http://www.oxfordpm.com/news/article/2014-08-19_oxford_performance_materials_receives_fda_clearance_for_3d_printed_osteofab_patient-specific_facial_device.php` (visited on 08/13/2015).

Park, P., Garton, H. J., Gala, V. C., Hoff, J. T., and McGillicuddy, J. E. (2004). "Adjacent segment disease after lumbar or lumbosacral fusion: review of the literature". In: ***Spine*** 29.17, pp. 1938–1944.

Podsiadlo, P. and Stachowiak, G. W. (2000). "Scale-invariant analysis of wear particle morphology—a preliminary study". In: ***Tribology International*** 33.3-4, pp. 289–295.

Prokopovich, P., Perni, S., Fisher, J., and Hall, R. (2011). "Spatial variation of wear on Charité lumbar discs". In: ***Acta biomaterialia*** 7.11, pp. 3914–3926.

Punt, I. M., Baxter, R., Ooij, A. V., Willems, P., Rhijn, L. V., Kurtz, S., and Steinbeck, M. (2011). "Submicron sized ultra-high molecular weight polyethylene wear particle analysis from revised SB Charité III total disc replacements". In: ***Acta Biomaterialia*** 7.9, pp. 3404–3411.

Punt, I. M., Cleutjens, J. P. M., Bruin, T. de, Willems, P. C., Kurtz, S. M., Rhijn, L. W. van, Schurink, G. W. H., and Ooij, A. van (2009). "Periprosthetic tissue reactions observed at revision of total intervertebral disc arthroplasty". In: ***Biomaterials*** 30.11, pp. 2079–2084.

Purdue, P. E., Koulouvaris, P., Nestor, B. J., and Sculco, T. P. (2006). "The central role of wear debris in periprosthetic osteolysis". In: ***HSS Journal*** 2.2, pp. 102–113.

Putz, R. L. and Müller-Gerbl, M. (1996). "The vertebral column—a phylogenetic failure? A theory explaining the function and vulnerability of the human spine". In: ***Clinical Anatomy*** 9.3, pp. 205–212.

Putzier, M., Funk, J. F., Schneider, S. V., Gross, C., Tohtz, S. W., Khodadadyan-Klostermann, C., Perka, C., and Kandziora, F. (2006). "Charité total disc replacement—clinical and radiographical results after an average follow-up of 17 years". In: ***European Spine Journal*** 15.2, pp. 183–195.

Qiu, M., Chyr, A., Sanders, A. P., and Raeymaekers, B. (2014). "Designing prosthetic knee joints with bio-inspired bearing surfaces". In: ***Tribology international*** 77, pp. 106–110.

R Core Team (2014). *R: A Language and Environment for Statistical Computing*. R Foundation for Statistical Computing. Vienna, Austria.

Raadnui, S. (2005). “Wear particle analysis - Utilization of quantitative computer image analysis: A review”. In: ***Tribology International*** 38.10, pp. 871–878.

Rabinowicz, E. (1961). “Influence of surface energy on friction and wear phenomena”. In: ***Journal of Applied Physics*** 32.8, pp. 1440–1444.

Rabinowicz, E. and Foster, R. (1964). “Effect of surface energy on the wear process”. In: ***Journal of Fluids Engineering*** 86.2, pp. 306–310.

Raghunath, N. and Pandey, P. M. (2007). “Improving accuracy through shrinkage modelling by using Taguchi method in selective laser sintering”. In: ***International journal of machine tools and manufacture*** 47.6, pp. 985–995.

Reda, A., Bowen, R., and Westcott, V. (1975). “Characteristics of particles generated at the interface between sliding steel surfaces”. In: ***Wear*** 34.3, pp. 261–273.

Reynolds, O. (1886). “On the Theory of Lubrication and Its Application to Mr. Beauchamp Tower’s Experiments, Including an Experimental Determination of the Viscosity of Olive Oil.” In: ***Proceedings of the Royal Society of London*** 40.242-245, pp. 191–203.

Richards, L., Brown, C., Stone, M. H., Fisher, J., Ingham, E., and Tipper, J. L. (2008). “Identification of nanometre-sized ultra-high molecular weight polyethylene wear particles in samples retrieved in vivo.” In: ***The Journal of bone and joint surgery. British volume*** 90.8, pp. 1106–1113.

Roy, T., Choudhury, D., Ghosh, S., Mamat, A. B., and Pingguan-Murphy, B. (2015). “Improved friction and wear performance of micro dimpled ceramic-on-ceramic interface for hip joint arthroplasty”. In: ***Ceramics International*** 41.1, pp. 681–690.

Saikko, V., Vuorinen, V., and Revitzer, H. (2015). “Analysis of UHMWPE wear particles produced in the simulation of hip and knee wear mechanisms with the RandomPOD system”. In: ***Biotribology***.

Schmalzried, T., Jasty, M., and Harris, W. H. (1992). “Periprosthetic bone loss in total hip arthroplasty. Polyethylene wear debris and the concept of the effective joint space.” In: ***The Journal of Bone & Joint Surgery*** 74.6, pp. 849–863.

Schmidt, M., Pohle, D., and Rechtenwald, T. (2007). “Selective laser sintering of PEEK”. In: ***CIRP Annals-Manufacturing Technology*** 56.1, pp. 205–208.

Scholes, S. and Unsworth, A. (2000). “Comparison of friction and lubrication of different hip prostheses”. In: ***Proceedings of the Institution of Mechanical Engineers, Part H: Journal of Engineering in Medicine*** 214.1, pp. 49–57.

Schwarz, E. M., Benz, E. B., Lu, A. P., Goater, J. J., Mollano, A. V., Rosier, R. N., Puzas, J. E., and O’Keefe, R. J. (2000). “Quantitative small-animal surrogate to evaluate drug efficacy in preventing wear debris-induced osteolysis”. In: ***Journal of Orthopaedic Research*** 18.6, pp. 849–855.

Scott, D. and Mills, G. (1973). “Spherical debris—Its occurrence, formation and significance in rolling contact fatigue”. In: ***Wear*** 24.2, pp. 235–242.

Sethi, R. K., Neavyn, M. J., Rubash, H. E., and Shanbhag, A. S. (2003). “Macrophage response to cross-linked and conventional UHMWPE”. In: ***Biomaterials*** 24.15, pp. 2561–2573.

Shanbhag, A. S., Jacobs, J. J., Black, J., Galante, J. O., and Glant, T. T. (1994). “Macrophage/particle interactions: effect of size, composition and surface area”. In: ***Journal of biomedical materials research*** 28.1, pp. 81–90.

Sherwood, L. (2011). ***Fundamentals of human physiology***. Cengage Learning.

Shiers, L. (1954). “ARTHROPLASTY OF THE KNEE Preliminary Report of a New Method”. In: ***Journal of Bone & Joint Surgery, British Volume*** 36.4, pp. 553–560.

Smith, L. J. and Fazzalari, N. L. (2009). "The elastic fibre network of the human lumbar anulus fibrosus: architecture, mechanical function and potential role in the progression of intervertebral disc degeneration". In: ***European Spine Journal*** 18.4, pp. 439–448.

Sprecher, C. M., Schneider, E., and Wimmer, M. A. (2004). "Generalized Size and Shape Description of UHMWPE Wear Debris — A Comparison of Cross-Linked, Enhanced Fused, and Standard Polyethylene Particles". In: ***Journal of ASTM International*** 1.1, p. 11202.

Stachowiak, G. W. and Podsiadlo, P. (1999). "Surface characterization of wear particles". In: ***Wear*** 225-229, pp. 1171–1185.

— (2001). "Characterization and classification of wear particles and surfaces". In: ***Wear*** 249.3-4, pp. 194–200.

— (2006). "Towards the development of an automated wear particle classification system". In: ***Tribology International*** 39.12, pp. 1615–1623.

Stachowiak, G. P., Stachowiak, G. W., and Podsiadlo, P. (2008). "Automated classification of wear particles based on their surface texture and shape features". In: ***Tribology International*** 41.1, pp. 34–43.

Stachowiak, G. and Batchelor, A. W. (2013). ***Engineering tribology***. Butterworth-Heinemann.

Stolarski, T. (1992). "Tribology of polyetheretherketone". In: ***Wear*** 158.1, pp. 71–78.

Takacs, J., Toth, L., Franek, F., Pauschitz, A., and Sebestyén, T. (2004). "Friction and wear measurements of laser-sintered and coated parts". In: ***Wear*** 256.11, pp. 1228–1231.

Tan, K., Chua, C., Leong, K., Cheah, C., Gui, W., Tan, W., and Wiria, F. (2004). "Selective laser sintering of biocompatible polymers for applications in tissue engineering." In: ***Bio-medical materials and engineering*** 15.1-2, pp. 113–124.

Ticona, ed. (2001). *GUR Ultrahigh-molecular-weight Polyethylene (PE-UHMW).*

Tipper, J. L., Ingham, E., Hailey, J. L., Besong, A. A., Stone, M. H., Wroblewski, B. M., and Fisher, J. (1997). "Quantitative comparison of polyethylene wear debris, wear rate and head damage in retrieved hip prostheses." In: ***the 43rd Annual Meeting of the Orthopaedic Research Society*** 11.2, p. 355.

Topolovec, M., Cör, A., and Milošev, I. (2014). "Metal-on-metal vs. metal-on-polyethylene total hip arthroplasty tribological evaluation of retrieved components and periprosthetic tissue". In: ***Journal of the Mechanical Behavior of Biomedical Materials*** 34, pp. 243–252.

Topolovec, M., Milošev, I., Cör, A., and Bloebaum, R. D. (2013). "Wear debris from hip prostheses characterized by electron imaging". In: ***Central European Journal of Medicine*** 8.4, pp. 476–484.

Toth, J. M., Wang, M., Estes, B. T., Scifert, J. L., Seim, H. B., and Turner, A. S. (2006). "Polyetheretherketone as a biomaterial for spinal applications". In: ***Biomaterials*** 27.3, pp. 324–334.

Tower, B. (1883). "First report on friction experiments". In: ***Proceedings of the institution of mechanical engineers*** 34.1, pp. 632–659.

Tsouknidas, A. (2011). "Friction induced wear of rapid prototyping generated materials: a review". In: ***Advances in Tribology*** 2011.

Vedaldi, A. and Fulkerson, B. (2010a). *Advanced encodings for recognition.* URL: `http://www.vlfeat.org/applications/apps.html` (visited on 05/03/2015).

— (2010b). "Vlfeat: An Open and Portable Library of Computer Vision Algorithms". In: *Proceedings of the International Conference on Multimedia.* MM '10. Firenze, Italy: ACM, pp. 1469–1472.

Vedaldi, A. and Fulkerson, B. (2010c). *vlfeat - An Open And Portable Library Of Computer Vision Algorithms*. URL: http://vision.ucla.edu/~brian/papers/vedaldi10vlfeat.pdf (visited on 02/24/2012).

Veruva, S. Y., Lanman, T. H., Isaza, J. E., MacDonald, D. W., Kurtz, S. M., and Steinbeck, M. J. (2014). "UHMWPE Wear Debris and Tissue Reactions Are Reduced for Contemporary Designs of Lumbar Total Disc Replacements". In: ***Clinical Orthopaedics and Related Research®*** 473.3, pp. 987–998.

Vicars, R., Fisher, J., and Hall, R. (2009). "The accuracy and precision of a micro computer tomography volumetric measurement technique for the analysis of in-vitro tested total disc replacements". In: ***Proceedings of the Institution of Mechanical Engineers, Part H: Journal of Engineering in Medicine*** 223.3, pp. 383–388.

Visentin, M., Stea, S., Squarzoni, S., Antonietti, B., Reggiani, M., and Toni, A. (2004). "A new method for isolation of polyethylene wear debris from tissue and synovial fluid". In: ***Biomaterials*** 25.24, pp. 5531–5537.

Wang, A., Lin, R., Stark, C., and Dumbleton, J. (1999). "Suitability and limitations of carbon fiber reinforced PEEK composites as bearing surfaces for total joint replacements". In: ***Wear*** 225, pp. 724–727.

Wang, S. B., Ge, S. R., Liu, H. T., and Huang, X. L. (2010). "Wear Behaviour and Wear Debris Characterization of UHMWPE on Alumina Ceramic, Stainless Steel, CoCrMo and Ti6Al4V Hip Prostheses in a Hip Joint Simulator". In: *Journal of Biomimetics, Biomaterials, and Tissue Engineering*. Vol. 7. Trans Tech Publ, pp. 7–25.

Wang, X. (1999). "Calibration of shrinkage and beam offset in SLS process". In: ***Rapid Prototyping Journal*** 5.3, pp. 129–133.

Weightman, B., Simon, S., Paul, I., Rose, R., and Radin, E. (1972). "Lubrication mechanism of hip joint replacement prostheses". In: ***Journal of Tribology*** 94.2, pp. 131–135.

Wen, J. and Khonsari, M. M. (2007). "Transient Temperature Involving Oscillatory Heat Source With Application in Fretting Contact". In: ***Journal of Tribology*** 129.3, p. 517.

Williams, J. (1994). ***Engineering tribology***. Cambridge University Press.

Wilm, J. and Kjer, H. M. (2013). *Iterative Closest Point*. URL: http://uk.mathworks.com/matlabcentral/fileexchange/27804-iterative-closest-point (visited on 02/25/2014).

Wimhurst, J., Brooks, R., and Rushton, N. (2001). "Inflammatory responses of human primary macrophages to particulate bone cements in vitro". In: ***Journal of Bone & Joint Surgery, British Volume*** 83.2, pp. 278–282.

Xin, H., Shepherd, D. E. T., and Dearn, K. D. (2013). "A tribological assessment of a PEEK based self-mating total cervical disc replacement". In: ***Wear*** 303.1-2, pp. 473–479.

Xin, H. (2013). "Evaluation Of Poly-ether-ether-ketone (PEEK) For Cervical Disc Replacement Devices". PhD thesis. University of Birmingham.

Xing, S., Waddell, J., and Boynton, E. (2002). "Changes in macrophage morphology and prolonged cell viability following exposure to polyethylene particulate in vitro". In: ***Microscopy research and technique*** 57.6, pp. 523–529.

Yang, S.-Y., Ren, W., Park, Y., Sieving, A., Hsu, S., Nasser, S., and Wooley, P. H. (2002). "Diverse cellular and apoptotic responses to variant shapes of UHMWPE particles in a murine model of inflammation". In: ***Biomaterials*** 23.17, pp. 3535–3543.

Zetasizer μV User Manual (2008).

Zhang, H., Berg, A., Maire, M., and Malik, J. (2006). "SVM-KNN: Discriminative Nearest Neighbor Classification for Visual Category Recognition". English. In: *2006 IEEE*

Computer Society Conference on Computer Vision and Pattern Recognition - Volume 2 (CVPR'06). Vol. 2. IEEE, pp. 2126–2136.

Zhang, M. Q., Lu, Z. P., and Friedrich, K. (1997). "On the wear debris of polyetheretherketone: fractal dimensions in relation to wear mechanisms". In: ***Tribology International*** 30.2, pp. 87–102.

Zolotarevová, E., Entlicher, G., Pavlova, E., Slouf, M., Pokorny, D., Vesely, F., Gallo, J., and Sosna, a. (2010). "Distribution Of Polyethylene Wear Particles And Bone Fragments In Periprosthetic Tissue Around Total Hip Joint Replacements". In: ***Acta Biomaterialia*** 6.9, pp. 3595–3600.

Zolotarevová, E., Hudeček, J., Spundová, M., and Entlicher, G. (2010). "Binding Of Proteins To Ultra High Molecular Weight Polyethylene Wear Particles As A Possible Mechanism Of Macrophage And Lymphocyte Activation." In: ***Journal of biomedical materials research. Part A*** 95.3, pp. 950–955.